Ultrafast manipulation of magnetization using on-chip THz

Kaushalya Jhuria

THÈSE

Présentée et soutenue publiquement pour l'obtention du titre de

DOCTEUR DE L'UNIVERSITE DE LORRAINE

Mention : PHYSIQUE

par KAUSHALYA

Sous la direction de Prof. Michel HEHN

Ultrafast manipulation of magnetization using on-chip THz

---

26 Octobre, 2021

Membres du jury:

Directeur(s) de thèse :	**Mr. Michel HEHN**	**Professor, IJL, UL, (Nancy)**
	Mr. Jon GORCHON	**CNRS researcher, IJL, (Nancy)**
Président de jury :	**Mr. Hervé Rinnert**	**Professor, IJL, UL, (Nancy)**
Rapporteurs :	**Mrs. Catherine Gourdon**	**Director of research (CNRS), INSP, (Paris)**
	Mr. Gilles Gaudin	**Director of research (CNRS), SPINTEC, (Grenoble)**
Examinateurs :	**Mr. Andrew Kent**	**Professor, New York University, Director of the center for Quantum Phenomena, (New York)**

Institut Jean Lamour

UMR 7198 - Université de Lorraine

Département de Physique de la Matiére et des Matériaux

Kaushalya

October 26th, 2021

Copyright

Dedicated to my family for the unconditional love and support!!!

Acknowledgements

I would like to express my immense gratitude and sincere thanks to my Ph.D. advisors Dr. Jon Gorchon and Prof. Michel Hehn for providing me this great opportunity to work under their guidance. Thanks a lot to Jon, for being so calm, patient, and helpful throughout these 3 years.

I could not have asked for a better advisor. I feel immensely privileged and proud to have worked under your guidance. I will always cherish our regular meetings and discussions. You have collaborated immensely in my quest to learn more about THz spintronics.

Thus, I will always be indebted to him for his advice and words of encouragement he provided to me whenever I felt low or was unnecessarily self-critical. This journey would not have been so fruitful if "The magician of team 101: Michel" was not involved in providing the nicest magnetic samples ever possible. Thanks a lot to Michel for supervising my thesis work from a bit of a distance and providing great pieces of advice and corrections on the manuscript. And a special mention to Prof. Stephane Mangin for being such a nice group leader who never lost an opportunity to keep our diverse group united.

I am especially thankful to the Lorraine University Excellence (LUE) program for financially supporting my research work.

I would like to express my gratitude to venerated jury members, Dr. Catherine Gurdon, Dr. Gilles Gaudin, Prof. Andrew Kent, Prof. Hervé Rinnert for accepting the invitation and providing their invaluable time to examine my work.

I am thankful to all our collaborators from UC riverside (Prof. Richard Wilson, Xinping Shi), UC Berkeley (Prof. Jeffrey Bokor, Dr. Akshay Pattabi, Dr. Roberto Lo Conte), University of Paris (Dr. Aristide Lemaitre) for the fruitful discussions and their involvement in the picosecond SOT switching project. I am also thankful to Dr. Sebastien Petit-Watelot, Dr. Julius Hohlfeld, Dr. Juan Carlos Rojas-Sanchez, and Dr. Gregory Malinowski for their valuable inputs into the work.

A special thanks to Sebastien Petit-Watelot and Laurent Badie as they are such humorous and cheerful people who keep the environment in the institute light-hearted. They never cease to amaze me with their contagious, positive, and vibrant energy.

I am also thankful to our cleanroom staff Dr. Gwladys Lengaigne and Dr. Laurent Badie for their incredible support. They always provided me with instant help and support whenever I required it.

I would like to extend my gratitude to other members of our research team including the administrative staff Amandine Reiter, Martine Tailleur for providing us with a lively atmosphere and making these 3 years an unforgettable experience for me.

I extend my sincere thanks to all the friends in Nancy including Vishnu, Aswin, Sunija, Alaka Di, Aman, Philippe, Thibaud, Huyen, Anna, Alberto, Sandra, Alex, Cataleena, Seb, Thiago, Kathleen, Pierre, Krishnan, Shantanu, Sarah, Quentin, Anil who made my stay in Nancy a memorable experience.

I am also very grateful to my landlady Marie-Odile Selme who also became my close friend. She has been an incredibly gracious host and has made me feel at home. I will especially remember our conversations that varied from our cultural differences and similarities to the importance of families in our lives. These discussions helped me gain a new perspective.

There is a saying, “If your friendship lasts for over 7 years, it’s beyond friendship”. That is indeed true with my besties, Anjana and Priya who are always there for me to lighten up the mood. And if there is any complication going on in my life, they are there to help me out. *Thanks a lot guys for being there for me.*

My Siblings and their kids are those gems in my life who always keep me energized. Thank you so much for always being there to motivate me to pursue my dreams across the globe. Our group video calls were the biggest sources of motivation for me in these last three years. My sisters, Sushila (*Chotya*) and Sunita (*Nanuda*) have always stood by my side whenever I had a low phase whether it was due to professional or personal reasons. They always used to come up with the best solutions to handle the situation. *Chotya and Nanuda, I cannot thank you enough for the way have held my back throughout the Ph.D. journey. I love you!!*

And lastly, If God exists, then it’s definitely in the form of my parents for me who gave me a humble upbringing that was not based on gender bias which is still not the case in many parts of the world. No words will be enough to thank them for what they have provided to me. Whatever little I have done so far or will do in the future, it will always be dedicated to my parents. *Thank you, Maa (Mrs. Mavi Devi), Papaji (Mr. Jagan Singh) for inspiring me through every action in your life. I love you!!*

Abstract

The need for memory storage devices has skyrocketed over the last few decades largely due to the development of the internet. The need for memory storage has reached enormous heights in the past two years, as a consequence of the pandemic due to COVID-19. Such growth in long-term data storage density has been enabled by the field of spintronics and the constant improvements to magnetic hard disk drives (HDDs) the field has provided. Nowadays, spintronics is attempting to reduce the energy consumption of processor-level short-term memories by exploring spin-based alternatives. This thesis deals with one of the major roadblocks for adoption of spintronic solutions in such kind of memories: the speed of magnetization writing.

The speed of operation during the writing of a magnetic bit depends on the magnetization switching mechanism employed. The switching mechanism is itself dependent on the intrinsic magnetic properties of the sample and the externally induced excitation that drives the reversal of the magnetic bit [1]. In this thesis, we will focus on the use of spin-orbit torque (SOT) excitations to drive the reversal, which is a relatively new but fast and energy-efficient approach in comparison with other state-of-the-art methods.

The typical speed of magnetization reversal using SOTs is in the range of few nanoseconds, far slower than the picosecond-long switching that is possible with charge-based memory devices[2]. In fact, a record reversal speed with electrical pulses as short as ~200ps was reported by Garello *et. al*., [3] in 2011 using SOTs. This thesis reports further efforts to speed up the magnetization reversal by almost 2 orders of magnitude by exploiting such SOTs. To this aim, THz electrical pulses were generated via the use Auston photoconductive switches. We demonstrate that a single 6ps wide electrical pulse can induce a SOT to a 1nm thin Co ferromagnetic layer and result in a full magnetization reversal. A systematic study to understand SOTs in the picosecond time regime is also undertaken via using different magnetic nanostructures.

In magnetic memory devices, a “read-head” is used to read the stored information in the device. Typically, in spintronic devices, giant magnetoresistance (GMR) or tunnel magnetoresistance (TMR) based read heads are used for such operations. In this thesis, we also report on the attempts of developing a GMR sensor working in the THz regime.

To undertake the aforementioned studies, a pump-probe optical and optoelectronic experimental setup has also been built and a detailed report of the same is also provided in the thesis.

Keywords: Magnetism, Spin-orbit torques, THz, ultrafast magnetization reversal, giant magnetoresistance

Abstrait

Le besoin de dispositifs de stockage d'information a explosé au cours des dernières décennies, en grande partie en raison du développement de l'Internet. Ce besoin a atteint des sommets énormes au cours des deux dernières années, à cause de la pandémie due au COVID-19. Cette croissance de la densité de stockage d'information pour le long terme a été permise par le champ de l'électronique de spin et des améliorations constants des disque durs magnétiques. De nos jours, l'électronique de spin se focalise sur la réduction de la consommation énergétique des mémoires de court-terme, au niveau du processeur, en explorant des alternatives basés sur la manipulation du spin. Cette thèse traite un des plus grands obstacles pour l'adoption de solutions spintroniques pour ce dernier type de mémoires: la vitesse d'écriture magnétique.

La vitesse d'écriture d'un bit magnétique dépend du mécanisme de retournement de l'aimantation utilisé. Le mécanisme de retournement est lui-même dépendant des propriétés magnétiques intrinsèques de l'échantillon et de l'excitation extérieure induite et qui entraîne le renversement[1]. Dans cette thèse, nous nous concentrerons sur l'utilisation des couples de spin-orbite (SOT) pour entraîner le retournement de l'aimantation, qui est une approche relativement nouvelle, rapide et économe en énergie par rapport à d'autres méthodes de pointe.

La vitesse typique du retournement de l'aimantation à l'aide du SOT est de l'ordre de quelques nanosecondes, bien plus lente que la commutation de l'ordre de la picoseconde qui est possible avec les dispositifs de mémoire conventionnels basés sur la manipulation de la charge[2]. En fait, une vitesse de retournement de l'aimantation record avec des impulsions électriques d'environ ~ 200 ps a été signalée par Garello *et. al.,* [3] en 2011 en utilisant du SOT. Cette thèse rapporte nos efforts pour accélérer le retournement de l'aimantation d'environ deux ordres de grandeur, en exploitant le SOT. Dans ce but, des impulsions électriques THz ont été générées via l'utilisation de commutateurs photoconducteurs (i.e. Auston-switch). Nous démontrons qu'une seule impulsion électrique de 6ps peut induire un SOT sur une couche ferromagnétique de Co d'une épaisseur de 1 nm et entraîner un retournement complet de l'aimantation. Une étude systématique pour comprendre les SOT dans le régime temporel picoseconde est également entreprise via l'utilisation de différentes nanostructures magnétiques.

Dans les dispositifs à mémoire magnétique, une "tête de lecture" est utilisée pour lire l'information stocké dans le dispositif. Typiquement, dans les dispositifs spintroniques, des têtes de lecture à magnétorésistance géante (GMR) ou à magnétorésistance tunnel (TMR) sont utilisées pour de telles opérations. Dans cette thèse, nous rapportons également les tentatives de développement d'un capteur GMR fonctionnant dans le régime THz.

Pour entreprendre les études susmentionnées, un montage expérimental optique et optoelectronique pompe-sonde a également été construit et un rapport détaillé de celui-ci est également fourni dans la thèse.

Mots clés : Magnétisme, Couples spin-orbite, THz, inversion ultrarapide de l'aimantation, magnétorésistance géante

Introduction Générale

Les appareils électroniques sont principalement basés sur la façon dont la charge des électrons est contrôlée à l'intérieur de l'appareil. Les transistors métal-oxyde-semiconducteurs complémentaires (CMOS) omniprésents sont confrontés à de grands défis en raison d'une réduction d'échelle agressive et de l'augmentation de la dissipation d'énergie. Nous avons donc besoin d'une approche complémentaire pour développer de nouveaux dispositifs fonctionnels à faible consommation d'énergie. Une solution proposée consiste à exploiter le degré de liberté due spin des électrons dans les dispositifs. Le domaine de recherche où le degré de liberté de spin est exploité avec le degré de charge d'un électron est connu sous le nom de spintronique.

La spintronique est devenue un domaine majeur après la découverte de la magnétorésistance géante (GMR) en 1988 4. La GMR est un changement de résistance dû à l'interaction entre le transport polarisé en spin dans un matériau magnétique et l'aimantation locale. Ce phénomène peut être utilisé comme un détecteur très sensible de champs magnétiques. L'effet réciproque, consiste du courant agissant sur l'aimantation (au lieu de l'aimantation sur le courant, ou résistance). Cet effet est appelé le couple de transfert de spin (STT) et peut être utilisé pour contrôler l'état magnétique d'un dispositif. Le STT est généralement utilisé dans les vannes de spin, un système multicouche constitué de deux couches métalliques magnétiques séparées par une couche separatrice conductrice. Dans une vanne de spin, les opérations d'écriture et de lecture peuvent être effectuées avec les deux mêmes contacts électriques. Lorsque la couche d'espacement est un isolant, la sensibilité de détection est améliorée par l'effet tunnel de magnéto-résistance (TMR). Deux exemples principaux de dispositifs disponibles dans le commerce qui utilisent ce type de structures sont la mémoire magnétique à accès aléatoire (MRAM) et les têtes de lecture dans les disques durs.

Une méthode relativement nouvelle pour contrôler l'orientation de l'aimantation appelée couple de spin-orbite (SOT) suscite beaucoup d'attention ces derniers temps. L'idée de base derrière cette approche est d'utiliser une couche de métal lourd (HM) pour générer un courant de spin et contrôler l'aimantation d'une couche ferromagnétique (FM) voisine. Les électrons traversant le HM se séparent en fonction de la direction de leur spin en raison du couplage spin-orbite élevé des HM. Cela se traduit par une accumulation d'électrons polarisés en spin sur les bords qui appliquent ensuite un couple au FM, connu sous le nom de SOT. Selon que l'origine de cette séparation de spin se situe dans le volume ou dans l'interface, les SOT peuvent être (dans une image simple) classés en deux catégories : l'effet Spin Hall (SHE) et l'effet Rashba-Edelstein, respectivement. Les composants de couple dominants fournis par ces effets sont respectivement les couples d'amortissement et le

couple de champ, et sont orthogonaux 5. Nous notons que es composantes de couple dépendent également de divers autres paramètres tels que l'épaisseur, la conductance de mélange de spin, le type de FM, le type de HM. , direction d'aimantation en FM, etc. 6. Cependant, l'amplitude et l'origine exactes de ces couples ne sont pas encore totalement comprises, et les sonder à des échelles de temps ultrarapides pourrait éclairer ces questions.

Pour challenger les industries existantes basées sur les charges électroniques et y intégrer la spintronique, l'un des défis est d'accélérer l'opération d'écriture. A titre de comparaison, les temps de commutation record des dispositifs spintroniques dans l'industrie sont encore de l'ordre de la nanoseconde alors que les transistors à effet de champ au silicium ont des délais de commutation inférieurs à 5 ps7. La commutation dans les appareils basés sur STT est limitée à quelques nanosecondes, car des impulsions de courant plus courtes nécessitent de grandes densités de courant et cela peut endommager la jonction magnétorésistive 3. L'alternative récente au mémoires basés sur le STT sont les dispositifs basés sur le SOT où le courant ne traverse pas la magnéto -jonction résistive, ce qui permet de travailler avec des impulsions plus courtes et intenses. Jusqu'à présent, la commutation de magnétisation dans les matériaux à base de SOT a été démontrée avec des impulsions allant jusqu'à 200 ps8. Le principal défi pour accéder et étudier des régimes encore plus rapides, c'est-à-dire inférieurs à 200 ps, est principalement instrumental. Les générateurs d'impulsions avec une telle bande passante et des intensités élevées sont presque inexistants en dessous de 200 ps.

Depuis quelques décennies, des recherches intensives sont en cours pour manipuler l'aimantation de diverses nanostructures magnétiques en utilisant des impulsions laser femtosecondes (fs). Le domaine est né du travail de pionnier effectué par Beaurepaire à el. en 1996, où ils ont montré qu'une impulsion laser de 60fs de large pouvait éteindre l'aimantation d'un ferromagnétique en nickel de 20 nm d'épaisseur en moins de 1 ps [4]. Malgré plus de 20 ans de recherche, de nombreuses questions ouvertes restent sans réponse concernant la physique d'une telle trempe ultrarapide de l'aimantation (perte ultrarapide de moment cinétique), connue sous le nom de démagnétisation ultrarapide. Le mystère majeur tourne autour des mécanismes possibles qui pourraient dissiper le moment angulaire à des échelles de temps aussi rapides. Certains des mécanismes proposés sont basés sur des interactions électron-réseau de retournement de spin 10, d'autres sont basés sur le transport porteur de spin 11.

En 2007, il a été découvert que de telles impulsions laser optiques d'une largeur de femtoseconde pouvaient même inverser l'aimantation, dans des alliages GdFeCo spécifiques, uniquement en raison de l'irradiation optique (sans champs magnétiques appliqués). Une quête de matériaux présentant un tel type de commutation tout optique ultrarapide a depuis été en cours dans de nombreux groupes de recherche. Cependant,

même si de nouveaux matériaux sont trouvés, l'exigence d'un laser femtoseconde rend toute technologie difficile à intégrer avec l'électronique existante.

Alors que la spintronique a été largement étudiée dans une fenêtre de fréquence allant jusqu'à plusieurs GHz ou dans l'infrarouge lointain, le régime THz reste largement inexploré. Le régime THz de la spintronique implique une nouvelle physique et des questions fondamentales qui, si elles sont résolues, pourraient faire progresser considérablement le domaine de la spintronique. Cette thèse est centrée sur la génération THz, la détection THz et sur l'utilisation du THz pour étudier différentes dynamiques de nanostructures magnétiques à des échelles de temps très courtes (picosecondes).

Cette thèse est divisée en 3 grandes sections. La première section (chapitre 2) Contexte et état de l'art, est une brève introduction à la terminologie de base associée au magnétisme, y compris diverses interactions magnétiques, anisotropies magnétiques ainsi qu'une introduction à l'équation LLG qui régit la dynamique d'un moment magnétique. Plus loin dans le chapitre, un bref état de l'art est fourni pour les différentes approches utilisées pour manipuler l'aimantation. Ces différentes approches incluent l'inversion de l'aimantation via des courants de spin (couples de transfert de spin STT et couples de spin-orbite SOT), des impulsions laser femtosecondes (inversion d'aimantation tout optique dépendante et indépendante de l'hélicité) et des impulsions THz.

La deuxième section (chapitre 3) Méthodes, comprend des détails sur le processus de fabrication de nos dispositifs THz sur puce ainsi qu'une introduction aux différentes configurations expérimentales utilisées pour caractériser les échantillons (VSM, TRMOKE, détection THz…). Les différents outils de caractérisation sont répartis en deux catégories : la caractérisation magnétique statique et la caractérisation magnétique dynamique. Parallèlement à la description détaillée des outils expérimentaux, le formalisme mathématique nécessaire pour extraire les quantités d'intérêt est également présenté.

La troisième section (chapitre 4) Résultats et discussion, est une présentation des différents projets entrepris et des résultats obtenus au cours de ce travail de thèse. Ce chapitre est subdivisé en trois chapitres : Premièrement, une étude détaillée de la dynamique de magnétisation entraînée par le couple spin-orbite picoseconde. Deuxièmement, l'inversion de l'aimantation dans les couches minces de Co due aux couples spin-orbite picosecondes. La dernière section se concentre sur l'utilisation des impulsions THz pour détecter les effets magnétorésistifs.

Le chapitre 5 reprend les conclusions et perspectives des différentes études qui ont été entreprises au cours de ce travail de thèse.

CONTENTS

List of Figures

List of Tables

List of abbreviations and symbols

CMOS	Complementary metal-oxide-semiconductor
GHz, THz	GigaHertz, TeraHertz
Ps, fs	Picosecond, femtosecond
STT	Spin-transfer torque
SOT	Spin-orbit torque
TMR	Tunnel magnetoresistance
GMR	Giant magnetoresistance
MRAM	Magnetic random access memory
SHE	Spin-Hall effect
HM	Heavy metal
FM	Ferromagnet
LT-GaAs	Low temperature-Gallium Arsenide
MOKE	Magneto-optic Kerr effect
TRMOKE	Time-resolved Magneto-optic Kerr effect
TDTR	Time domain thermal reflectance
DMI	Dzyaloshinskii-Moriya interaction
PMA	Perpendicular to film plane magnetic anisotropy
LLG	Landau-Lifshitz-Gilbert
M3TM	Microscopic three temperature model
AOS	All-optical switching
SCCM	Standard cubic centimeter per minute
CPS	Co-planar stripline
CPW	Co-planar waveguide
VSM	Vibrating sample magnetometry
PEM	Photo elastic modulator

EOM	Electro-optic modulator
$\boldsymbol{S}$	Spin angular momentum
$\boldsymbol{L}$	Orbital angular momentum
$\boldsymbol{J}$	Total angular momentum
$\boldsymbol{\mu_s}$	Spin magnetic moment
$\boldsymbol{\mu_s}$	Orbital magnetic moment
$\boldsymbol{\mu_J}$	Orbital magnetic moment
$\boldsymbol{\mu_B}$	Bohr magneton
$\boldsymbol{\mu_0}$	Vacuum permeability
g	Landé factor
M	Magetization vector
$\boldsymbol{m}$	Normalized Magetization vector
Ms	Saturation Magetization
H	External magnetic field
E_Z	Zeeman energy
Γ_Z	Zeeman torque
E_D	Dipolar energy
E_{Exc}	Exchange energy
A_{Exc}	Exchange constant
E_{SO}	Spin orbit coupling energy
E_{Ani}	Anisotropy energy
$\boldsymbol{v}$	velocity
E	Electric field
$\boldsymbol{D}$	Antisymmetric exchange vector
K	Anisotropy
V	Volume

Δ_{wall}	Thickness of domain wall
σ_{wall}	Wall energy per unit area
γ	Gyromagnetic ratio of the free electron
$\boldsymbol{H_{eff}}$	Effective magnetic field
α	Gilbert damping constant
$\mathrm{n}_{\uparrow}(E_F), n_{\downarrow}(E_F)$	Density of states of up and down spin electrons at fermi level
P	Spin polarization
β	Spin-transfer constant
I	Electric current
$\boldsymbol{J_C}$	Charge current density
$\boldsymbol{J_S}$	Spin current density
θ_{SH}	Spin-Hall angle
$\hbar$	Planck's constant
$\boldsymbol{\sigma}$	Polarization of accumulated spins
e	Electron charge
$\boldsymbol{\sigma}$	Polarization of accumulated spins
$\boldsymbol{\tau_{FL}}$	Field-like torque
$\boldsymbol{\tau_{DL}}$	Damping-like torque
d_0	Thickness of magnetic layer
T_e	Temperature of electron reservoir
T_s	Temperature of spin reservoir
T_l	Temperature of phonon reservoir
ϵ	Electric permittivity
θ_k	Kerr rotation
ε_K	Kerr ellipticity
Θ	Complex Kerr angle

$\lambda/2$, $\lambda/4$	Half waveplate, quarter waveplate
V_{RF}	RF port output
R_{M}	Responsivity of the photodiodes
g	Internal transimpedence gain of monitors
G	Internal transimpedence gain of RF operational amplifiers
η	Characteristic impedence of the transmission medium
$\langle S \rangle$	Time averaged poynting vector
T_0	Transmission coeficient
V_{IP}	Root mean square of lock-in RF output voltage
V_P	Phase velocity
N	Demagnetizing factor
C	Heat capacity
Λ	Thermal conductivity
ρ_e	Electrical resistivity
T	Temperature
P_{abs}	Absorbed laser power
G_{int}	Internal thermal conductance
T_c	Curie temperature
P_{pump}	Pump power
V	Voltage

1

Introduction

This chapter is a brief description/motivation to the research topic undertaken during this thesis work which includes various spintronic phenomenon at picosecond time scales. Later in this chapter, outline of the thesis chapters is detailed.

*****

Electronic devices are mainly based on how the charge of an electron is controlled inside the device. The ubiquitous complementary metal-oxide-semiconductor (CMOS) transistors are facing great challenges as a result of aggressive downscaling and increases in energy dissipation. We, therefore, need a complementary approach to develop new functional devices with lower power consumption. One proposed solution is to exploit the spin degree of freedom of electrons in devices. The domain of research where the spin degree of freedom is exploited along with the charge degree of an electron is known as Spintronics.

Spintronics became a major field after the discovery of giant magnetoresistance (GMR) in 1988 [5]. GMR is a change of resistance due to the interaction between spin polarized transport in a magnetic material and the local magnetization. This phenomenon can be used as a very sensitive detector of magnetic fields. The reciprocal effect, consists of the current acting on the magnetization (instead of magnetization on the current, or resistance). This effect is called the spin transfer torque (STT) and can be used to control the magnetic state of a device. STT is typically used in spin valves, a multilayer system consisting of two magnetic metallic layers separated by a conducting spacer. In a spin valve both write and read operations can be performed, with the same two electrical contacts. When the spacer layer is an insulator the detection sensitivity is enhanced via the tunnelling magneto resistance (TMR) effect. Two main examples of commercially available devices that use this kind of structures are magnetic random access memory (MRAM) and read heads in hard disk drives.

A relatively new method to control the orientation of the magnetization called spin-orbit torque (SOT) is gaining a lot of attention in recent times. The basic idea behind this approach is to use a heavy metal (HM) layer to generate a spin current and control the magnetization of a neighboring ferromagnetic layer (FM). The electrons flowing through the HM separate based on the direction of their spin due to the high spin-orbit coupling of HMs. This results in the accumulation of spin polarized electrons at the edges which then applies a torque to the FM, known as SOT. Depending on whether the origin of this spin separation is in the bulk or interface, SOTs can be (in a simple picture) classified in two categories: Spin Hall effect (SHE) and Rashba-Edelstein effect, respectively. The dominant torque components provided by these effects are damping like and field like torques, respectively, and are orthogonal [6]. We note that these torque components also depend on various other parameters like thickness, spin mixing conductance, type of the FM, type of HM, direction of magnetization in FM, etc [7]. However, the exact amplitude and origin of these torques is still not fully understood, and probing them at ultrafast timescales could shine some light on these questions.

To challenge the existing electronic charge based industries and integrate spintronics into it, one of the challenge is to speed up the writing operation. For comparison, the record switching time of spintronic devices in industry are still in the order of nanoseconds while silicon-field effect transistors have switching delays of less than 5 ps[8]. Switching in STT based devices is limited to few nanoseconds, since shorter current pulses require large current densities and this can lead to damage of the magneto-resistive junction [3]. A recent alternative to STT are SOT based devices where the current does not cross the magneto-resistive junction, which allows to work with shorter pulses. So far, the magnetization switching in SOT based materials has been demonstrated with pulses down to 200 ps[9]. The principal challenge to access and study even faster regimes i.e. below 200ps, is primarily instrumental. The pulse generators with such bandwidth and high intensities are almost non-existent below 200ps.

Since past few decades, intensive research has been going on to manipulate the magnetization of various magnetic nanostructures by using femtosecond (fs) laser pulses. The field was born from the pioneering work done by *Beaurepaire at el*. in 1996 where they showed that a 60fs wide laser pulse could quench the magnetization of a 20nm thick nickel ferromagnet within less than 1 ps[10]. Despite more than 20 years of research, many open questions remain unanswered regarding the physics of such ultrafast quenching of the magnetization (ultrafast loss of angular momentum), known as ultrafast demagnetization. The major mystery revolves around the possible mechanisms that could dissipate angular momentum at such fast timescales. Some of the proposed mechanisms are based on spin-flipping electron-lattice interactions [11] others are based on spin-carrying transport [12].

In 2007, it was discovered that such femtosecond-wide optical laser pulses could even reverse the magnetization, in specific GdFeCo alloys, purely due to the optical irradiation under no applied magnetic fields [13]. It was later understood that optical heating alone was responsible for the switching. A quest for materials presenting such type of ultrafast all-optical switching has since been underway by many research groups. However, even if new materials are found, the requirement of a femtosecond laser renders any technology difficult to integrate with the existing electronics.

While spintronics has been widely studied in a frequency window up to several GHz or in the far infrared region, the THz regime remains largely unexplored. The THz regime of spintronics involves new physics and fundamental questions that, if answered, could greatly advance the field of spintronics. This thesis is focused on THz generation, THz detection and on the use of THz to study different dynamics of magnetic nanostructures at very short time scales (picoseconds).

This thesis is divided into 3 major sections. The first section (chapter 2) ***Context and state of art***, is a brief introduction to basic terminology associated with magnetism including various magnetic interactions, magnetic anisotropies along with an introduction to the LLG equation which governs the dynamics of a magnetic moment. Later in the chapter, a brief state of the art is provided for different approaches that are used to manipulate the magnetization. These different approaches include magnetization reversal via spin-currents (spin-transfer torque STTs, and spin-orbit torques SOTs), femtosecond laser pulses (helicity dependent and independent all-optical magnetization reversal), and THz pulses.

The second section (chapter 3) ***Methods***, includes details on the fabrication process for our on-chip THz devices along with an introduction to various experimental setups used to characterize the samples (VSM, TRMOKE, THz detection…). The various characterization tools are divided into two categories: static magnetic characterization and dynamic magnetic characterization. Along with the detailed description of the experimental tools, the mathematical formalism necessary to extract the quantities of interest is also presented.

Third section (chapter 4) ***Results and discussion***, is a presentation of different projects undertaken and the results obtained during this thesis work. This chapter is further subdivided into three chapters: First, a detailed study of picosecond spin-orbit torque driven magnetization dynamics. Second, the magnetization reversal in Co thin films due to picosecond spin-orbit torques. The last section focuses on the use of THz pulses to detect magneto-resistive effects.

Chapter 5 includes ***conclusions and perspectives*** for the different studies that have been undertaken during this thesis work.

2

Context and state of the art

This section is comprised of four subsections. Section *2.1* deals with the basic terminology of magnetism including the introduction to various magnetic interactions. Section *2.2* is a brief state of the art on various conventional ways of manipulating the magnetization of thin films. Lastly, section *2.3, 2.4* deals with the ultrafast manipulation of magnetization using femtosecond lasers and picosecond electrical pulses respectively.

*****

2.1 Basics of magnetism

This section is a brief introduction to the main fundamental quantities and energies that characterize magnetic materials. We will also see how the competition between those energies is responsible for the magnetic response of a magnetic nanostructure.

2.1.1 Spin (S), magnetic moment (μ) and Magnetization (M)

The electron is a quantum particle whose state in atoms is entirely defined by four quantum numbers. Among them, the orbital magnetic quantum number corresponds to the projection of the orbital angular momentum onto a given axis and the magnetic spin quantum number corresponds to the projection of the electron's intrinsic angular momentum onto a given axis. For an electron, the magnetic spin quantum number can take two values : $s = \frac{1}{2}$ and $s = -\frac{1}{2}$. As a result, the electron's intrinsic angular momentum also called Spin, can only be in two possible states $\boldsymbol{S} = \pm\frac{\hbar}{2}$. We often describe these two states as spin *up* and spin *down*. The total angular momentum of an electron ($\boldsymbol{J}$) is the sum of Spin ($\boldsymbol{S}$) and the Orbital angular momentum ($\boldsymbol{L}$).

In its orbital motion around the nucleus, the electron, which is a charged particle, creates a magnetic field associated to a magnetic angular moment ($\boldsymbol{\mu_L}$). It is shown that $\boldsymbol{\mu_L} = -\frac{\mu_B}{\hbar}\boldsymbol{L}$. In the same way, a magnetic moment is associated to the spin and is given by $\boldsymbol{\mu_s} = -g\frac{\mu_B}{\hbar}\boldsymbol{S}$ where g is the Landé factor and $\boldsymbol{\mu_B}$ is the Bohr magneton. The total magnetic moment ($\boldsymbol{\mu_J}$) is the sum of $\boldsymbol{\mu_s}$ and $\boldsymbol{\mu_L}$. The total magnetic moment of an atom is then the result of the sum of all the magnetic moments. While the magnetic properties of materials are defined at the atomic scale, the study of the magnetic behavior of nanostructures requires the definition of a magnetization ($\mathbf{M}$) which is the total magnetic moment per unit volume

$$\boldsymbol{M}(\boldsymbol{r}) = \frac{d\boldsymbol{\mu_J}(\boldsymbol{r})}{dV}$$

Where $\boldsymbol{\mu_J}(\boldsymbol{r})$ is the total magnetic moment in a volume dV at position $\boldsymbol{r}$.

We define also the "saturation magnetization" M_S equal to the norm of $\boldsymbol{M}(\boldsymbol{r})$ when magnetic moment is saturated, i.e. all the atomic magnetic moments are oriented in the same direction in the volume dV. This is a property of any magnetic material, regardless of its shape, anisotropy etc.

Finally, we define $\boldsymbol{m}$ the normalized magnetization vector $\frac{\boldsymbol{M}}{M_S}$.

2.1.2 Magnetic Interactions

In the following section, we will represent some of the important magnetic interactions and their corresponding energies. The competition between these energies determines the final magnetic configuration of magnetic materials.

2.1.2.1 Zeeman Interaction and torque

The Zeeman Interaction is defined as the response of a magnetic moment $\boldsymbol{\mu}$ to the presence of an external magnetic field ($\boldsymbol{H}$). The expression of the energy is given by

$$E_Z = -\mu_0 \, \boldsymbol{\mu}.\boldsymbol{H} \qquad 2.1$$

When a magnetic field is applied to a magnetic moment, it tends to align the moment parallel to the applied field. In equation 2.1, the constant μ_0 is the vacuum permeability.

The driving force to align $\boldsymbol{\mu}$ along $\boldsymbol{H}$ is a torque given by

$$\Gamma_Z = \mu_0 \, \boldsymbol{\mu} \times \boldsymbol{H} \qquad 2.2$$

2.1.2.2 Dipolar Interaction

As explained in section 2.1.1, an atom creates a magnetic field associated to its total magnetic moment $\boldsymbol{\mu}$. This atom experiences the field created by all the other atoms of the material. This stray field, $\boldsymbol{H_{di}}$ also called demagnetizing field or dipolar field, induces a dipolar interaction and an energy term given by

$$E_D = -\mu_0 \, \boldsymbol{\mu}.\boldsymbol{H_{di}} \qquad 2.3$$

To get $\boldsymbol{H_{di}}$, the stray fields of all the atoms has to be calculated. It is a long range interaction. This energy term is highly anisotropic. Indeed, using only two magnetic moments, we can easily show that E_D ($\rightarrow\leftarrow$) > E_D ($\uparrow\uparrow$) > E_D ($\rightarrow\rightarrow$). In the case of a thin films, the dipolar energy is minimized when magnetization is in plane. This is referenced in literature as the shape anisotropy (see next sections for details).

2.1.2.3 Exchange Interaction

Inherent to the existence of a magnetic order, the exchange interaction arises from the Coulomb interaction between electrons associated with the Pauli exclusion principle. Practically,

the exchange interaction sets a preferential configuration, parallel or antiparallel, between spins, resulting in magnetic order, a macroscopic magnetization, and the formation of magnetic domains (explained in section 2.1.4). The expression for the exchange energy between 2 neighboring spins, $\mathbf{S_i}$ and $\mathbf{S_j}$, is given by

$$E_{Exc}^{i,j} = -J_{(\vec{r_i}-\vec{r_j})}\, \boldsymbol{S_i} \cdot \boldsymbol{S_j} \qquad 2.4$$

Where J is the exchange integral, and its sign determines the type of magnetic order. Ferromagnetism is favored when J is positive, and antiferromagnetism or ferrimagnetism is favored for negative J value.

To get the total exchange energy, all energies between first neighbours must be summed up and care must be taken not to count energies twice. The expression for exchange energy results in

$$E_{Exc} = \sum_{i,j} E_{Exc}^{i,j} \qquad 2.5$$

When a continuous variation of the magnetization is considered, and not discrete spins, equation 2.5 becomes

$$E_{Exc} = \frac{A_{Exc}}{M_S^2} \int_V \left(\boldsymbol{\nabla} \cdot \boldsymbol{M}(\vec{r})\right)^2 dV \qquad 2.6$$

where A_{Exc} is called the exchange constant.

2.1.2.4 Spin-Orbit Coupling

The electron spin is also coupled to its orbital motion, which lifts the degeneracy between up and down spin states. The origin of this coupling can be understood as follows: When a relativistic particle is moving with velocity $\boldsymbol{v}$ in an electric field $\boldsymbol{E}$, it experiences a magnetic field proportional to $\boldsymbol{v} \times \boldsymbol{E}$ [14]**.** A Zeeman like energy term appears

$$E_{SO} \propto \boldsymbol{\mu}.(\boldsymbol{v} \times \boldsymbol{E}) \qquad 2.7$$

For an electron, the electric potential is created by the nucleus and thus E is radial. As a result,

$$E_{SO} \propto \boldsymbol{\mu}.(\boldsymbol{v} \times \boldsymbol{r}) \qquad 2.8$$

Since $\boldsymbol{L} \propto \boldsymbol{v} \times \boldsymbol{r}$ and $\boldsymbol{\mu} = -\frac{\mu_B}{\hbar}\boldsymbol{L} - g\frac{\mu_B}{\hbar}\boldsymbol{S}$, equation 2.11 becomes

$$E_{SO} \propto \boldsymbol{S}.\boldsymbol{L} \qquad 2.9$$

2.1.2.5 DMI Interaction

The Dzyaloshinskii-Moriya interaction (DMI) is a different type of exchange interaction, which can happen in systems with a broken inversion symmetry and a high spin-orbit coupling. This interaction is anti-symmetric, unlike the exchange interaction, and leads to non collinear arrangement of spins and chiral magnetic textures. In some cases, interesting topological objects such as skyrmions can be stabilized [15]. The energy associated with this interaction between 2 neighboring spins, $\mathbf{S_i}$ and $\mathbf{S_j}$, is given by

$$E_{DMI}^{i,j} = -\boldsymbol{D} \cdot (\boldsymbol{S_i} \times \boldsymbol{S_j}) \qquad 2.10$$

where $\boldsymbol{D}$ is the antisymmetric exchange vector.

2.1.3 Anisotropy Energy

As it is the case for many properties of matter, the magnetic properties are in many cases anisotropic. This anisotropy is reflected in the fact that the magnetization is oriented along certain preferred directions in zero applied field. With this respect, different situations can be encountered. The one that we will encounter in this thesis is the case of the presence of a second-order axis or uniaxial anisotropy for which the general expression is given by

$$E_{Ani} = K\,V\,sin^2\theta \qquad 2.11$$

Where θ is the angle between the magnetization and the anisotropy axis and V is the volume of the magnetic material. For $K > 0$, the energy is minimum when $\boldsymbol{M}$ is along the anisotropy axis, in either direction.

In general, K depends on many parameters of the magnetic material itself (crystalline structure, strain, interface quality, film thickness, saturation magnetization, etc…) [16]. For a given multilayer, temperature will also play a vital role to influence the magnetic anisotropy and generally K decreases as temperature increases. It can greatly help with the energy requirements to switch the magnetization. A more detailed explanation about the temperature dependence on magnetic anisotropy will be provided in the forthcoming chapters.

There are two main fundamental origins to magnetic anisotropy: the dipolar interaction and the spin-orbit interaction.

The dipolar interaction, combined with the geometry of the magnetic sample, leads to what is known as *shape anisotropy.* This has been discussed in section 2.1.2.2. In the case of a thin film, shape anisotropy tends to favor an in-plane magnetization.

The spin-orbit interaction, by coupling the spins and the orbitals, leads to magnetic anisotropy via the anisotropy of the orbitals. For example, due to anisotropy in the crystalline structure, the spin-orbit interaction leads to what is known as *crystalline anisotropy*. The same effect can be achieved by inducing a stress in the material. Similarly, the interfacial orbitals at the surface of magnetic films can lead to a strong magnetic anisotropy, particularly important in very thin films, named *interfacial anisotropy*.

The anisotropy can also be divided in volume and surface contributions. The latter only contribute significantly when the thickness of the magnetic layer is small. We can then write

$$K = K_V + \frac{K_S}{t} \qquad 2.12$$

Where K_V gathers all the anisotropies of volume origin (ex: crystalline and shape anisotropies) and K_S gathers all the anisotropies of surface origin.

In modern storage technologies, perpendicular to film plane magnetic anisotropy (PMA) is chosen. In this case, the anisotropy axis is perpendicular to film plane and K is positive. The binary encoding of the information is obtained with magnetization perpendicular, either positive (bit "1") or negative (bit "0"). The benefit of having a strong uniaxial anisotropy is to provide high thermal stability, or in other words, a long retention time for the data. This long retention time leads to what is also known as non-volatility, and in devices it means that the data will remain stored even in the absence of an external power supply, unlike most charge based processor-level memories.

2.1.4 Magnetic domains and domain walls

As we have just seen, in the presence of a second-order anisotropy axis, the magnetization is in an anisotropy energy minimum when θ =0° and θ =180°. Up to now, we have considered that the magnetization of nanostructures is homogeneous. In some cases, $\boldsymbol{M}(\boldsymbol{r})$ depends on the position. In this case, some areas of magnetization have θ =0° and are in contact with areas of magnetization with θ =180°. The areas with homogeneous magnetization are called domains. The transition between these areas is called a domain wall. The magnetization within this wall varies gradually. If the magnetization rotates parallel to the plane of the wall, the wall is said to be Bloch-type. If the magnetization rotates perpendicular to the plane of the wall, the wall is said to be of the Neel type. Both can be encountered in thin films depending on the energy terms involved. DMI can also play a crucial role in stabilizing the domain walls during the magnetization reversal mechanism, which will be discussed in the later sections.

The spatial extension of a domain wall is finite. In the case of a Bloch wall, a wall that is too wide is extremely expensive in terms of anisotropy energy, while a wall that is too narrow is extremely expensive in terms of exchange energy. Hence, there is always a competition between these two energies, which decides the thickness of the domain wall. A rigorous calculation shows that the wall extension is given by

$$\Delta_{wall} = \pi \sqrt{\frac{A_{Exc}}{K}} \qquad 2.13$$

For this spatial extension, the wall energy per unit area is given by

$$\sigma_{wall} = 4\sqrt{A_{Exc}\, K} \qquad 2.14$$

Domains are formed either during magnetization reversal or as a result of reduction of the dipolar energy. For example, in ferromagnetic materials, the exchange interaction wants to keep all the spins aligned in the same direction and results in a single domain structure but it is not always the case since the dipolar interaction become dominating for long-range interactions and hence fight against the exchange interaction resulting into formation of large domains. Domains can further break into smaller domain due to the dipolar interaction. Figure 2.1 represents the formation of domains in a perpendicularly magnetized cobalt ferromagnet as a result of an external magnetic field.

After going through the basic magnetic interactions and their effects on the magnetic ordering inside the magnetic nanostructure and the static configurations, let's move forward to understand more precisely the dynamics of the magnetization in a magnetic nanostructure. The dynamics will be generated either by a torque induced by applying an external magnetic or spin polarized currents.

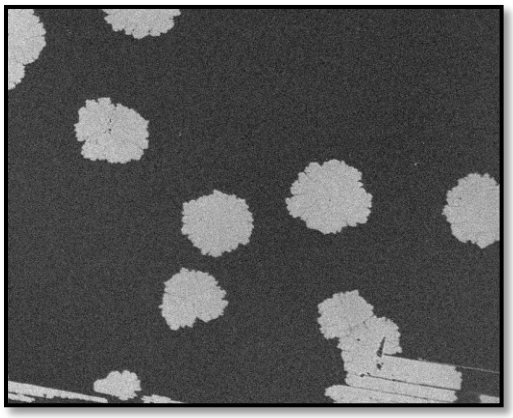

Figure 2.1 MOKE microscopy image of the magnetic domain formation

2.2 Magnetization Dynamics

In this section we will consider a distribution of magnetic moments in a ferromagnetic thin film which is perfectly homogeneous, such that $\boldsymbol{M}$ does not depend on $\boldsymbol{r}$ and so $\boldsymbol{m}$ gives the direction of the magnetization. These assumptions allow to approximate the system by a single moment, and is referred to as the *macrospin approximation*.

In the following sections, we will first review the classical equation which governs the trajectory of a magnetic moment in presence of various forces, and we will later discuss the complete reversal of a magnetic element and the limitations of the macrospin approximation describing it.

2.2.1 Magnetic Field Induced Torques

As detailed in section 2.1.2.1, a magnetic field $\boldsymbol{H}$ exerts a torque on a magnetic moment, $\Gamma_Z = \mu_0 \, M_S \, V \, \mathbf{m} \times \boldsymbol{H}$. Using the kinetic momentum theorem applied to the magnetic moment, the Landau-Lifshitz equation can be derived as

$$\frac{\boldsymbol{dm}}{\boldsymbol{dt}} = -\gamma\mu_0 \, (\boldsymbol{m} \times \boldsymbol{H}) \qquad 2.15$$

where γ is the gyromagnetic ratio of the free electron. As a result, the time evolution of $\boldsymbol{m}$ is driven by the torque exerted by the field $\boldsymbol{H}$ on $\boldsymbol{m}$. Without dissipation, the magnetization will precess around $\boldsymbol{H}$ with a precessional frequency given by the product $\gamma\mu_0 \, \boldsymbol{H}$. In a magnetic material, in addition to the external field, many sources of local fields can be experienced by the magnetization (exchange, dipolar, anisotropy…). As a result, equation 2.15 is rewritten as

$$\frac{\boldsymbol{dm}}{\boldsymbol{dt}} = -\gamma\mu_0 \, (\boldsymbol{m} \times \boldsymbol{H_{eff}}) \qquad 2.16$$

Where $\boldsymbol{H_{eff}}$ is the effective field seen by the magnetization. The above equation only considers the contribution of interactions that are conservative in nature and hence the system will keep precessing indefinitely around $\boldsymbol{H_{eff}}$ as shown in figure 2.2(a). In reality, the system dissipates energy during the precessional motion and hence the oscillations get damped over time as shown in figure 2.2(b). This dissipation of energy can also be considered as an additional torque acting on the magnetization which is always in the transverse direction with respect to $\boldsymbol{H_{eff}}$ and orients $\boldsymbol{m}$ towards $\boldsymbol{H_{eff}}$. The revised form of the above equation is known as the Landau-Lifshitz-Gilbert (LLG) equation, and can be written as below-

$$\frac{\boldsymbol{dm}}{\boldsymbol{dt}} = -\gamma\mu_0\left(\boldsymbol{m}\times\boldsymbol{H_{eff}}\right) + \alpha(\boldsymbol{m}\times\frac{\boldsymbol{dm}}{\boldsymbol{dt}}) \qquad 2.17$$

Here, α is a constant known as the Gilbert damping which governs the intensity of energy dissipation of the precessional motion. The more damping a magnetic nanostructure has, the faster it will dissipate its energy and reach the equilibrium, along $\boldsymbol{H_{eff}}$. The damping of a system is due to various intrinsic and extrinsic contributions such as the electron-magnon scattering, spin-flip scattering etc. For example, it is very hard to achieve ultra-low damping in metallic ferromagnets due to high scattering between the conduction electrons and the magnons present near the fermi level [17]. This scattering becomes negligible in the case of insulating oxides such as Yttrium iron garnets (YIG) and hence it is easy to achieve ultra-low damping in this kind of materials.

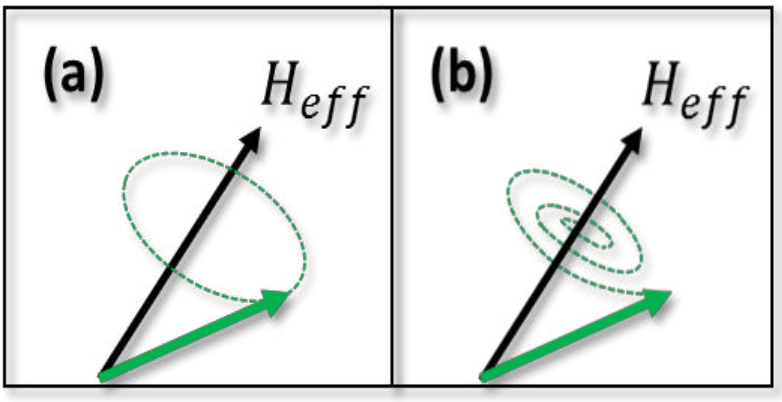

Figure 2.2 Magnetization (green arrow) trajectory in the presence of magnetic field (a) without and (b) with dissipation.

Magnon or spin-waves are generated as a consequence of non-homogenous torques on the system which provide a constant phase difference between the spins.

So far we have seen how the system behaves in the presence of any effective field $\boldsymbol{H_{eff}}$. Controlling the magnetization of the system using an external magnetic field is the most classical way but it has some limitations from the application point of view. Particularly, the requirement of injecting high current amplitudes to generate such high magnetic fields often make the devices energy inefficient[18].

In the next few sections, we will go through various alternative approaches that can be used to efficiently control the magnetization of the magnetic system. The application of an electric spin polarized current pulse to perform this operation is so far the most promising approach. Two of the well-known phenomenon namely the spin-transfer torque (STT) and the spin-orbit torque (SOT) are described in the following sections.

2.2.2 Spin polarized current, Giant Magnetoresistance and Spin Transfer Torques

In the ferromagnetic transition metals such as Iron (Fe), Cobalt (Co), and Nickel (Ni), the current can be divided into two channels [19], one for the spin up electrons and the other for spin-down electrons. In these metals, the current is mainly carried by the 3s polarized electrons since the effective mass is larger for d electrons. 3d electrons are responsible mainly for the magnetization. According to Stoner's theory of magnetism, the 3d band splitting for these metals is such that the density of the states for up $n_{\uparrow}(E_F)$ and down $n_{\downarrow}(E_F)$ spin electrons is not equal at the fermi level E_F. This inequality leads to a spin polarization (P) that is given by the equation 2.18

$$P = \frac{n_{\uparrow}(E_F) - n_{\downarrow}(E_F)}{n_{\uparrow}(E_F) + n_{\downarrow}(E_F)} \qquad 2.18$$

If P =0 as in normal metals (Cu, Pt, Au…), the current is not polarized. If P =1, the current is fully polarized and the ferromagnet is called a half-metal [20].

A first effect of the existence of this spin polarization is the anisotropic magnetoresistance effect. Due to spin–orbit coupling, the orientation of the electron orbitals in a ferromagnetic material is determined by the direction of the magnetic field. This results in a greater scattering cross-section for a transport electron when the direction of the current is parallel to the applied field. As a result, changing the magnetization direction with respect to the current will change the resistance of a single ferromagnetic layer [21].

Due to improvements in thin-film growth techniques, spin polarized currents were eventually injected into another magnetic material though a non-magnetic material, a metal or an insulator. This was only possible when control over layer thicknesses of less than several nanometers was developed. Thin films have been key for various spintronic phenomena such as giant magnetoresistance, tunnel magnetoresistance effects or the Spin-Transfer Torque (STT).

The discovery of giant magnetoresistance effect has a great importance in the technological development of spintronic devices. In multilayers, composed by an alternation of nanometer thick magnetic and non-magnetic layers, the modification of the magnetic state by an external magnetic field induces a very high (can reach 100%) change in the resistance. This simple architecture replaced the conventional inductive read heads in the hard disk drives (HDDs) and it is also responsible for the enormous increment in the reading sensitivity. Figure 2.3 represents the graphical view of the technological advancement in hard disk drives to enhance the areal

density as a result of development in the magnetoresistance and thin-film growth techniques. Giant magnetoresistance can be studied in various kinds of magnetic nanostructures namely the magnetic multilayer GMR, spin valve GMR, Pseudo-spin-valve GMR, Granular GMR, etc [22].

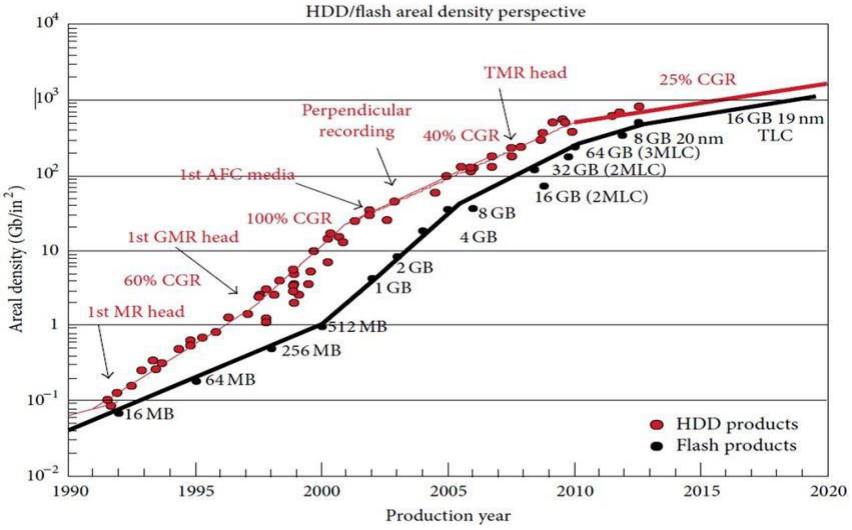

Figure 2.3 Graphical representation of the areal density in a HDD over the last 3 decades [23]

The simplest magnetic nanostructure is called spin valve and is made of two magnetic layers spaced by a nonmagnetic (NM) layer. In the spin-valve system, as shown in figure 2.4(a), one of the magnetic layers has a magnetization that is pinned in one particular direction and is known as the fixed layer. The magnetic state of this layer will not change under applied field. The other magnetic layer is called the free layer and can reverse. The schematic shown in figure 2.4(a) is the in-plane (IP) anisotropy based geometry of the spin-valve structure.

Both the spin valve and the magnetic multilayer structure based systems were used in this thesis work to study giant magnetoresistance effect in the THz regime.

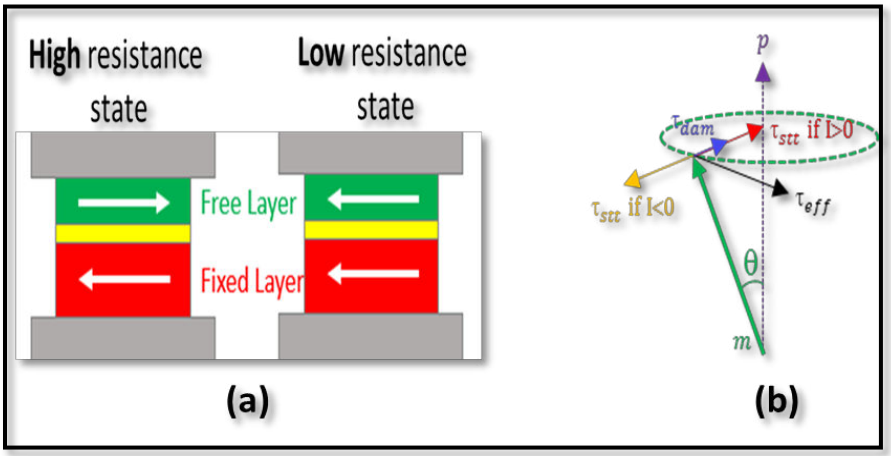

Figure 2.4 (a) Schematic view of the spin-transfer torque and (b) various torques ruling the magnetization dynamics of the free layer in a spin valve system

Depending on the geometry of the magnetic system used and the magnetoresistance origin, it can be classified into three major categories: anisotropic magnetoresistance (AMR), giant magnetoresistance (GMR), and tunnel magnetoresistance (TMR). The schematic represents of all the MR effects are shown in figure 2.5. For the GMR and TMR schematics, FM1 and FM2 represents the pinned and the free layer respectively. NM represents the nonmagnetic metallic spacer layer in the case of GMR whereas the spacer is replaced by an insulating layer in the case of TMR.

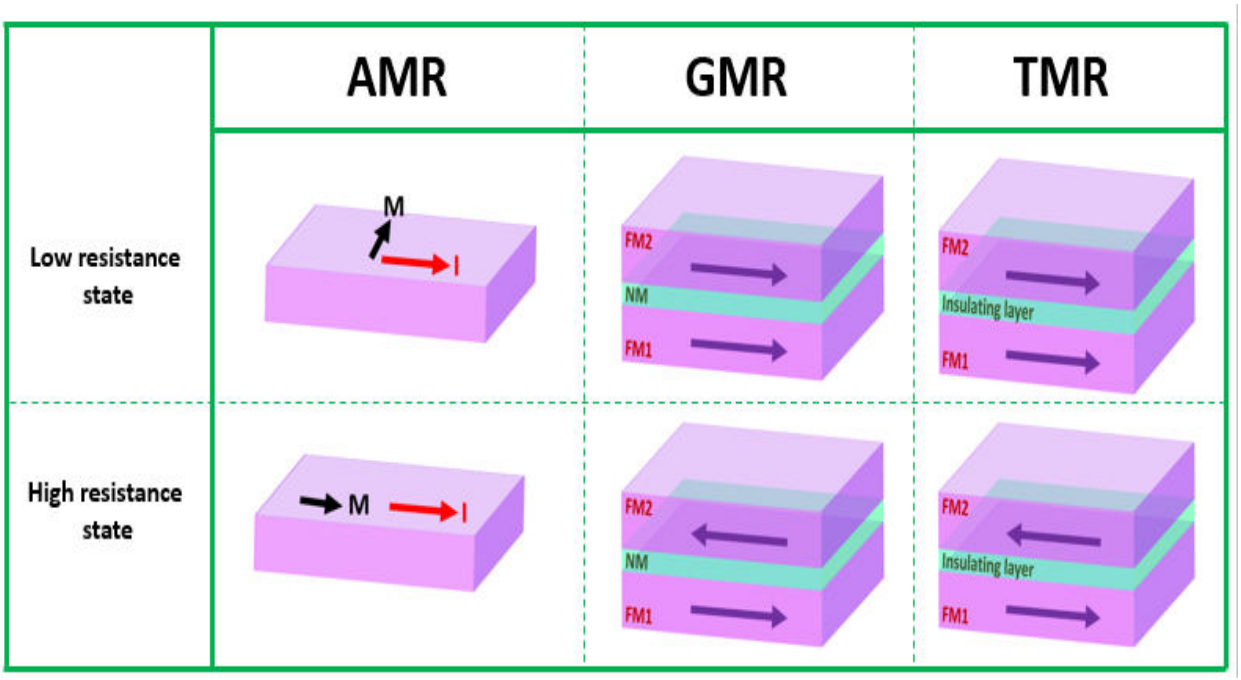

Figure 2.5 Schematic representation of anisotropic magnetoresistance (AMR), giant magnetoresistance (GMR), tunnel magnetoresistance (TMR).

Reducing the size of the GMR hard drive head, i.e. increasing the current density, lead to the experimental discovery of Spin Transfer Torque (STT). STT was first predicted theoretically by Slonczewski and Berger in 1996 [2425]. For spin transfer torques, the spin polarized current carried by conduction electrons and polarized by the fixed layer reaches the free layer and provides a torque on the local magnetization. The spin transfer torque term was incorporated into the Landau-Lifshitz-Gilbert equation by Slonczewski [24] as shown in equation 2.19.

$$\frac{\boldsymbol{dm}}{\boldsymbol{dt}} = -\gamma\mu_0\left(\boldsymbol{m}\times\boldsymbol{H_{eff}}\right) + \alpha\left(\boldsymbol{m}\times\frac{\boldsymbol{dm}}{\boldsymbol{dt}}\right) - \beta IG(\theta)\,\boldsymbol{m}\times(\boldsymbol{m}\times\boldsymbol{p}) \qquad 2.19$$

Here, β is a spin-transfer constant, I is the electrical current, $G(\theta)$ is the angular dependent function of the spin-transfer torque, $\boldsymbol{m}$, and $\boldsymbol{p}$ represents the unitary vectors in the direction of the free and the fixed layer magnetization respectively. The spin-transfer torque in such a configuration as shown in figure 2.4(b), induces an anti-damping or damping-like term (depending on the polarity of the injected current), that can be used to switch or stabilize the magnetization. However, in *some structures and geometries*, the spin-transfer torque can also lead to a field-like torque that induces a precession of the moment around the injected spin density [26].

This simple concept of controlling the magnetic state of the free layer by injecting an electric current into the spin-valve system has been widely used in spintronic-based data storage devices such as magnetic random access memory (MRAM) for write operations. However, spin-transfer torque magnetic random access memory (STT-MRAM) still have some practical limitations. Particularly, these devices require long electrical current pulses (few nanoseconds) which slow down their operational speed. Long electrical current pulses are required because in spin valves with a pair of *parallel* ferromagnetic layers, an incubation delay is present for the spin torques. The reason is that, as shown in Equation 2.19, no torque can be induced when the layers are fully parallel. In practice though, at room temperature, thermal excitations induce small misalignments between the layer's magnetization, which can then experience spin-torques. The spin-torques then induce even larger misalignments, which act as a feedback loop to allow even larger spin-torques, eventually leading to switching. In order to speed up the dynamics, larger spin-torques can be applied, via an increased current injection, but a waiting time related to the stochastic thermal excitations will still be present. Moreover, in most STT-MRAM designs, the insulating interlayer necessary for reading limits the injected current density since the high current flow can lead to damage [27]. In order to speed up the operation of magnetic random access memory, a more recent alternative type of spin-torque, namely the spin-orbit torque (SOT) can be employed.

2.2.3 Spin-Orbit Torques

Instead of using a ferromagnetic layer to obtain a spin current, an alternative method is to exploit the Spin-Hall effect (SHE). When a charge current is injected into a high spin-orbit material, such as a heavy metal, the up and down spin electrons get separated into opposite directions. This separation of up and down spin electrons provides a spin-current (I_S) in the transverse direction to the applied charge current (I_C). Typically, a bilayer structure of heavy metal/ferromagnet is used to inject the spin current from the heavy metal into the adjacent

ferromagnet and torque it via the spin transfer torque as shown in figure 2.6 (a). Such type of torque is called a spin-orbit torque (SOT) [2] [28]. This torque can very efficiently control the magnetic state of the ferromagnet [29] [30] [31] [32] [33]. The generated spin current density ($\boldsymbol{J_S}$) is written in equation 2.20 [34]. Here, $\boldsymbol{J_C}$ is the charge current density, ħ is Planck's constant, e is electron charge, θ_{SH} is the spin Hall angle of the heavy metal, which determines the direction of spin accumulation at the HM/FM interface. The polarization ($\boldsymbol{\sigma}$) of accumulated spins is always orthogonal to both $\boldsymbol{J_C}$ and $\boldsymbol{J_S}$.

$$\boldsymbol{J_S} = \frac{\hbar}{2e}\theta_{SH}(\boldsymbol{J_C} \times \boldsymbol{\sigma}) \qquad 2.20$$

Similar to the spin Hall effect, a high spin-orbit coupling can also lead to a transverse spin polarization at certain interfaces. This is known as the Rashba-Edelstein effect. The phenomenon is typically observed in a ferromagnetic layer sandwiched between a heavy metal in the bottom and an oxide layer on the top[29]. The presence of the bottom heavy metal and the top oxide layer creates an asymmetric electric field potential in the vertical direction (direction of symmetry breaking), namely the Rashba field. The schematic representation of interfacially induced spin orbit torque on the magnetic system is shown in figure 2.6 (b). A simple picture is to consider that this electric field potential translates into a magnetic field from the electron's frame of reference. This translated magnetic field then applies a torque onto the ferromagnet that can be used to manipulate the magnetization of the ferromagnet. A more realistic picture is that the Rashba field and spin-orbit coupling induce a spin momentum locking, which means that electrons going forward have a different spin from those going backwards.

When applying a current, and increasing the population of electrons going forward, we generate a net spin polarization that can then torque the neighboring magnet. A whole new class of materials is also under study to exploit SOTs such as in topological insulators where the bulk part of the material shows insulating properties while the surface is conductive [35].

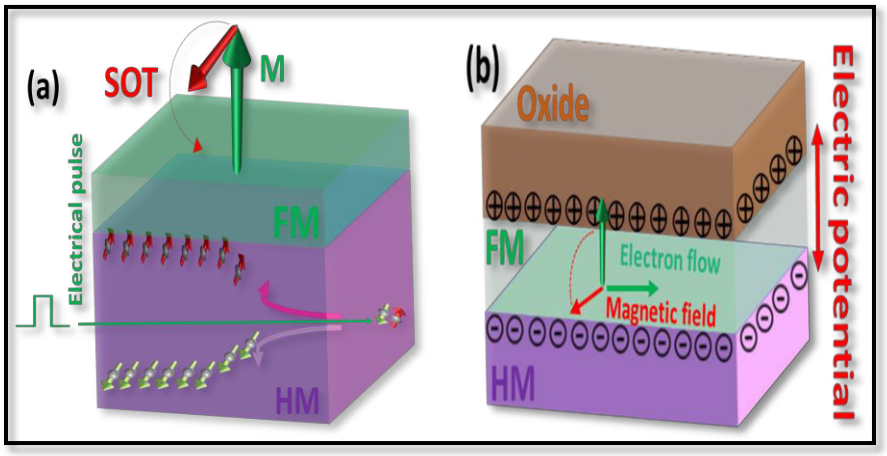

Figure 2.6 Schematic representation of (a) spin Hall effect based and (b) interface driven Rashba Edelstein effect based spin-orbit torques

Just like with spin-transfer torques, spin-orbit torques can also provide both the damping ($\boldsymbol{\tau_{DL}} \sim \boldsymbol{m} \times (\boldsymbol{\sigma} \times \boldsymbol{m})$) and the field-like ($\boldsymbol{\tau_{FL}} \sim \boldsymbol{\sigma} \times \boldsymbol{m}$) torques to the magnetic layer as shown in figure 2.7. [36]. In figure 2.7, $\boldsymbol{B_{DL}}$ and $\boldsymbol{B_{FL}}$ are the effective magnetic fields corresponding to $\boldsymbol{\tau_{DL}}$ and $\boldsymbol{\tau_{FL}}$ respectively. Even after years of intensive research, it is still a point of debate in the spintronic community to quantify clearly the origin of spin orbit torques in bulks and interfaces.

Even though in practical situations, the applied torque on the ferromagnet is always a contribution from both the damping and the field-like torques, the nature and magnitude of dominating torque depend on both intrinsic and extrinsic parameters. Some of these parameters are the thickness of the layers, spin mixing conductance, type of the heavy metal (HM), type of the ferromagnet (FM), the direction of magnetization in FM, etc [7]. For example, different transition metals of 4d and 5d groups such as platinum (Pt) and tantalum (Ta) have opposite polarities of spin-Hall angle (SHA) depending on the number of d electrons present in the outermost orbit. Opposite polarity of SHA means that for the same direction of charge current flow in the heavy metals spins separate in the opposite direction and hence the spin orbit torque [37].

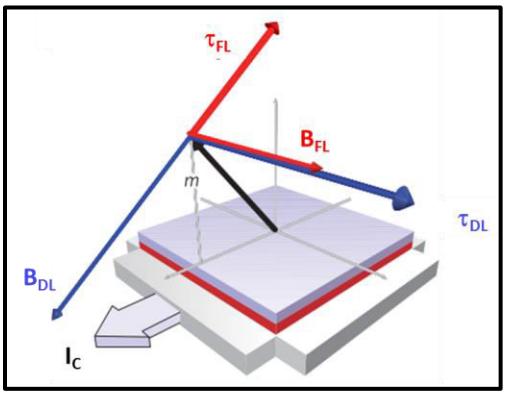

Figure 2.7 Schematic representation of different SOT components and their respective effective fields. Adapted from K.Garello et. al.,2013 [36].

The Landau-Lifshitz-Gilbert equation governing the magnetization dynamics under the influence of SOT can be written by simply including the damping and field like terms of SOT in equation 2.17.

$$\frac{\boldsymbol{dm}}{\boldsymbol{dt}} = -\gamma\mu_0\left(\boldsymbol{m}\times\boldsymbol{H_{eff}}\right) + \alpha(\boldsymbol{m}\times\frac{\boldsymbol{dm}}{\boldsymbol{dt}}) - \theta_{SH}^{DL}C_s\left(\boldsymbol{m}\times(\boldsymbol{m}\times\boldsymbol{\sigma})\right) + \theta_{SH}^{FL}C_s(\boldsymbol{m}\times\boldsymbol{\sigma}) \qquad 2.21$$

Where $C_S = \frac{\mu_B}{\mathrm{e}}\frac{\boldsymbol{J_c}}{d_0}\frac{1}{M_S}$ is material dependent constant with μ_B being the Bohr magneton, d_0 is the thickness of the magnetic layer. $\theta_{\mathrm{SH}}^{DL}$ and $\theta_{\mathrm{SH}}^{FL}$ are the damping and field like spin Hall angles respectively.

For the complete literature review on spin orbit torques, we refer the readers to the review articles written by R. Ramaswamy *et. al.*, 2018 [28], J. Sinova *et. al.*, 2015 [2], and A. Hoffmann *et. al.*, 2013 [38]. In this section, we will only go through some of the references, which are essential to understand the results obtained during this thesis work.

Spin orbit torques can be exploited in both the In-plane and Out-of-plane magnetic anisotropy based systems but the current magnetic random access memory implementation prefers the Out-of-plane anisotropy systems due to better scalability. In the Out-of-plane anisotropy based systems or perpendicular magnetic anisotropy systems, since the spin accumulation is always in-plane, there is a requirement for a small external field $\boldsymbol{H_{ext}}$ to break the symmetry of the system and define the final magnetic state based on the direction of in-plane spin accumulation or spin orbit torque. This external field is also essential during the magnetic domain-wall propagation based switching to fight against the DMI effect which stabilizes the chiral Néel domain walls and can hinder the switching process [39]. The requirement of $\boldsymbol{H_{ext}}$ is one of the major hurdles for broad adoption of spin orbit torques for application purposes. External field-free switching using spin orbit torques in perpendicular magnetic anisotropy systems is also one of the active topics of research where various approaches are being used such as wedged structural engineering, exchange coupling based techniques, and geometrical domain-wall pinning [28].

There are different ways to evaluate the magnitude of SOTs such as the magneto-optic Kerr effect (MOKE) [40], harmonic Hall voltage measurements [6], spin-torque ferromagnetic resonance (ST-FMR) [41]. During this thesis work, Hall voltage measurements have been done to extract the critical current density requirement for quasi-static magnetization reversal using wide electrical pulses. Mainly the MOKE microscopy and time-resolved magneto-optic Kerr effect (TRMOKE)

measurements are being undertaken to study the spin orbit torque dynamics and reversal in ultrafast time scales. Details about the experimental setup are provided in chapter 3.

So far in this section, we have mentioned the fundamentals of spin orbit torques, their origins, various material systems to exploit these torques, the spin orbit torque symmetries, and requirement of $\boldsymbol{H_{ext}}$ in the perpendicular magnetic anisotropy based systems. In section 2.2.4, we will go through various switching schemes, which govern the full reversal of the magnetic state of the systems.

2.2.4 SOT Switching Schemes

There are various mechanisms involved in a spin-orbit torque driven reversal, which can be classified into two main categories i.e. coherent and incoherent switching. Coherent switching corresponds to the reversal of the magnetization during which all of the spins follow the same exact dynamics [31]. However, almost all observations to date, based on spin-orbit torques as well as other types of torques, point towards an incoherent switching scenario.

Since the spin-orbit torques were discovered, it was soon found out that switching measurements were not in good agreement with the macrospin model. The switching current densities were found to be substantially low in comparison with the predictions made by the macrospin model [42,31,3.] The reason is that the whole system is not reversed at the same time. Initially, a specific region gets reversed (domain nucleation) and then the whole system gets reversed through domain expansion. Such domain nucleation can take place in various ways: it can be initiated by multiple random nucleation sites or from a single nucleation site (ex: at the edge) [43].

The pulse duration of the incident charge current pulse (τ_p) plays a vital role in the critical current (I_c) requirement, switching speed as well as the switching mechanism. *K. Garello et. al. in 2014,* [3] measured the critical current for spin-orbit torque switching as a function of charge pulse duration in a Pt (3)/Co (0.6)/AlOx nanodot of 96nm lateral size. In their experiments, they found that for $\tau_p <$ 1ns, I_c increases sharply as the pulse duration is reduced, whereas for $\tau_p >$1ns, the dependence is quite weak, as shown in figure 2.8. Here, τ_0 represents the transition from one regime to the other. They concluded that for $\tau_p <$ 1ns, the switching was deterministically driven by a single domain nucleation at the edge and domain wall's propagation. The critical current was attributed to the amount of angular momentum to be transferred during the duration of the pulse that was needed to move the domain wall from one

edge to the other. For pulse durations above τ_0, stochastic nucleation would help the reversal, reducing the critical current.

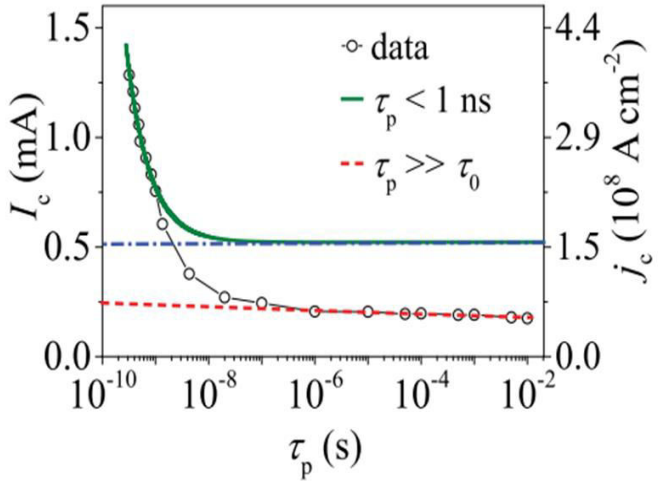

Figure 2.8 Critical current I_c (left y-axis) and current density J_c (right y-axis) as a function of pulse duration (τ_p) [3].

This incoherent switching scheme is also strongly dependent on the dimensions of the devices. Coherent switching is possible only in ultrathin films with nanoscale dimensions (< 20-100 nm). For example, during a work done by Zhang *et al.* [1], it was found that for a fixed current pulse duration, the critical current density increases very little when the device diameter was reduced from 80 to 30nm whereas a sharp increment (an order of magnitude) was observed while going from micrometer wire to 80nm magnetic dot. This observation was interpreted as the transition from an incoherent to a coherent switching regime.

The center point of all the studies done so far is to understand the role of different torque components, their contribution in the switching process and also, to understand the contribution of other parameters that can affect the switching scheme. A good understanding of the switching scheme involved is important to further modify the systems to reach the goal of energy-efficient and fast switching.

As we have seen in this section the pulse duration of the charge current plays an important role in the switching scheme and hence the switching time. For example, in the case of domain wall nucleation, the speed of domain wall propagation is a limiting parameter to decide the overall switching time.

During this thesis work, a Co ferromagnet was sandwiched between two heavy metal layers namely the bottom Pt and top Ta. These two heavy metal layers are used since the Spin-Hall angle of both layers is opposite to each other and by being grown on each side of the Cobalt layer the total spin orbit torque can be enhanced [33].

So far, we have seen how to manipulate the magnetization of a magnetic system by using an external magnetic field or electric current pulses. Since the slow switching time is still a huge hurdle to replace the spintronic devices with their CMOS counterparts, people have also tried to exploit other ways of manipulating the magnetization of a magnetic material. In section 2.3, we will go through some of the important studies which have been done to control the magnetization in ultrafast time scales using femtosecond (f_s) laser pulses.

2.3 Ultrafast Dynamics

In the 1990's a new approach to manipulate the magnetization at ultrafast timescales came into the picture as intense femtosecond laser sources were becoming more and more widely available [44].

2.3.1 Femtosecond laser-induced ultrafast demagnetization

The very first experimental demonstration of femtosecond laser-induced magnetic manipulation was reported by Beaurepaire *et. al*. in 1996 [4] where a Nickel (Ni) ferromagnetic thin film of 22nm was irradiated by a 60 fs wide laser pulse. During the longitudinal time-resolved magneto-optical Kerr effect measurements, it was found that the magnetization of Ni thin film gets quenched rapidly within 1 ps of the laser pulse arrival as shown in figure 2.9 (a). This result received a lot of attention from the spintronic community as it posed some fascinating questions such as: how the laser light is triggering these ultrafast magnetization dynamics? Where is the angular momentum of the system going? How rapidly is the angular momentum getting exchanged between different reservoirs such as the electron, lattice, or spin baths?

In their seminal work, Beaurepaire and colleagues proposed a simple three-temperature model (3TM) to describe the observed dynamics. According to this model, which is an extension of the famous 2 temperature model, electrons (T_e), phonons (lattice; T_l) and spins (magnons; T_s) are thermal reservoirs that can store the incident laser energy. As a result of light-matter interaction on the laser pulse arrival, since the optical-near IR is only able to excite the electronic system, the electron temperature increases rapidly. Subsequently, electrons start to exchange the thermal energy with the spin and phonon baths. The graphical representation of the temperature profiles of these three reservoirs is plotted in figure 2.9 (b). The description provided by Beaurepaire *et. al*. in 1996 was incomplete in a sense because they did not consider the flow of angular momentum between different reservoirs which they later took into account

and showed experimentally, that a THz electromagnetic field is emitted as a consequence of ultrafast demagnetization to conserve angular momentum [45].

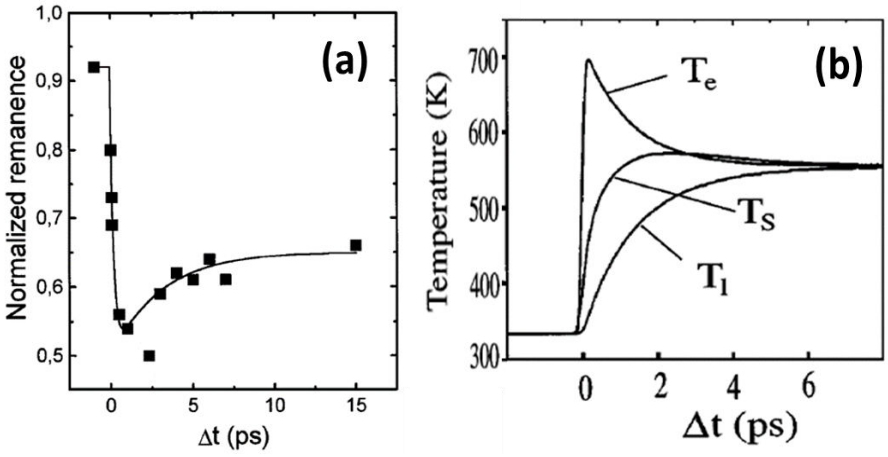

Figure 2.9 (a) TRMOKE data representing the ultrafast demagnetization in Ni thin film, (b) Graphical representation of electron temperature (T_e), lattice temperature (T_l), and spin temperature (T_s), calculated using 3TM[4].

Even after years of intensive research, it is still an unsolved puzzle to understand the underlying mechanism involved in ultrafast demagnetization. We refer the interested readers to read the review articles written by Kriliyuk *et. al*., in 2010 [46] and Malinowski *et. al*. in 2018,[47] to get a detailed description of the advances that have been made in the past two decades to understand the underlying mechanism. In this thesis, we will only mention some of the most exciting experimental results and commonly used models that have been proposed to have a better understanding of the underlying physics of this phenomenon.

Two temperature (2T) and three temperature (3T) models are the most widely used frameworks to describe ultrafast demagnetization. In the year 2009, Koopmans *et. al.* developed a microscopic three temperature (M3TM) [48]. This model is based on Elliott-Yafet scattering, according to which, the spin state of an electron flips as a result of electron-phonon interaction, and the difference of angular momentum due to spin-flip get transferred to the lattice.

On the experimental ground, it is well known that the femtosecond laser pulse can generate a large number of excited electrons called hot electrons. These hot electrons lead to ultrafast demagnetization by diffusion of spins in the superdiffusive regime [49]. A theoretical model has also been proposed to explain the demagnetization process via these hot-electron spins by Battiato et. al.,[12] in the year 2010 soon after the experimental demonstration done by Malinowski et. al [50]. In recent years, people have even started using these hot electrons to manipulate a remote magnetic system in spin-valve like structures [47]. In the next section, we will

briefly go through the magnetization reversal studies that have been done by directly exciting the material with femtosecond laser light.

2.3.2 Femtosecond laser-induced ultrafast switching

After the discovery of ultrafast demagnetization, people started looking into different materials to achieve a full reversal of the magnetization as a consequence of direct excitation with femtosecond laser light. In the year 2006 Stanciu *et. al.*, [51] demonstrated the magnetization switching in GdFeCo ferrimagnetic alloys using femtosecond laser light illumination. GdFeCo ferrimagnets consist of two different spin sub-lattices that are anti-ferromagnetically coupled to each other with uncompensated magnetic moments. These two distinct elements (Gd and Fe or Co) have different demagnetization dynamics in single element bulk systems. In the alloy as well, the sublattices experience different demagnetization rates [52] despite the strong exchange interaction. During demagnetization angular momentum is exchanged between the sublattices and when the FeCo reaches a full demagnetization, the angular momentum from the Gd sublattice leads to the reversal of the FeCo magnetization. The full magnetization reversal is achieved when the Gd sublattice is also reversed as a result of the antiferromagnetic exchange with the FeCo. Initially, the all-optical magnetization switching in GdFeCo was believed to be dependent on the helicity of the light polarization [51], and was termed Helicity Dependent AOS. However, it was soon found out that the reversal mechanism could also be triggered independently of the polarization [52], the polarization thus playing a minor role, and was thus renamed Helicity Independent AOS. New material systems fitting either of these types of reversal types (HD vs HI AOS) have since been found [5354], and the underlying mechanisms are believed to be drastically different.

Indeed, the all-optical switching is a big achievement for the spintronic community since the switching speed gets increased by at least 100 times in comparison with the achievable switching speed using conventional magnetic fields or spin torques. The underlying mechanism of femtosecond laser-induced ultrafast demagnetization, as well as the reversal, is still a topic of debate within the community. Current all optical switching still has some limitations though: First of all, the range of material where ultrafast all-optical switching has been demonstrated is still limited to Gd-based and Tb-based ferrimagnetic systems [55] with the recent exception of MnRuGa Heuslers [56]. Moreover, integration of all-optical methods into solid-state electronics remains challenging due to the requirement of the bulky laser systems and the requirements to combine optics with electronics. Recently, in 2017, a new approach has been proposed by Wilson *et. al.,* [57] where picosecond wide *electrical* pulses were used to perform ultrafast

manipulation of magnetic systems. In the next section, we will go through the advances that have been made in this very exciting and new area of spintronics.

2.4 Ultrafast (THz) Spintronics

Figure 2.10 represents the electromagnetic spectrum and its classification of various regimes. Fundamentally, all electromagnetic waves are governed by the same physics and respond to Maxwell's equations. In practice though, different mathematical tools or models are used to describe the systems for each regime. When low-frequency waves are used, and the wavelength is large compared to the dimensions of the circuit (cables), then the voltage and current are almost constant in the entire length of the circuit. For such cases, common Ohm's and Kirchoff's laws suffice to describe the system. However, as the frequency is increased and the wavelength shrinks (typically microwaves), the voltage and current are time-dependent along the length of the circuit. This is entirely a consequence of the limited speed of light and information. In this high-frequency regime, for example, waves have a propagation velocity, can reflect at discontinuities in material properties and can dissipate as they propagate. The tools used to characterize circuits are thus different: We use telegraph equations, complex impedances that affect both phase and amplitude of electrical signals, and focus more on power transmission rather than currents. When reaching even higher frequencies, in the optical regime, material properties respond slightly differently (dissipation mechanisms may change for example), but the physics remains the same. However, the tools used to characterize this regime are then Maxwell's equations, and, for example, impedances become indices of refraction.

The THz region lies at the transition between the high-frequency electronics and photonics regions [58]. This region has been less explored due to the lack of efficient THz emitters, waveguides, and detectors, which is why the frequency range is termed the THz gap. In magnetism, THz waves have been recently used to induce ultrafast magnetization dynamics[45 59 57 60]. In this thesis, the whole spectrum of electromagnetic waves is covered for different purposes: the optical regime for the femtosecond laser pulses, low frequency regime for instrumentation, the high frequency regime for transmission line characterization and the THz regime for most of the experiments.

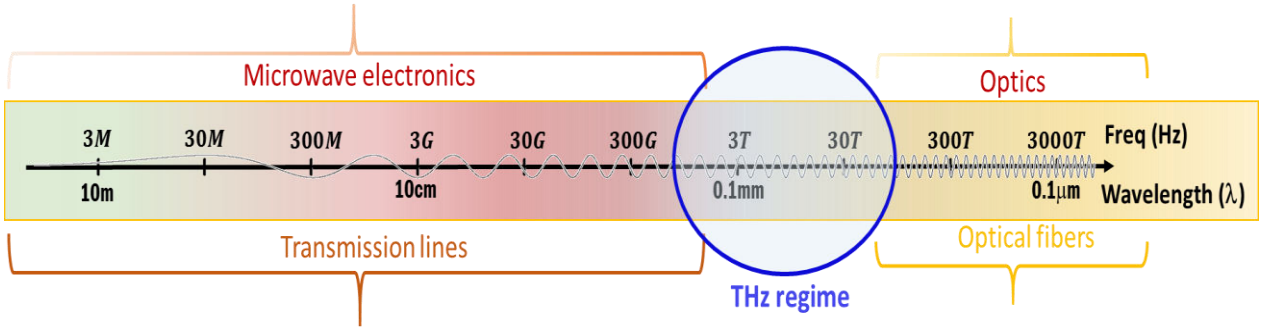

Figure 2.10 Schematic representation of the electromagnetic wave spectrum and its classification on the basis of detection techniques.

Wilson *et. al.* [57] in the year 2017, proposed a new approach to manipulate the magnetization of magnetic thin films using ultrashort electric charge current pulses of a few picoseconds. They used Auston photoconductive switches to generate the picosecond electrical pulses. Auston switches are semiconducting material-based photoconductive switches that have naturally a high resistivity. As soon as the switch is irradiated by a femtosecond laser light, valence band electrons are excited into the conduction band and, as a result, the conductivity increases leading to a "closing" of the switch. If a bias voltage is applied around the switch, the optical irradiation will result in a THz discharge. The pulse duration of the generated THz is dependent on various parameters such as femtosecond laser pulse duration, switch parameters such as its capacitance, and most importantly the relaxation time of the semiconducting material used for the switch design. The faster the relaxation time of the semiconductor, the shorter the generated THz pulse will be. Ideally, the first half of the THz/ps pulse is proportional to the temporal profile of the femtosecond laser pulse used to illuminate the photoconductive switch whereas the second half is dictated mostly by the relaxation time of the semiconducting material [61].

In the work reported by Wilson *et. al.* [57], they used low-temperature gallium arsenide (LT-GaAs) as the semiconducting material to fabricate the photoconductive switch and then coupled it with gold (Au) co-planar waveguide (CPW) to guide the generated THz in the preferred direction as shown in figure 2.11. To understand the femtosecond laser-induced ultrafast demagnetization, they deposited a 25μm×5μm magnetic material on the central Au line of the CPW at a distance of 0.5mm from the Auston switch. The idea behind this approach is to probe the TRMOKE response of the magnetic material as a result of ps wide electrical pulse arrival. For this study, they worked with Pt/Co/Pt multilayers. They performed TRMOKE measurement using both the optical (direct irradiation of femtosecond laser pulse) and electrical (picosecond pulse) pulses.

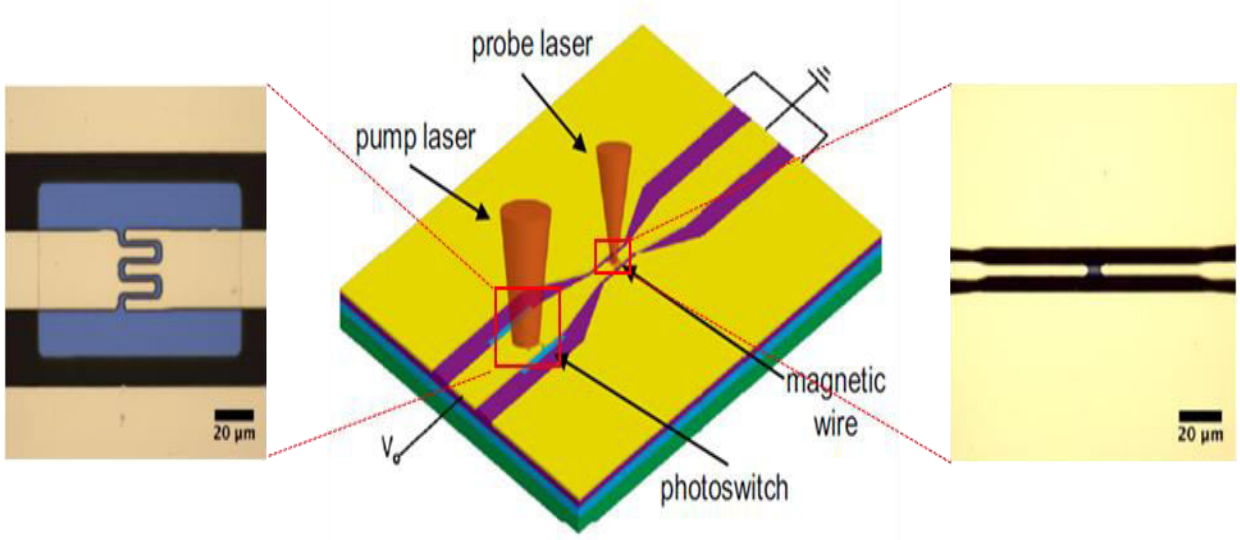

Figure 2.11 Schematic of the on-chip device to induce ultrafast demagnetization in Co/Pt multilayers [57].

Figure 2.12 (a) represents the TRMOKE response of the sample after optical excitation with a 2.6ps wide laser pulse. The shaded area represents the heat profile of the laser pulse, solid lines represents the predictions made by the three temperature model. Similarly, figure 2.12 (b) shows the evolution of the magnetization following a 5.5ps wide electrical pulse, demonstrating for the first time, picosecond current induced ultrafast demagnetization.

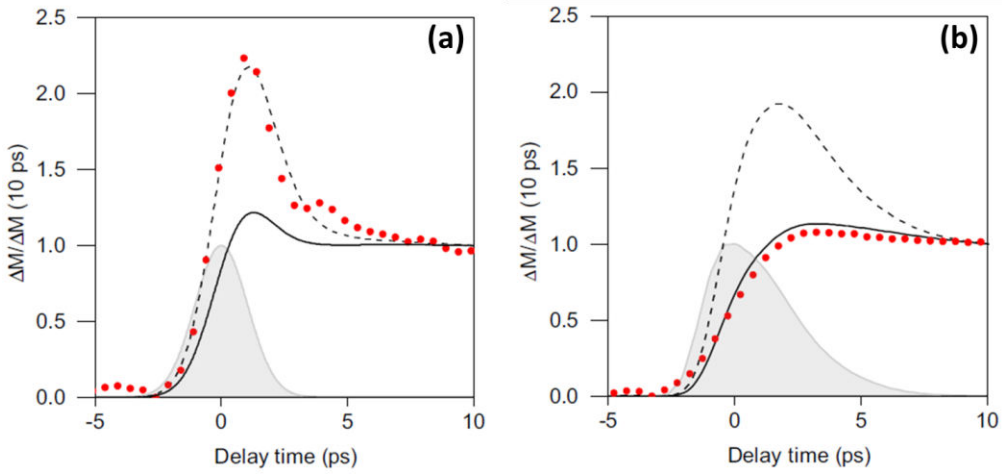

Figure 2.12 (a) Time-resolved magneto optic Kerr effect curves after the (a) optical and (b) electrical excitation [57].

The three temperature model shows poor consistency with the experimental data whereas, for electrical excitations, the theoretical prediction is in excellent agreement with the experimental data. The authors attributed this mismatch to the fact that an optical irradiation excites a few electrons at high energy levels resulting in a non-thermal distribution of the electronic population, whereas an electrical pulse induces a thermalized heating of the electronic bath. Because the three temperature model assumes thermalized baths at all times, the optical

excitation case poses important questions. The dashed lines in figure 2.12 represent the response of the system after reducing the electron-phonon coupling coefficient by 50 %, and fits well the optical data, suggesting reduced electron-phonon scattering rates for the highly excited few electrons. It is evident from the above study that the dynamics are highly dependent on the way we excite the system.

Just after this study, the same group [62], showed that electrically heating a GdFeCo ferrimagnet with such short (9 picosecond wide) electrical current pulses could allow to fully switch the magnetization. For this study, the authors used a co-planar stripline design, as shown in figure 2.13.

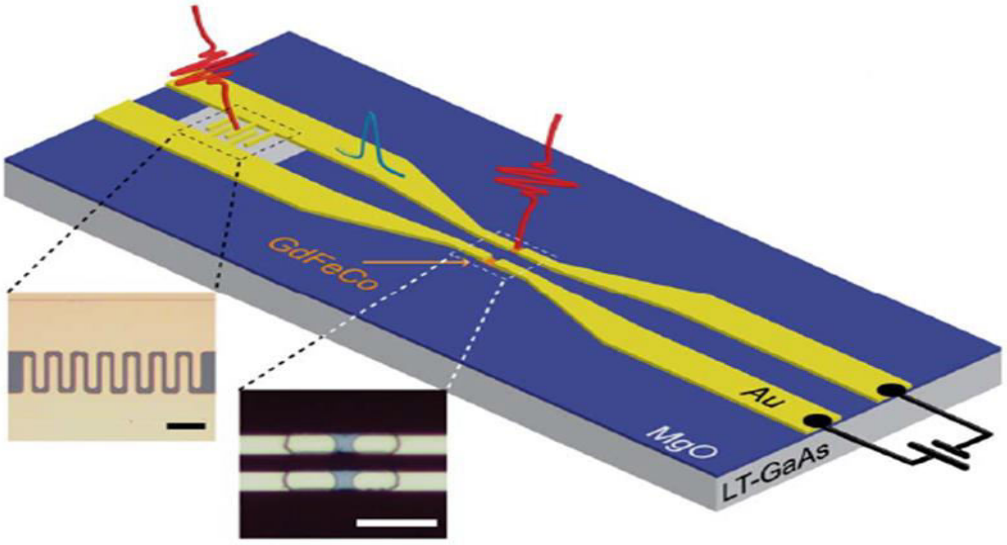

Figure 2.13 Schematic of the device with CPS to study ultrafast magnetization reversal of GdFeCo ferrimagnet using a single sub-picosecond wide electrical pulse [62].

For this study, they deposit Ta(5)/$Gd_{30}Fe_{63}Co_7$(20)/Pt(5) magnetic system on both the lines of CPS. Ta and Pt heavy metals are used to provide SOT to the GdFeCo layer.

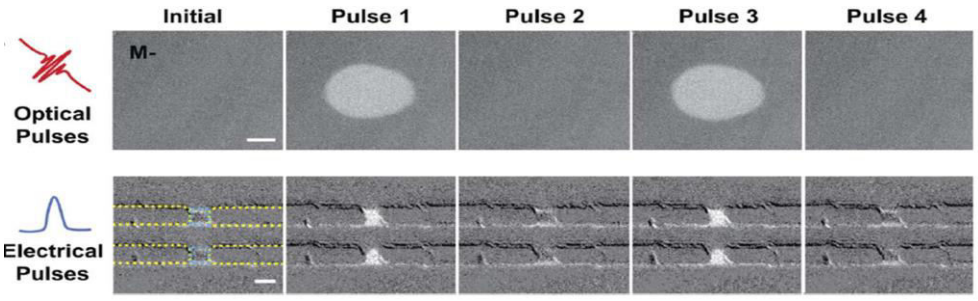

Figure 2.14 All-optical and electrical pulse induced toggle switching in GdFeCo thin film [62].

Figure 2.14 represents the switching outcome as a result of both optical and electrical excitations. The final spin state of the system keeps on toggling from up to down and vice versa

after the arrival of each pulse. Electrical pulse-induced switching results are the same as its optical counterpart which proves that the non-thermal distribution as a result of laser excitation is not mandatory for magnetization reversal instead, just the electrical heating is sufficient. Authors demonstrated through some simulations that the contribution of SOT in the toggle switching of GdFeCo was likely less than 10 % and hence does not play a major role in the ultrafast switching of this ferrimagnet in this particular structure. However, it would be interesting to study this kind of ferrimagnetic systems to attempt to combine these SOTs with the ultrafast heat-induced switching physics.

2.5 Conclusion

In this chapter, I have shown the material parameters and mechanisms that describe magnetization dynamics and magnetization reversal. I have shown the different time-scales or frequency windows that have been exploited in the literature, and the promising advantages of the use of the THz part of the spectrum. This thesis is a continuation of these latter studies where THz pulses generated via photoswitches are exploited for magnetization manipulation. The first major goal of the PhD has been to add spin currents into the picture, in order to induce ultrafast spin-torques (or spin-orbit torques), as well as the reciprocal magneto-resistance effects. To the best of my knowledge, there are not any work yet where such short spin current pulses have been generated in a wired geometry. In fact, most ultrafast spin injection studies to date have been performed via ultrafast laser-induced demagnetization experiments [63,64]. In such demagnetization experiments, the spin is pumped vertically through a multilayer [63,64], and doesn't allow for the measurement of spin-orbit torques. Another point of interest of the photoswitch approach, is the possibility of injecting a unipolar current (E field) pulse, which is impossible with light or free-space THz (where uni-directional effects are mostly due to the optical absorption and/or heat gradients). Having control over the polarity of pulses enables the control of the magnetic state to be written. All-in-all, we wish to push the understanding of spintronics by exploring the picosecond regime, and to enable new methods for ultrafast control and readout of a magnetic memories.

3

Methods

This chapter is divided into four sections. The first section includes the description of the sample fabrication process used during this thesis. The second section includes a brief introduction to various characterization tools used to study the static magnetic properties of the samples. The third section is a detailed description of the time-resolved magneto-optic Kerr effect (TRMOKE) setup which was built to study various dynamic thermal and magnetic properties of different magnetic systems in the picosecond and femtosecond time regimes. The final section is a description of the numerical model that predicts the magnetization dynamics.

*****

3.1 Device Fabrication

Sample preparation consists of three main steps, during which the photoconductive Auston switch, magnetic load and transmission lines are patterned. The device fabrication process starts with a 1cm×1cm so called *low temperature* gallium arsenide (LT-GaAs) substrate.

The device fabrication process starts with a 1cm×1cm so called *low temperature* gallium arsenide (LT-GaAs) substrate. The substrate is obtained by first depositing a GaAs (5nm)/$GaAl_{0.8}As$ (300nm) buffer layer on a semi-conducting GaAs (100) substrate using molecular beam epitaxy at 550 °C. Finally, a 1μm thick LT-GaAs is deposited at 260 °C. A schematic representation of a typical lithography step is shown in figure 3.1. Same recipe was used to perform lithography and lift-off for all three steps i.e. prior to exposure, substrate was spin-coated with an organic solvent solution MCC primer 80/20 and positive photoresists LOR 3A, S1813 for 40sec each using the spin coater 150. The MCC primer is required to maintain the adhesion between the substrate and the photoresists while the LOR3A is used as an additional photoresist to ensure the undercuts after the UV exposure.

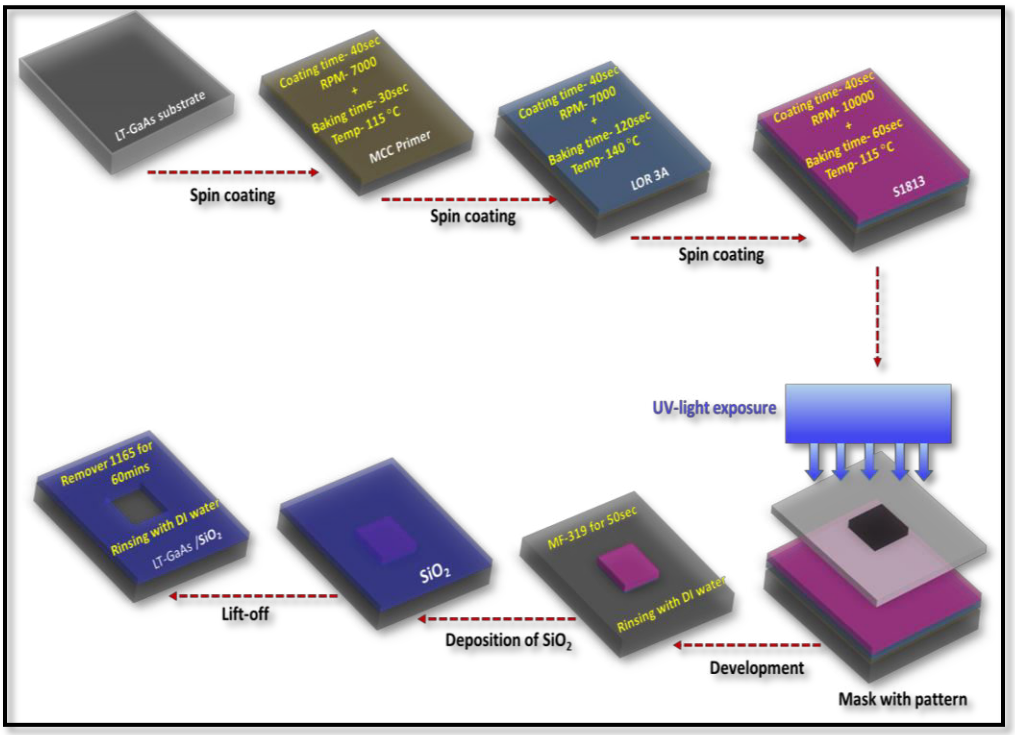

Figure 3.1 Schematic representation of the typical UV-lithography procedure used to pattern devices.

The spin coating parameters are shown in figure 3.1 where RPM represents the rotation per minute. The sample was then baked at different temperature for different time duration. After

each step of spin-coating, the sample was exposed to UV through the respective masks for 18sec using mask aligner MJB4 suss MicroTec. MF 319 developer was used for development for 50sec followed by rinsing with DI water for 20sec. After development, various deposition tools were used to deposit insulating (SiO_2) layer, magnetic load and gold transmission lines. After each step of deposition, lift-off was undertaken using remover 1165 by dipping the sample into it for 60mins followed by rinsing with DI water.

During the deposition of step 1 lithography, AC 450 (Alliance Concept) sputtering system was used to deposit 100nm thick oxide layer of SiO_2 in the presence of 20 SCCM Ar and O_2 flow at a base pressure of around 6×10^{3}mbar. The 100nm thick oxide layer is deposited to prevent shunting currents between the trasnmission lines' signal and ground lines. A small LT-GaAs window was patterned to have a photoconductive Auston switch which was used to generate ps wide electrical pulses [65].

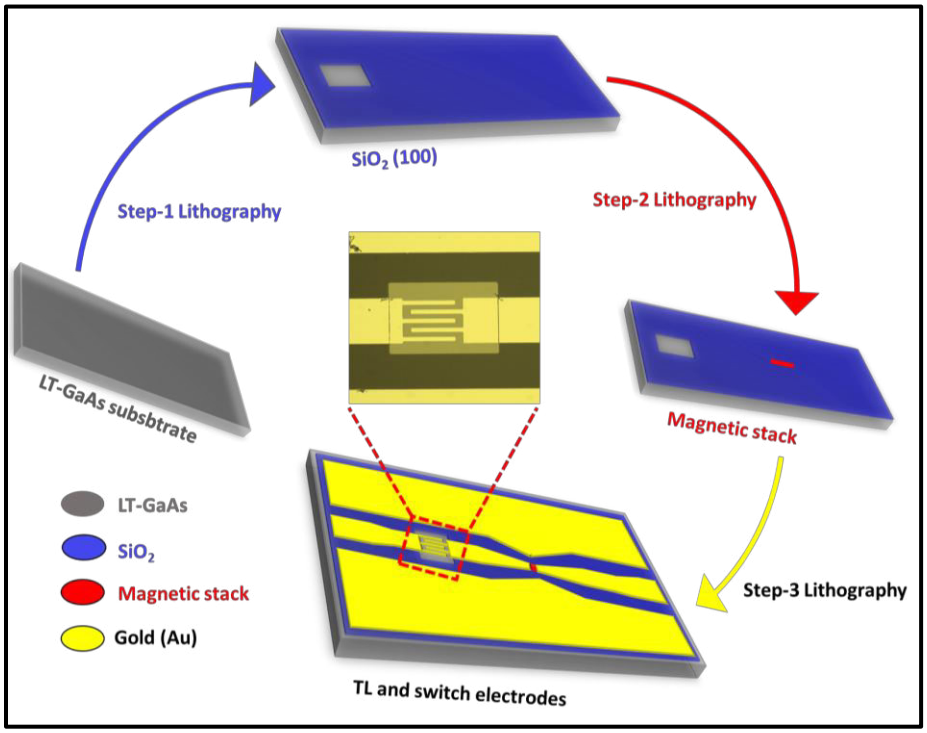

Figure 3.2 Schematic representation of each lithography step used to fabricate the on-chip THz device.

During the step 2 of lithography, the magnetic stack was deposited using DC magnetron sputtering in an AJA system. For results shown in chapter 4.2, a specific magnetic stack Ta(5nm)/Pt(4)/Co(1)/Cu(1)/Ta(4)/Pt(1) was deposited to study SOT switching in 1nm Co ferromagnet. Similiarly in chapter 4.1-4.3, various other magnetic stacks were undertaken to quantitatively understand the SOTs in ps time regime.

During step 3 of lithography, Ti(20nm)/Au(300nm) thick layer was deposited using e-beam evaporation for transmission line fabrication along with photoconductive switch electrodes. Ti(20nm) was deposited as a buffer layer to enhance the adhesion between the gold and the substrate along with improved quality of gold deposition. Gold was chosen for the transmission lines due to its electrical properties which helps to design impendence matched devices with the external electronics. A schematic representation of final output of every step is shown in figure 3.2.

Figure 3.3, shows the sample under microscope after the fabrication process. The first two devices from the top are the co-planar stripline (CPS) based on-chip THz devices along with the photoconductive and magnetic specimen on them. The rest of the devices are based on co-planar waveguide (CPW) structures with variation in photoconductive switch electrode geometry as well as magnetic load. Along with the THz devices, a big block of the magnetic stack is also available along with four gold electrodes to perform four-point electrical measurements. Although during this thesis work, the big magnetic block was used only during the all-optical TRMOKE measurements as mentioned earlier in this section.

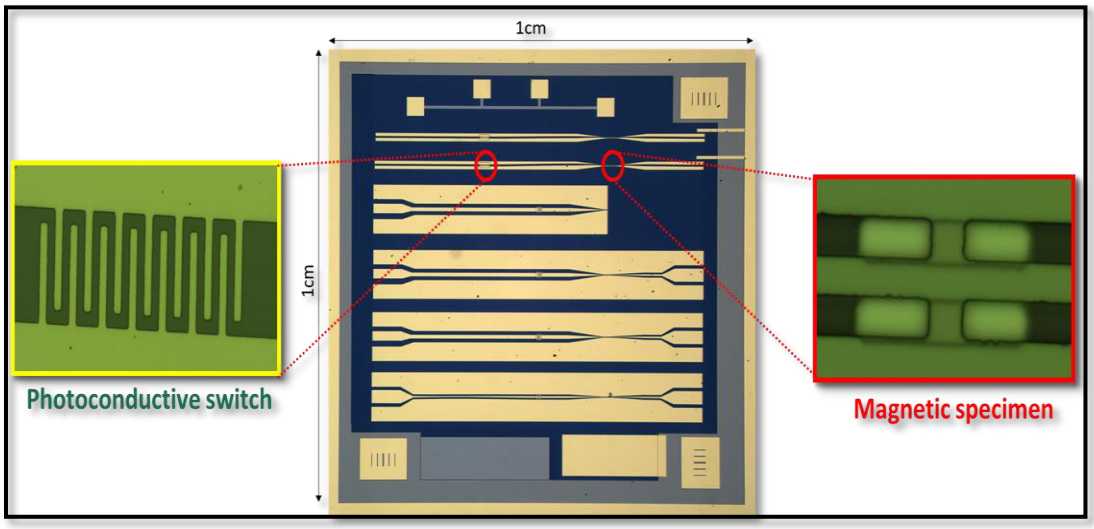

Figure 3.3 Sample image under the microscope by the end of fabrication steps

The Hall bars used in chapter 4 for quasi-static measurements, used a slightly different lithography approach. In particular, step 1 consisted in the patterning of the magnetic material performed via ion-beam etching. Also, the gold layer deposited for the electrical contacts had a thickness of only 150 nm.

After device fabrication, various characterization techniques have been used to study different static and dynamic magnetic responses of the magnetic specimen. Some of the static magnetic

measurement based techniques are mentioned briefly in section 3.2. A detailed explanation of the static and time-resolved magneto-optic Kerr effect (TRMOKE) is provided in section 3.2 and 3.3.

3.2 Static Characterization Techniques

Every time a magnetic stack has been deposited on LT-GaAs substrate during step 2 lithography, one additional glass or Si substrate has also been placed in the sputtering chamber to deposit a full film sample. The full film sample was then used to perform various static magnetic measurements such as SQUID vibrating sample magnetometry (VSM) to get the coercivity field (H_C), saturation magnetization (M_S). Magnetoresistance (MR) measurements were performed on the samples used in section 4.4 to study giant magnetoresistance (GMR). Hall measurements were undertaken to perform quasi-static magnetization reversal experiments. Magneto-Optical Kerr effect is explained in section 3.2.4 which has been largely used to take hysteresis loop measurements. Static MOKE microscopy setup is also briefly explained in this section which was used to record the magnetization reversal images of I nm thin Co ferromagnet using picosecond wide electrical pulses.

3.2.1 Vibrating sample magnetometry

Vibrating sample magnetometer (VSM) is a widely used technique both for scientific and industrial research. In order to measure the magnetic moment, the sample (and its associated magnetic flux) is vibrated in order to generate induction on a nearby pick-up coil. Samples are vibrated vertically via a piezoelectric transducer assembly. The generated induction on the coils is then proportional to the magnetic moment of the sample. In order to detect the small inductive signals, lock-in detection is typically used.

Since the magnetic thin films used in this thesis were extremely thin (1nm to 3nm), and therefore the magnetic flux was very small, a superconducting quantum interface device based vibrating sample magnetometer (SQUID-VSM) was used for most measurements to enhance the sensitivity. With a SQUID magnetometer, a sensitivity of ~10^{-8} emu can be achieved in comparison with a classical VSM system which has a limited sensitivity range i.e ~10^{-5}-10^{-6} emu. A SQUID magnetometer's high-sensitivity is achieved by measuring, similarly to interferometers, phase-shifts or interference patterns of electron waves (at superconducting temperatures). In the case of the SQUID, the magnetic field is responsible for the phase shift in the superconducting currents. The schematic of a typical VSM setup is shown in figure 3.4.

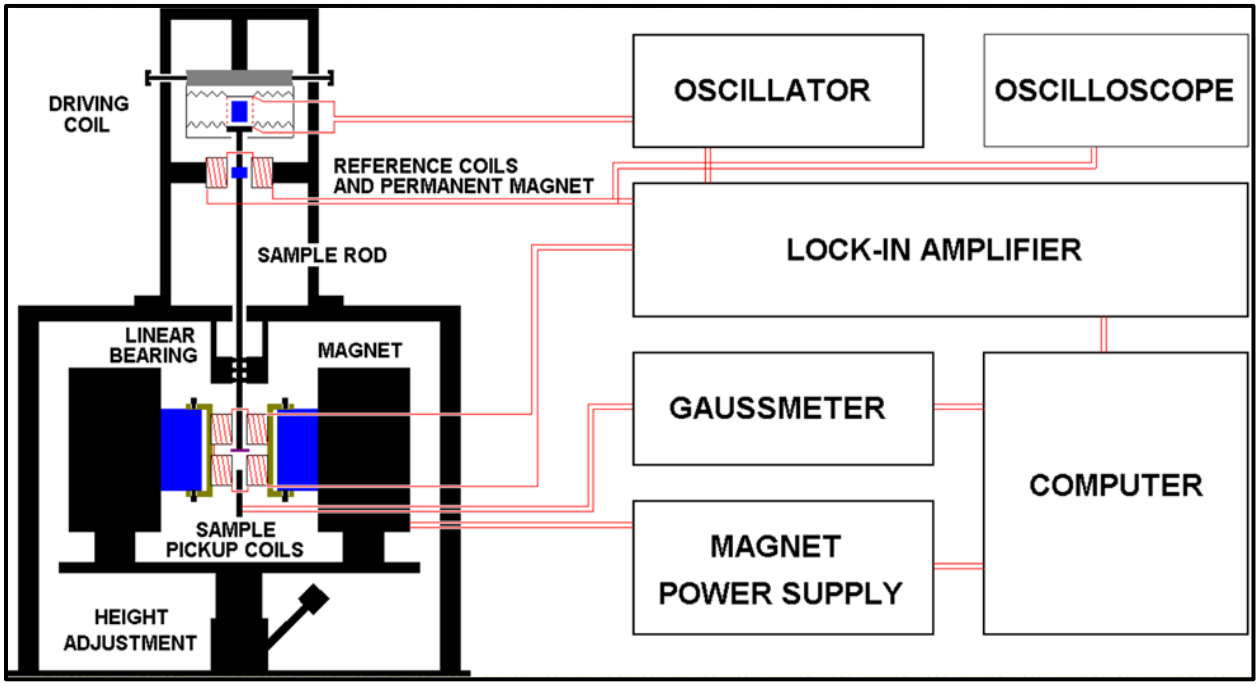

Figure 3.4 Schematic representation of the vibrating sample magnetometer (VSM) assembly

3.2.2 Magnetoresistance

Conventionally, a magnetoresistance effect is measured using an electrical four-probe method. This geometry allows to remove the contribution of the resistance of the leads. The change in the resistance with respect to the externally applied magnetic field can be studied simply by applying constant current (I) through two external probes and measuring the voltage through two internal probes. The ratio determines the resistance. Magnetoresistance is then computed using equation 3.1

$$MR = \frac{R(H) - R(0)}{R(0)} \qquad 3.1$$

Here, $R(H)$ and $R(0)$ are the resistances in the presence and absence of magnetic field (H), respectively. Depending on the magnetic properties of the magnetic multilayer, either in-plane (i.e. H in the film plane) or out of plane (i.e. H perpendicular to the film plane) can be used. In the in -plane case, two different geometries can be used: a) I parallel to H (longitudinal magnetoresistance) and b) I perpendicular to H (transverse magnetoresistance). These geometries are especially important when checking anisotropic magnetoresistance. The magnetoresistance can also be defined by two different magnetic states at zero applied field, if the sample has two stable remanant states. Contact probe-based magnetoresistance measurements have been undertaken in this thesis work where the pressure contacts were

made with the help of four needles as shown in figure 3.5(a). Figure 3.5(b) represents the schematic of the setup used to measure the giant magnetoresistance of the thin films used in chapter 4.4.

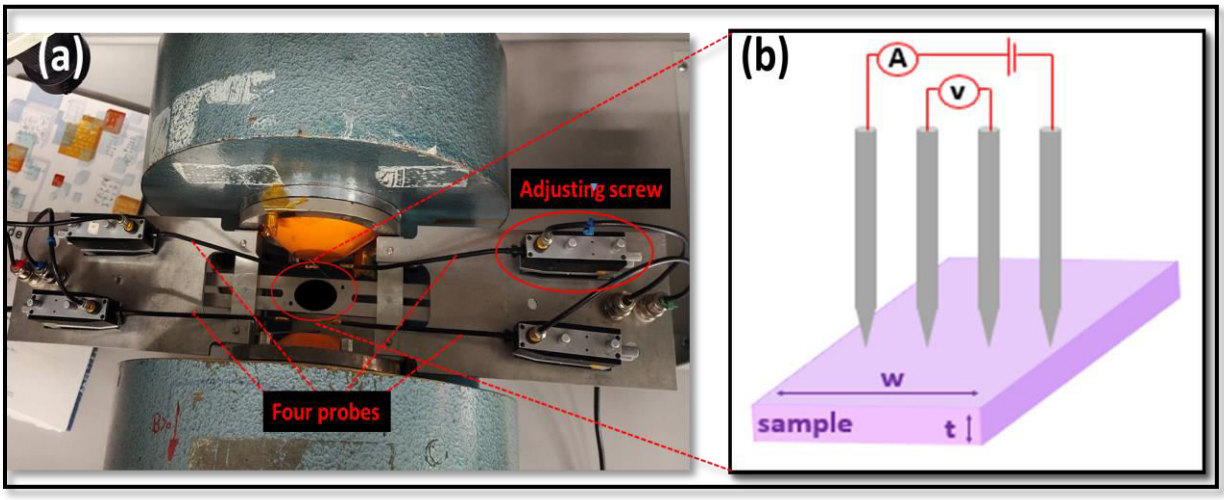

Figure 3.5 (a) View of the experimental setup and (b) schematic of the conventional four-probe method to measure magnetoresistance (MR)

3.2.3 Anomalous Hall effect

As mentioned in the introduction part of this chapter, Hall measurements have been undertaken to perform quasi-static switching studies. The schematic of a typical device structure used for Hall measurements is shown in figure 3.6(c) where the magnetic thin film system is patterned in a Hall geometry followed by depositing Au contact pads. Figure 3.6(a-b) represents the experimental setup used for the Hall measurement along with the patterned devices. The Hall voltage is measured on the orthogonal arms to the direction of applied current. In the case of our samples, which are ferromagnetic, we are sensitive to the anomalous Hall effect, and observed no ordinary Hall effect.

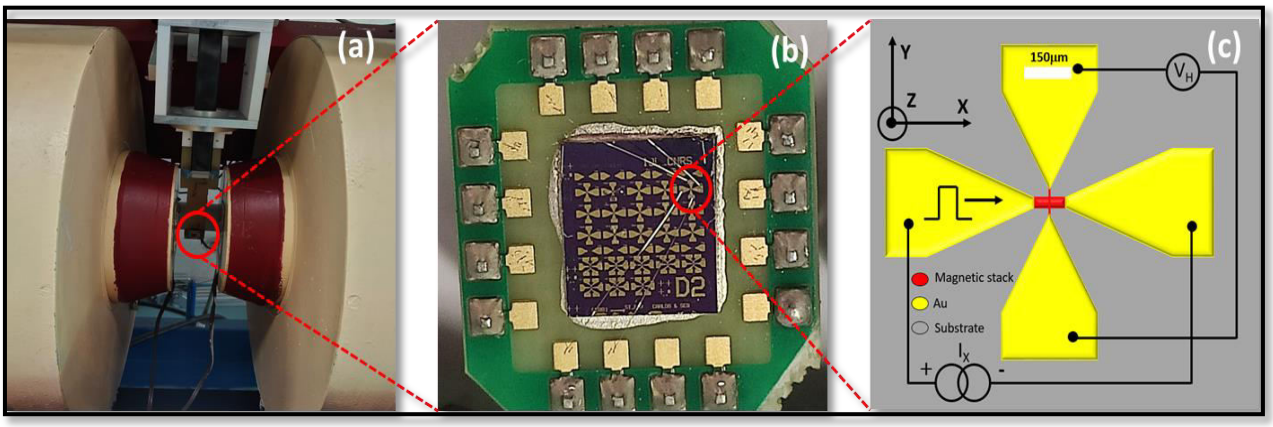

Figure 3.6 Planar Hall measurement (a) experimental setup, (b) device and (c) Schematic of Hall measurement

3.2.4 Magneto-Optical Kerr Effect magnetometry

3.2.4.1 Magneto-optical Kerr effect

The interaction of light with matter and magnetism has a long history. In the year 1845,Michael Faraday demonstrated the modification of the polarization of light after transmission through a piece of glass in the presence of an external magnetic field $\boldsymbol{H_{ext}}$, also known as the Faraday effect. He found that, when $\boldsymbol{H_{ext}}$ is applied along the light propagation direction, the axis of polarization of the transmitted light gets rotated by an angle proportional to $\boldsymbol{H_{ext}}$ [66]**.** Later in the year 1877, John Kerr demonstrated a similar effect in the reflection mode, namely the magneto-optical Kerr effect (MOKE) [67]. Magneto-optical effects are not limited to the interaction of electromagnetic waves with the magnet in the visible range, but can also be observed at ultraviolet, infrared, and microwave frequencies [67]. X-rays can also be employed to study element-specific magneto-optical effects [68]. Other magneto-optical effects have also been demonstrated such as the Voigt effect [69], Cotton Mouton effect [70]. However, the major advantage of the magneto-optical Kerr effect is its linear dependence with the magnetization's projection along a certain axis. Therefore, various magnetostatic properties can be easily accessed by measuring one component of the magnetization and sweeping the external magnetic field. Due to the small skin depth of the used visible-near IR light (10-20nm), the method is intrinsically surface sensitive, but can be considered as a bulk probe for ultrathin samples. A brief overview of the microscopic and macroscopic origin of magneto-optic Kerr effect is provided in this section.

The magneto-optic Kerr effect can be understood from the microscopic point of view by imagining the electronic system of the specimen as oscillating due to the interaction with light. Thereafter a force analogous to the Lorentz force induces a modification in the axis of vibration of the electrons. Hence the reflected light undergoes a change in the polarization that is related to the magnetization of the sample. This simplistic view is not accurate, as it does not capture the importance of the spin-orbit interaction in magneto-optics, but it portrays an intuitive way of thinking about magneto-optical phenomena.

A more accurate, but still phenomenological description of MOKE is the following: When an electromagnetic wave propagates through an isotropic media, the electric permittivity (ϵ) is a scalar quantity given by the expression ($\mathbf{D} = \epsilon\mathbf{E}$) since the electric field vector ($\mathbf{E}$) and the displacement vector ($\mathbf{D}$) remain parallel to each other. But due to magnetism, the medium

becomes anisotropic, and therefore this quantity is no longer a scalar but should be defined as a three-rank tensor as given by equation 3.2.

$$\epsilon = \begin{bmatrix} \epsilon_{xx} & \epsilon_{xy} & \epsilon_{xz} \\ \epsilon_{yx} & \epsilon_{yy} & \epsilon_{yz} \\ \epsilon_{zx} & \epsilon_{zy} & \epsilon_{zz} \end{bmatrix} \qquad 3.2$$

Because the magnetic field is not a time-invariant quantity (it breaks time-reversal symmetry), for anisotropic magnetic materials ϵ is no more Hermitian (i.e. $\epsilon_{ij} = -\epsilon_{ji}^{*}$) where ϵ_{ji}^{*} is the complex conjugate of ϵ_{ji}. Hence the electric permittivity tensor for such a system can be written as follows-

$$\epsilon = \begin{bmatrix} \epsilon_{xx} & \epsilon_{xy} & \epsilon_{xz} \\ -\epsilon_{xy} & \epsilon_{yy} & \epsilon_{yz} \\ -\epsilon_{xz} & -\epsilon_{yz} & \epsilon_{zz} \end{bmatrix} \qquad 3.3$$

Now if we consider the incoming light to be propagating along the z-direction, which is the case for the polar geometry of the setup used throughout this thesis (different MOKE detection geometries are explained later in this section), equation 3.3 takes a different form as given by equation 3.4. The diagonal terms do not contribute to the magnetic response of the material since magneto-optical effects are chiral in nature (i.e. they affect different circular polarized components differently) and are thus embodied in the cross terms xy, yz , xz, unlike linearly anisotropic effects (for example: linear birefringence). In most cases, we can safely assume that these cross terms are proportional to the magnetization of the system.

$$\epsilon = \begin{bmatrix} \epsilon_{xx} & \epsilon_{xy} & 0 \\ -\epsilon_{xy} & \epsilon_{xx} & 0 \\ 0 & 0 & \epsilon_{xx} \end{bmatrix} \qquad 3.4$$

The normalized eigenmodes of ϵ for the above tensor matrix are as represented in equation 3.5 where E_x and E_y are the electric fields in x and y direction respectively. These eigenmodes with eigenvalues ($\epsilon = \epsilon_{xx} \pm i\epsilon_{xy}$), correspond to the response of the medium to left (LCP) and right (RCP) hand circularly polarized light respectively. The latter two circular polarization states are defined as

$$\begin{bmatrix} \mathrm{E}_x \\ \mathrm{E}_y \end{bmatrix}_{\pm} = \frac{\mathbf{1}}{\sqrt{\mathbf{2}}} \begin{bmatrix} 1 \\ \pm i \end{bmatrix} \qquad 3.5$$

This shows that the complex refractive index of the magnetic material experienced by LCP and RCP will be different. As a result, a linearly polarized light undergoes a change (i.e. complex rotation of polarization) after reflection from a magnetic material and becomes elliptically polarized. The complex rotation Θ as represented by equation 3.6 can be written in terms of the

real part known as Kerr rotation (θ_k) and an imaginary part Kerr ellipticity (ε_K), both parts being proportional to the magnetization.

$$\Theta = \theta_k + i\varepsilon_K \qquad 3.6$$

Depending on the orientation of magnetization (**M)** of the specimen with the plane of incidence of light, different MOKE geometries can be employed. These geometries are classified mainly into three categories as shown in figure 3.7: (a) Polar, (b) Longitudinal, and (c) Transverse MOKE geometries. Longitudinal geometry is sensitive to both the in-plane and out-of-plane projections of the magnetization (the sensitivity depends on the projection of the k vector on **M**) whereas the polar geometry is only sensitive to the out-of-plane projection. A third configuration can be employed which is sensitive to the transverse in-plane magnetization, named the transverse MOKE geometry. In this case, the magnetization does not induce a modification of the polarization but rather a change in the reflectivity.

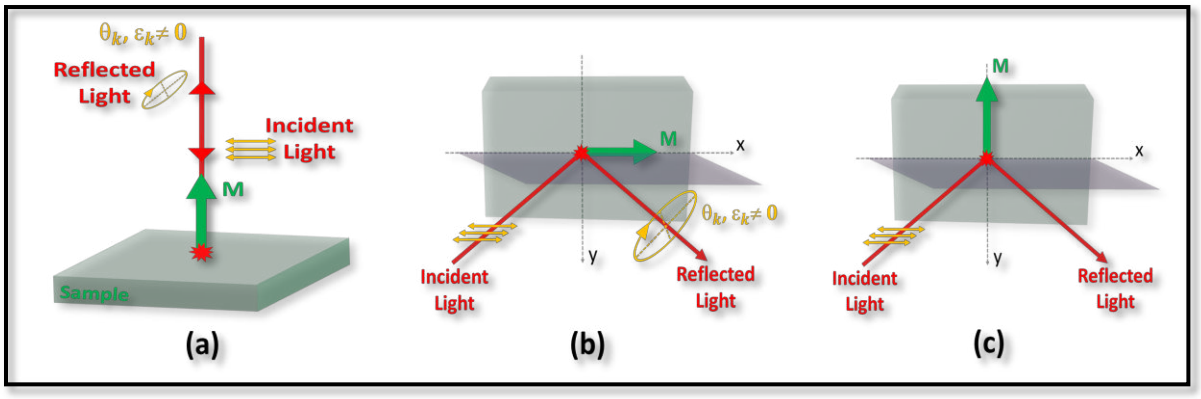

Figure 3.7 Schematic representation of (a) Polar, (b) longitudinal, and (c) transversal MOKE geometries. Planes of incidence are in purple.

In order to detect the small changes in polarization various experimental techniques can be used, some of which will be explained in the next sections.

3.2.4.2 Optical components of a MOKE setup

The basic elements required to detect the MOKE rotation are the light source, two polarizers and a detector. Light is first linearly polarized by a first polarizer, and after reflection on the sample, a second polarizer (named the analyzer) is used to convert the polarization changes into intensity changes that are then detected with the photodetector.

MOKE signal can also be detected with spatial resolution (using a microscope) and/or time-resolution (using pulsed sources). The microscope enables the observation of magnetic domains, and time-resolved experiments unveil the dynamics of the magnetic system after an

excitation. Both these approaches have been widely used during this thesis work. In this section, a static MOKE detection setup (shown in figure 3.8) is explained with a brief description of its basic components.

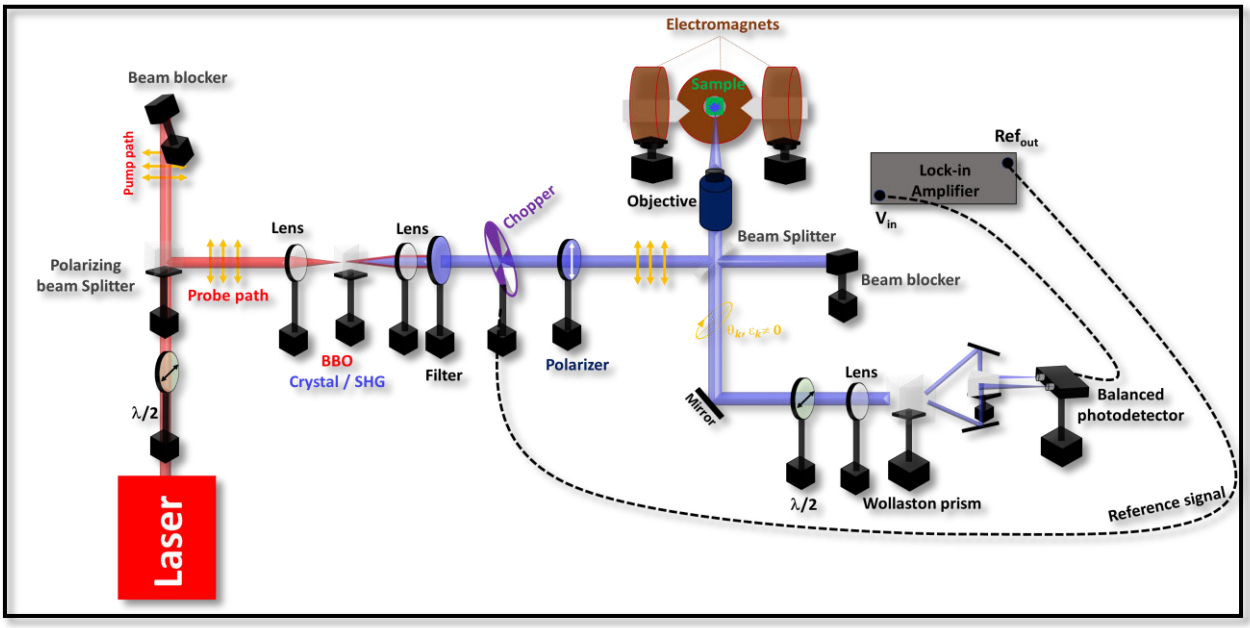

Figure 3.8 Schematic of static Magneto-optic Kerr effect (MOKE) detection setup

Polarizers and beam splitters:

For the optical setup built and used during this thesis work, different types of polarizers and beam splitters have been used. Glan type polarizers with high extinction ratio (>10^5:1) were used in the setup to ensure a linear polarization. A polarizing beam splitter, was used to split the incident laser beam into two different (s and p polarized respectively) beams namely the probe and the pump to study the time-resolved magneto-optical Kerr effect as explained in section 3.3. A non-polarizing beam splitter, which reflects 20 % of incident light and transmits 80 % independently of its polarization, has been employed in the probe path just before the sample and the objective. The high transmission to reflection ratio based beam splitter was chosen to extract the maximum amount of signal that is reflected from the sample since it includes the magnetic information of the sample. The Wollaston polarizer was used in the detection path to separate the s and p components of the reflected probe and direct them towards the double photodiode balanced detector.

Waveplates/ retarders:

Waveplates or retarders are birefringent materials used to rotate or change the polarization of the transmitted light by introducing a phase difference between two linearly polarized and

orthogonal light components. Two of the well-known waveplates are the half-wave (λ/2) and quarter-wave (λ/4) plates. Half waveplate (λ/2 rotates the incident polarization by an angle 2ϕ, where ϕ is the angle between the plane of polarization of the incident light beam with that of the fast axis of the waveplate. Half waveplates are usually placed just before a polarizer to control the output intensity which is being transmitted through the polarizer. For example, we use a half waveplate in the detection path to ensure equal distribution of intensities for s and p components transmitted through the Wollaston polarizer. This equal distribution of power is essential to enhance the signal to noise ratio while using the balanced detection technique (explained in later section). The quarter waveplate (λ/4) changes the linear polarization of light into circular polarization and vice versa. A quarter waveplate is sometimes used instead of the half waveplate to detect the Kerr ellipticity (ε) signal instead of the Kerr rotation (θ_k) [71].

Optical modulator:

Modulation is a common method in electronics and optics to filter out noise and detect small signals. Here, to extract the signal of interest, an optical beam is being modulated at a particular frequency which is provided as the reference to a lock-in amplifier. The lock-in amplifier will output a voltage proportional to the signal at said reference frequency, filtering out most of the noise that can be found at other frequencies. This is particularly useful to get rid of the high noise at low frequency (1/f noise) found in common electronics such as the optical detector. In general, the higher the frequency of modulation, the lower the 1/f noise will be, with the experimental setup eventually reaching the shot-noise limit [72]. Chopper, electro-optic modulator (EOM), photo-elastic modulator (PEM) can be used to modulate the optical signal through mechanical, electro-optic, and photo-elastic means respectively.

For static MOKE measurements taken during the thesis work, optical chopper was employed which modulates the optical signal mechanically at a frequency of choice between 50 and 400Hz. The electro-optic modulator (EOM) was used at a modulation frequency of 1-3MHz during the time-resolved magneto-optical Kerr effect (TRMOKE), time-domain thermal reflectance (TDTR) measurements (discussed in later sections). Sometimes a double modulation scheme (using both the optical chopper and the EOM) was also employed to further reduce the noise levels and also to get rid of the stray light-induced signals.

Photodetector:

A balanced photodetection approach is employed to further enhance the sensitivity of the setup by suppressing the laser-noise. In this approach, an assembly of two photodiodes is used instead of a single photodetector. The laser beam is split into two separate beams of similar

intensity using the half waveplate and Wollaston polarizer (as mentioned earlier). The output currents from each photodiode goes through a differential operational amplifier which rejects the common fluctuation that is present in both signals (i.e. noise).

Moreover, the used photodetector relies on three different transimpedance operational amplifiers in order to get three different voltage outputs namely the monitor +, monitor –, and the RF output as shown in the function block diagram of the photodetector in figure 3.9. The voltage output at monitor+, monitor – is simply a product of the photocurrent (I^{DC}) and the internal transimpedance gain (g) of each photodiode.

The RF port output (V_{RF}) is the voltage signal proportional to the difference of the photocurrents (or the optical powers) across the two photodiodes. The currents generated at each photodiode I_+ and I_- (before amplification) and the voltages at each output (after amplification) are given in equation 3.7.

$$I_+ = P_+ R_M \rightarrow V_+ = I_+ g \qquad 3.7$$

$$I_- = P_- R_M \rightarrow V_- = I_- g$$

$$V_{RF} = (I_+ - I_-) G$$

Here P_+ and P_- represent the optical input powers at each photodiode. R_{M} in units of Amps/Watt is the responsivity of the photodiodes which is a function of the wavelength of the optical input signal. The factors g and G represent the transimpedence gain of the monitors and RF operational amplifiers, respectively. We note that the gain G can be externally set from 10^3-10^7 (V/A).

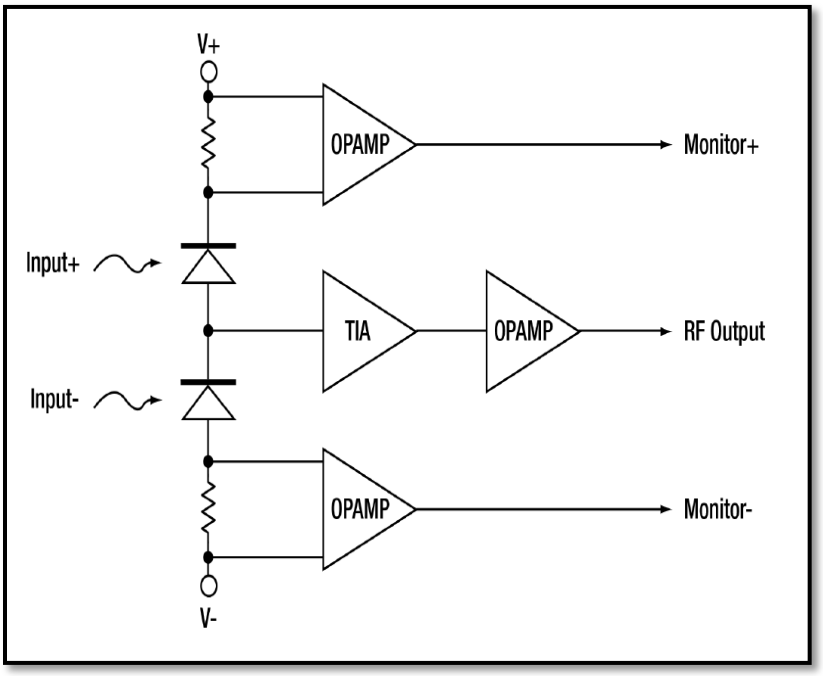

Figure 3.9 Functional block diagram of PDB450A-AC balanced photodetector

Beta borium borate (BBO) crystal:

BBO crystals are also birefringent optical materials used for non-linear applications such as second harmonic generation. BBO crystal was used in the probe path to change the wavelength of the optical beam from 800nm to 400nm using the second harmonic generation technique.

3.2.4.3 Calibration of Kerr rotation:

To find the relationship between the measured voltage and the Kerr rotation (θ_k), first the Jones matrix formalism can be applied to find both components of the light's electric field ($\mathbf{E_x}$, $\mathbf{E_y}$) after reflection on the sample and transmission through the optics.

$$\begin{bmatrix} \mathbf{E_x} \\ \mathbf{E_y} \end{bmatrix} = -i\sqrt{T_0}[\mathrm{HWP}][\mathrm{S}] \begin{bmatrix} \mathbf{E_0} \\ 0 \end{bmatrix} \qquad 3.8$$

$$\begin{bmatrix} \mathbf{E_x} \\ \mathbf{E_y} \end{bmatrix} = -\boldsymbol{i}\sqrt{T_0} \begin{bmatrix} \cos 2\phi & \sin 2\phi \\ \sin 2\phi & -\cos 2\phi \end{bmatrix} \begin{bmatrix} r_{pp} & r_{ps} \\ r_{sp} & r_{ss} \end{bmatrix} \begin{bmatrix} \mathbf{E_0} \\ 0 \end{bmatrix} \qquad 3.9$$

Here, $-\boldsymbol{i}\sqrt{T_0}$ represents the DC component corresponding to the transmission coefficient of all the optical elements used between the sample and the detector, $[\mathrm{HWP}]$ and $[\mathrm{S}]$ represents the two-dimensional jones matrices for the half-waveplate and the sample respectively. ϕ is the angle between the fast axis of the HWP and the horizontal direction x. For MOKE measurements, the HWP is rotated at $\phi \approx \frac{\pi}{8}$ such that the horizontal and the vertical electrical

field components are roughly equal. The term $\begin{bmatrix} \mathbf{E_0} \\ 0 \end{bmatrix}$, represents the p-polarized light incidence at the sample. Wollaston polarizer placed after the HWP separates the x and y components and directs them towards the balanced photodetector. Equation 3.9 can be re-written as follows

$$\begin{bmatrix} \mathbf{E_x} \\ \mathbf{E_y} \end{bmatrix} = -\boldsymbol{i}\sqrt{T_0}\begin{bmatrix} 1/\sqrt{2} & 1/\sqrt{2} \\ 1/\sqrt{2} & -1/\sqrt{2} \end{bmatrix}\begin{bmatrix} r_{pp} & r_{ps} \\ r_{sp} & r_{ss} \end{bmatrix}\begin{bmatrix} \mathbf{E_0} \\ 0 \end{bmatrix} \qquad 3.10$$

$$\begin{bmatrix} \mathbf{E_x} \\ \mathbf{E_y} \end{bmatrix} = \frac{-\boldsymbol{i}\sqrt{T_0}}{\sqrt{2}}\begin{bmatrix} r_{pp} + r_{sp} & r_{ps} + r_{ss} \\ r_{pp} - r_{sp} & r_{ps} - r_{ss} \end{bmatrix}\begin{bmatrix} \mathbf{E_0} \\ 0 \end{bmatrix} \qquad 3.11$$

$$\begin{bmatrix} \mathbf{E_x} \\ \mathbf{E_y} \end{bmatrix} = \frac{-\boldsymbol{i}\,\mathbf{E_0}\sqrt{T_0}}{\sqrt{2}}\begin{bmatrix} r_{pp} + r_{sp} \\ r_{pp} - r_{sp} \end{bmatrix} \qquad 3.12$$

The electrical field components (E_x) and (E_y) can then be written as $-\mathrm{i}\boldsymbol{E_0}\sqrt{T_0}/\sqrt{2}\left(r_{pp} + r_{sp}\right)$ and $-\mathrm{i}\boldsymbol{E_0}\sqrt{T_0}/\sqrt{2}\left(r_{pp} - r_{sp}\right)$ along with their complex conjugates $\mathrm{i}\boldsymbol{E_0^*}\sqrt{T_0}/\sqrt{2}\left(r_{pp}^* + r_{sp}^*\right)$ and $\mathrm{i}\boldsymbol{E_0^*}\sqrt{T_0}/\sqrt{2}\left(r_{pp}^* - r_{sp}^*\right)$ respectively. Since the power is proportional to $\boldsymbol{E}\boldsymbol{E}^*$ and hence the terms $\boldsymbol{E_x}\,\boldsymbol{E_x^*}$ and $\boldsymbol{E_y}\,\boldsymbol{E_y^*}$ can be written as follows

$$\boldsymbol{E_x}\,\boldsymbol{E_x^*} = \frac{\boldsymbol{E_0}\,\boldsymbol{E_0^*}\,T_0}{2}\left(r_{pp}r_{pp}^* + r_{pp}r_{sp}^* + r_{sp}r_{pp}^* + r_{sp}r_{sp}^*\right); \qquad 3.13$$

$$\boldsymbol{E_y}\,\boldsymbol{E_y^*} = \frac{\boldsymbol{E_0}\,\boldsymbol{E_0^*}\,T_0}{2}\left(r_{pp}r_{pp}^* - r_{pp}r_{sp}^* - r_{sp}r_{pp}^* + r_{sp}r_{sp}^*\right)$$

In a propagating sinusoidal linearly polarized electromagnetic plane wave of a fixed frequency (monochromatic), the Poynting vector points in the direction of propagation. The intensity of the wave corresponds to the time-averaged magnitude of the Poynting vector which corresponds to

$$I = \langle S \rangle = \frac{1}{2\eta}|E|^2 = \frac{1}{2\eta}EE^* \qquad 3.14$$

where E is the complex amplitude of the electric field and η is the characteristic impedance of the transmission medium, $\eta_0 \approx 377\ \Omega$ for a plane wave in free space. The power corresponds to the integral of the intensity over the full beam size, which for a Gaussian beam is equal to $P = I\pi w^2/2$, where w is the beam radius ($1/e^2$ definition). Consequently, the power incident on each of the inputs of the balanced photodetector are equal to,

$$\begin{bmatrix} P_+ \\ P_- \end{bmatrix} = \frac{\pi w^2}{4\eta}\begin{bmatrix} \boldsymbol{E_x}\,\boldsymbol{E_x^*} \\ \boldsymbol{E_y}\,\boldsymbol{E_y^*} \end{bmatrix} = \frac{P_0 T_0}{2}\begin{bmatrix} \left(r_{pp}r_{pp}^* + r_{pp}r_{sp}^* + r_{sp}r_{pp}^* + r_{sp}r_{sp}^*\right) \\ \left(r_{pp}r_{pp}^* - r_{pp}r_{sp}^* - r_{sp}r_{pp}^* + r_{sp}r_{sp}^*\right) \end{bmatrix} \qquad 3.15$$

Where power $P_0 = (\pi w^2/4\eta)\boldsymbol{E_0}\,\boldsymbol{E_0^*}$ is the probe power incident on the sample. Using equations 3.7, the output voltages V_+ and V_- and V_{RF} of the balanced detector are

$$\begin{bmatrix} V_+ \\ V_- \end{bmatrix} = \frac{P_0\, T_0\, R_M g}{2} \begin{bmatrix} r_{pp}r_{pp}^* + r_{pp}r_{sp}^* + r_{sp}r_{pp}^* + r_{sp}r_{sp}^* \\ r_{pp}r_{pp}^* - r_{pp}r_{sp}^* - r_{sp}r_{pp}^* + r_{sp}r_{sp}^* \end{bmatrix} \qquad 3.16$$

and,

$$V_{RF} = P_0\, T_0\, R_M G(\, r_{pp}r_{sp}^* + r_{sp}r_{pp}^*) \qquad 3.17$$

Replacing $r_{pp} = |r_{pp}|\exp(i\phi_{pp})$; $r_{sp} = |r_{sp}|\exp(i\phi_{sp})$; $r_{sp}^* = |r_{sp}|\exp(-i\phi_{sp})$; $r_{sp} = |r_{sp}|\exp\left(-i\phi_{sp}\right)$, and assuming that $r_{pp} \gg r_{sp}$ which holds if the Kerr rotation is small, then the output voltages can be re-written as below.

$$V_+ = V_- = \frac{P_0\, T_0\, R_M g}{2}\, |r_{pp}|^2 \qquad 3.18$$

$$V_{RF} = 2P_0\, T_0\, R_M G\, |r_{pp}|\, |r_{Sp}| \cos(\phi_{sp} - \phi_{pp}) \qquad 3.19$$

The complex Kerr rotation Θ given by equation 3.6 can also be represented in terms of Fresnel coefficients r_{pp} and r_{sp} as below.

$$\Theta = \theta_k + \boldsymbol{i}\varepsilon = \frac{r_{sp}}{r_{pp}} = \frac{|r_{sp}|}{|r_{pp}|}(\cos(\phi_{sp} - \phi_{pp}) + i \sin(\phi_{sp} - \phi_{pp}) \qquad 3.20$$

Therefore, equation 3.19 can be written as,

$$V_{RF} = 2P_0\, T_0\, R_M G\, |r_{pp}|^2 \theta_k \qquad 3.21$$

We can measure the monitor voltages V_+ and V_- with a low bandwidth voltmeter. The RF voltage is preferably measured at high frequency in order to reduce the $1/f$ electronic noise. To this aim, we first need to modulate the optical signal at said frequency f (pulsation ω) and then use demodulation (also termed downconversion or phase sensitive detection) of the measured voltage via a lock-in amplifier.

For static MOKE experiments such as the characterization of magnetic hysteresis cycles, the probe beam is modulated by a mechanical chopper at a frequency of f~50-400 Hz. The chopper induces a square-wave modulation on the transmission T_{ch} of the probe given by,

$$T_{ch} = \frac{1}{2} + \frac{1}{2}\frac{4}{\pi}\left(sin(\omega_{ch}t) + \frac{1}{3}sin(3\omega_{ch}t) + \frac{1}{5}sin(5\omega_{ch}t) \ldots\right) \qquad 3.22$$

Under modulation, the total transmission T_0 in equation 3.19 becomes $T_0 T_{ch}$. The lock-In then demodulates the component of the signal V_{RF} at ω, and outputs the root mean square (RMS) voltage (for a sine wave, we divide by $\sqrt{2}$ the amplitude), which results in a measured in-phase voltage V_{IP} given by-

$$V_{IP} = \frac{1}{\sqrt{2}} 2 \frac{P_0}{2} \frac{4}{\pi} T_0 R_M G |r_{pp}|^2 \theta_k \qquad 3.23$$

$$V_{IP} = 2\sqrt{2} \frac{P_0}{\pi} T_0 R_M G |r_{pp}|^2 \theta_k \qquad 3.24$$

A calibration relation can be evaluated by dividing the in-phase detected voltage from equation 3.24 by the monitor voltages from equation 3.18,

$$\frac{V_{IP}}{V_+} = \frac{4}{\pi} \sqrt{2} \frac{G}{g} \theta_k \qquad 3.25$$

The total Kerr rotation ($2\theta_k$) can be evaluated by subtracting the measurement taken for both the orientations of the sample's magnetic moment i.e. ${\theta_k}^+ - {\theta_k}^-$.

$${\theta_k}^+ - {\theta_k}^- = 2\theta_k = \frac{\pi}{4\sqrt{2}} \frac{g}{G} \left(\frac{{V_{IP}}^+ - {V_{IP}}^-}{V_+} \right) \qquad 3.26$$

The above relation between V_{IP} and θ_k was also verified experimentally by rotating the half waveplate ($\lambda/2$) by a known angle and monitoring the Lock-in amplifier output voltage signal, as shown in figure 3.10.

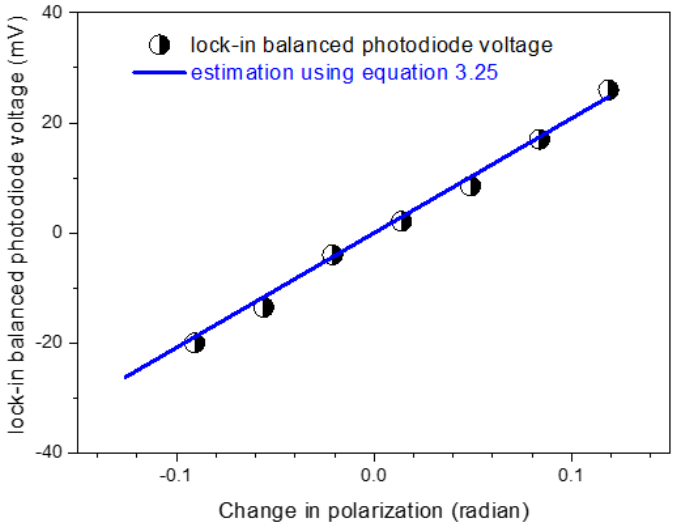

Figure 3.10 Calibration curve for experimental verification of V_{IP} versus θ_k

3.2.4.4 Magnetic hysteresis loops:

On our setup, a maximum external magnetic field of ~ 200mT can be achieved in both the in-plane (IP) and the out-of-plane (OOP) directions to the sample plane using an assembly of electromagnets. Figure 3.11 (a-b) represents the hysteresis loop measurement in polar MOKE geometry for a 1 nm and 3nm thin cobalt layer respectively. The black curve presented in figure 3.11(a-b) is tilted at some angle due to the presence of the Faraday effect since some of the optical elements such as the objective are placed very close to the electromagnet. In figure 3.11(a) we plot the Kerr rotation of a 1nm thick Co sample as a function of an external out-of-plane magnetic field. The sharp transitions and the hysteretical reversal are a signature of the perpendicular magnetic anisotropy. In figure 3.11(b) a 3nm thick Co layer with in-plane anisotropy is studied. Because the field is applied along the hard axis and is smaller than the anisotropy field, we cannot observe any saturation. Blue curves represent the final magnetic response of the Co thin films after eliminating the contribution of the Faraday effect. To eliminate the Faraday effect contribution, MOKE hysteresis measurements were taken on non-magnetic and highly reflective metals (Ag, Cu) separately and then the response was subtracted from the magnetic sample output. The asymmetry around "0" in the data along the y-axis is attributed to the slight imbalance between the two beams entering into the photodiodes. This imbalance can be fixed easily by rotating the half waveplate ($\lambda/2$) that is placed just before the Wollaston polarizer.

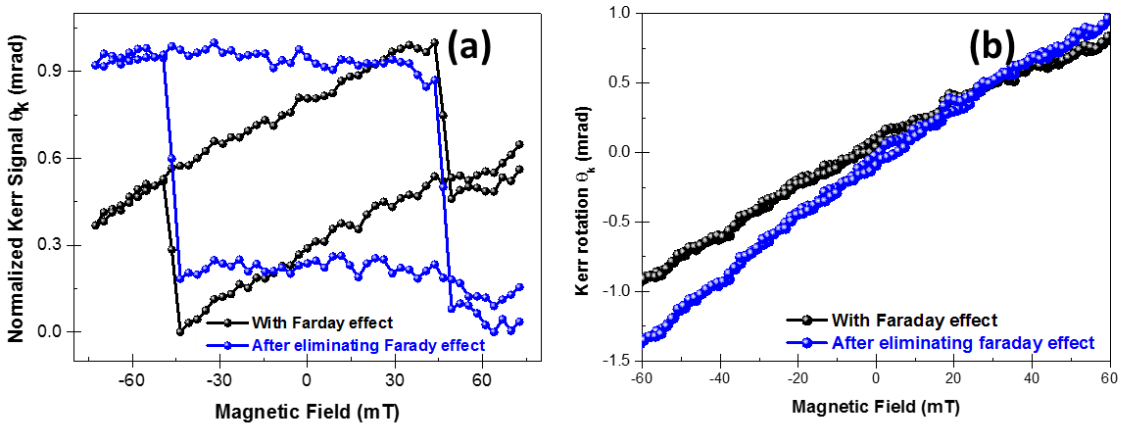

Figure 3.11 Polar MOKE hysteresis loop of (a) 1nm and (b) 3nm thin Co layer before and after eliminating the Faraday effect contribution

3.2.4.5 MOKE microscopy

A schematic diagram of the Kerr microscopy section of the optical detection setup is represented in figure 3.12. The basic components used for the MOKE microscopy setup are: LED

source, lenses, pin hole, polarizer, objective, analyzer, camera. Kohler illumination was ensured using a pair of lenses and a pin hole and by focusing the illumination beam at the back focal plane of the objective. The angle between the polarizer and the analyzer is kept around 90 degrees (almost crossed) to get the maximum sensitivity of the magnetic contrast. An optical filter was also employed in the detection path to block the laser beam from entering into the camera. The camera is 6fps monochrome CCD.

The microscope was required to work with the transmission line devices and focus the probe to the small magnetic regions. A flipper mirror was used in the detection path to switch from one experimental configuration to another (laser MOKE to Kerr microscopy). Depending on the type of experiments, different objectives (×10, ×20, ×50) were used. For example, to detect the electrical pump induced responses, ×50 objective was used to better focus the probe beam on the magnetic specimen. When performing MOKE imaging, due to the highly reflective Au transmission lines that are next to the magnetic section, we are very susceptible to pixel overflowing. This means the exposure time has to be kept short, which results in an important degradation of the magneto-optical signal. As a solution we use 8x binning, without loss of spatial resolution, to speed up the camera up to 15fps and average 60 images to reduce noise and boost back the signal to noise ratio. Finally, mechanical drift and vibrations importantly degrade the quality of the images, in particular when live background subtraction is used in order to enhance the magneto-optical contrast.

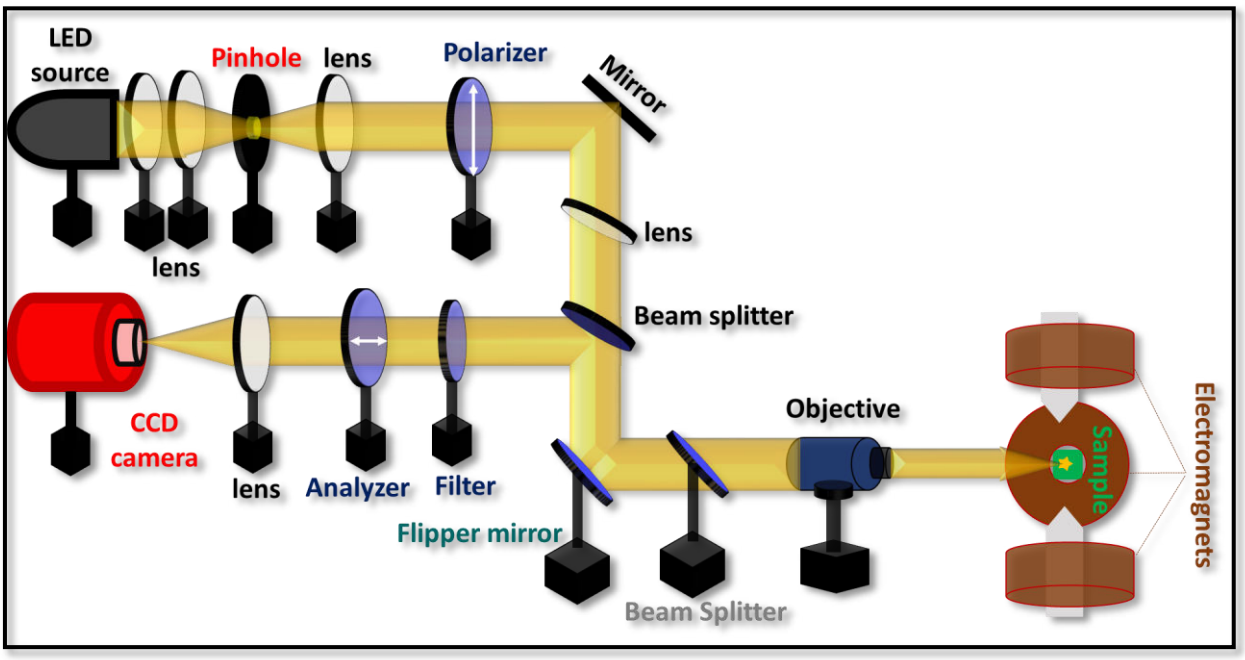

Figure 3.12 Kerr microscopy setup for magnetic domain analysis and single-shot switching measurements

3.3 Dynamic Characterization Techniques

This section comprises various dynamic characterization techniques used to study different magnetic and thermal properties of nanostructures in the picosecond and femtosecond time scales. Sections 3.3.1-3.3.2 is introduction to the concept of pump-probe measurements, and in particular to the time-resolved magneto-optical Kerr effect (TR-MOKE) and the time-domain thermal reflectance (TDTR) methods. Section 3.3.2 is an introduction to the electrical probing technique used to detect the time-resolved electric field traces of the picosecond wide electrical pulses generated. In addition, efforts to further advance the probing techniques and implement the e-field antenna/detector on chip will be discussed. The last part of this section includes some of our efforts to optimize the transmission line parameters to have a better control of wave reflections in the devices.

3.3.1 Time-resolved pump-probe methods

Figure 3.13 represents the schematic of the optical setup used for various time-resolved pump-probe measurements. Such measurements are vitally important in many research areas where time resolution is pushed to extremely short timescales. In this kind of measurement, a very short pulsed source is necessary, often a femtosecond optical pulse. The pulse is then divided into two in-phase pulses, one which will be used as an excitation or “pump”, and a second one which will be used as a detector or “probe”. The pump triggers some dynamics (magnetization change, electronic occupation change…) repeatedly with a certain repetition rate. Since the signal obtained by probing a single event is generally too noisy, the key consists in probing the average response of multiple *identical* events. This entails a full recovery of the sample to its pre-excited state before the next pump event. Finally, by changing the interval of time between the pump and the probe pulses, the time-resolved dynamics can be sampled, limited only by the pulse-duration of the pump and probe pulses.

The pump and probe pulses can be of different nature (THz, optical-IR, deep-UV, current pulse…). During this thesis the pump was either a femtosecond laser pulse or a picosecond electrical current pulse. In most experiments we use an intense pump pulse, in order to create large dynamics, and a relatively small intensity probe pulse, in order to detect the sample property changes without exciting too much the sample.

In order to split the laser into pump and probe beams, we use a polarizing beam splitter in combination with a half waveplate ($\lambda/2$) in order to set the polarization angle and select the

splitting ratio after the beamsplitter. We usually set the probe beam to about 15% of the total power.

The delay line is an essential component for any laser-driven pump-probe measurements since it provides the time delay between the pump and the probe beams by introducing an optical path-length difference between the two beam paths. It is an assembly of a few silvers mirrors and a retro-reflector mirror that is mounted on a mechanical rail. Two main problems may arise when setting up a delay line: First, the input beam into the retroreflector needs to be perfectly parallel to the delay line rail, otherwise resulting in spatial shifts of the beam as the retroreflector position is moved. The second possible challenge is divergence in the beam. If the input beam is slightly divergent (or convergent), then the output beam dimensions might be very different from the input beam dimensions, resulting in a different fluence at the sample position. To limit this, a pair of lenses might be used before the delay line to correct the divergence. If divergence cannot be improved (Gaussian beam always have a certain divergence, due to diffraction) the diameter of the beam might be increased, to limit divergence, particularly if using a long delay line. One of the ways to ensure the good alignment of the setup is to use a camera or beam-profiler after the delay line and to compare the initial and final positions and sizes of the beam. In our experience, we were able to reduce the lateral shift down to less than 50um for a ~2mm beam (~2% change) over 4 meters of delay line, and the divergence's effect to less than 10% in size change over the same range.

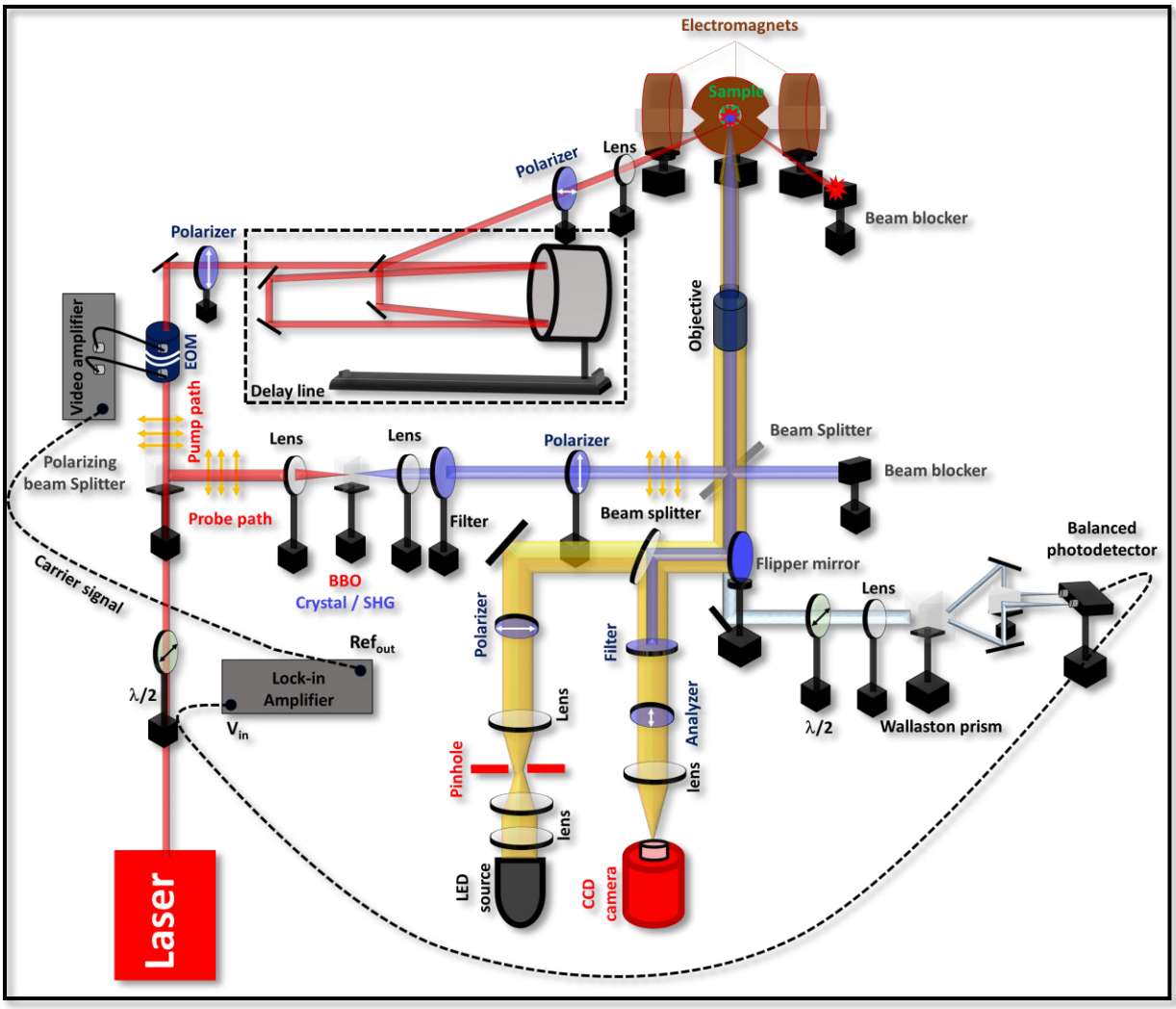

Figure 3.13 Schematic representation of TRMOKE setup for both Kerr microscopy and spectroscopy measurements

As mentioned in section 3.2.4.1, an optical chopper was employed in the probe beam path to modulate the optical signal. For the pump-probe setup, an electro-optic modulator (EOM) was employed in the pump beam path since a EOM can modulate the signals at very high frequencies, where the 1/f electronic noise is strongly reduced. In our experiments, the EOM was used along with a 250 series video amplifier which can deliver 275 V peak to peak signal from DC to 6MHz. The electro-optic modulator consists of a pair of two crystals placed close to each other forming a capacitor with one electrode on each side of the pair. An application of electric field through the electrodes changes the relative refractive index of the crystals and the incident optical beam gets modulated at the applied electric field frequency. For most of the measurements, the optical signal was modulated at a frequency of 3MHz which was provided through the SINE OUT port of the Lock-in amplifier.

Optical filters are used for various purposes such as to block or allow a particular wavelength range of the laser beam or to allow or block a part of the spectrum of the laser beam. In our experimental setup, when both the pump and the probe beams have the same wavelength (i.e. 800nm), optical filters are used in the pump and the detection path respectively. The first filter cuts the initial 50-60 % of the spectrum and the second optical filter placed in the detection path cuts the rest. This pair of optical filters were used to avoid the pump leakage into the probe beam path. For the setup with the BBO crystal in the probe path, a simple low pass filter is sufficient to allow the optical signal up to 400nm and to block the 800nm completely.

A convenient component for balanced detection path is the knife-edge right-angle prism mirror. This element ensures the normal incidence of the two probe beams on the balanced photodetector avoiding any clipping of the beam when hitting the tiny ~1mm photodiodes.

3.3.1.1 Time-resolved magneto-optic Kerr effect (TRMOKE)

Ultrafast time-resolved magneto-optic Kerr effect (TRMOKE) measurements are relatively new characterization tools that came into existence after the invention of pulsed laser sources. One of the first TRMOKE measurements was undertaken in the year 1960s where the magnetic field pulse-induced magnetization precessions were observed in the nanosecond time scales [73]. Later in the year 1996, after the discovery of ultrafast demagnetization of a 20nm thick Ni ferromagnet as a result of irradiation with femtosecond laser pulses [10], TRMOKE experiments became a powerful tool to study the magnetization dynamics with incredible time-resolution. These experiments can be considered as a time-domain counterpart to the more common ferromagnetic resonance (FMR) measurement.

For the detection of the TRMOKE signal, i.e. the pump induced MOKE signal, we bring in the pump beam onto the sample, and ensure an overlap of the pump and probe beams at the sample surface. For the TRMOKE, intensity modulation is achieved at high frequency (MHz) via the electro-optic modulator and a pair of crossed polarizers. The schematic of working principle of a typical EOM is shown in Figure 3.14.

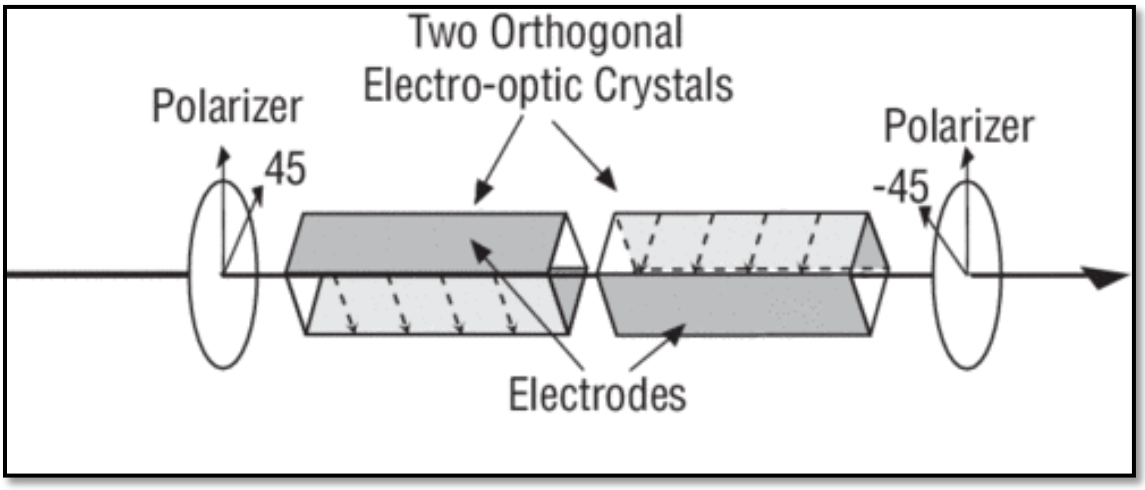

Figure 3.14 Schematic to represent the working principle of electro-optic modulator

The modulation of the pump's electric field is then given by

3.27

$$\mathbf{\mathit{1}} = \begin{bmatrix} 0 & 0 \\ 0 & 1 \end{bmatrix} \underbrace{e^{-\frac{i\delta}{2}} \begin{bmatrix} \cos^2\theta + e^{-i\delta}\sin^2\theta & \left(1-\mathrm{e}^{\mathrm{i}\delta}\right)\cos\theta\sin\theta \\ \left(1-\mathrm{e}^{\mathrm{i}\delta}\right)\cos\theta\sin\theta & \sin^2\theta + e^{-i\delta}\cos^2\theta \end{bmatrix}}_{\text{arbitrary retardation}} \begin{bmatrix} \mathbf{E_0} \\ 0 \end{bmatrix}$$

Where θ is the angle between the fast axis of the EOM crystals and the x axis and δ is the phase difference between the orthogonal x & y field components (known as retardance). In our setup we set $\theta = \pi/4$, which simplifies the expression E_{EOM}. The transmission through the system T_{EOM} is then given by

$$T_{EOM} = \frac{I}{I_0} = \frac{\boldsymbol{E_{EOM}E^*_{EOM}}}{\boldsymbol{E_0\,E^*_0}} = \cdots = \frac{1}{2} + \frac{1}{2}\cos(\delta) \qquad \textit{3.28}$$

The retardance δ is controlled via the change in optical index (birefringence) Δn, and is given by $\delta = \frac{2\pi L}{\lambda_0}\Delta n$ where L is the length of the crystals and λ_0 is the wavelength of light in vacuum. The birefringence is controlled via linear electro-optic effect, also known as the Pockel's effect, by applying a DC and AC bias to the crystals.

3.29

$$\delta = \frac{2\pi L}{\lambda_0}\mathrm{B}[V_{DC} + V_{AC}(\omega_{EOM}t)]$$

Where we define B as a linear electro-optic constant and where ω_{EOM} is the EOM's modulation pulsation. In our setup, we know that at $\lambda_0 = 800$ nm a 250 V DC bias swing rotates the polarization by 90 degrees, which means it induces a retardance of π. This is commonly known as the half wave voltage. We can therefore simplify equation. 3.29 at $\lambda_0 = 800$ nm as,

$$\delta_{800nm} = \frac{\pi}{250}[V_{DC} + V_{AC}(\omega_{EOM}t)] \qquad 3.30$$

We set $V_{DC} = -250 + V_{low,dc}G_{amp}$, where $V_{low,dc}$ is the actual input DC voltage that is then amplified by $G_{amp}\sim100$ via the audio amplifier (converts 0 to 5 V into -250 to +250 V). For $V_{low,dc}\sim1.114$ V we obtain a $V_{DC}\sim138$ V, close to a quarter wave retardation. We set $V_{AC} = 125\sin(\omega_{EOM}t)$ to modulate the total voltage between 0 and 250V, and achieve near-full modulation. The total transmission is therefore given by,

$$T_{EOM} = \frac{1}{2} + \frac{1}{2}\cos\left(\frac{\pi}{250}[-138 + 125\sin(\omega_{EOM}t)]\right) \qquad 3.31$$

Figure 3.15(a) is a plot of the result of equation 3.31 at 1 MHz, and its comparison with the experimentally measured output on a fast photodiode.

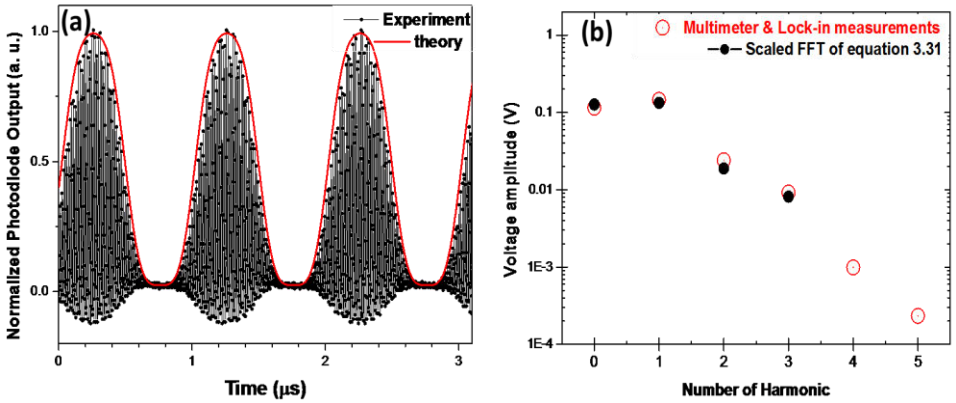

Figure 3.15 (a) Comparison between the theoretical and experimentally obtained transmission function of EOM and (b) FFT of transmission function and it's comparison with the experimental obtained results for different harmonics

The lock-in will demodulate this signal, so to predict the Kerr rotation we need to know the different frequency components of our modulated signal. We perform a FFT (fast Fourier transformation) of equation 3.31, and compare the results with experimental measurements of the DC voltage and of the signal amplitudes (not RMS!) at the various harmonics, performed on the lock-in as shown in figure 3.15(b).

Again, experimental results compare fairly well with our model predictions, particularly for the DC and 1st harmonic terms. For a 0 to 1V photodiode modulation, we find $V_{DC}\sim 0.46$ V and $V_{1f}\sim 0.559$ V, $V_{2f}\sim 0.042$ V, $V_{3f}\sim 0.0682$ V… We can therefore approximate the modulation as,

$$T_{EOM} = 0.46 + 0.5586\, sin(\omega_{EOM} t) + 0.042\, sin(2\omega_{EOM} t) + 0.0682\, sin(3\omega_{EOM} t) \ldots \qquad 3.32$$

Now that we have the modulation of our pump, and its decomposition in Fourier components, we can see how our signal will be modified by the pump. Unlike when measuring hysteresis, where the probe beam is modulated, in TRMOKE measurements, the pump beam is modulated, which then modulates the sample parameters. The modulation is thus applied to the sample's reflection matrix $[S]$ in equation 3.8, meaning all the Fresnel coefficients are time dependent now. If we carry the modulation until equations 3.18 and 3.19, we obtain,

$$V_+ = V_- = \frac{\mathrm{P}_0\, T_0\, R_M g}{2} |\, r_{pp,0} + \Delta r_{pp}(\mathrm{t})|^2 \qquad 3.33$$

$$V_{RF} = 2P_0\, T_0\, R_{\mathrm{M}} G \big|\, r_{pp,0} + \Delta r_{pp}(\mathrm{t})\big|^2 [\theta_{\mathrm{k},0} + \Delta\theta_k(t)] \qquad 3.34$$

We can see that the RF voltage is sensitive to the static Kerr rotation $\theta_{\mathrm{k},0}$, the pump induced Kerr rotation changes $\Delta\theta_k(t)$ as well as to the static and dynamic reflectivities $r_{pp,0}$ and $\Delta r_{pp}(\mathrm{t})$, respectively. We measure the monitor voltages with a multimeter, at any time delay, and assume the reflectance changes induced by the pump $\Delta r_{pp}(\mathrm{t})$ are small in comparison to the static reflectivity $r_{pp,0}$. We develop the RF voltage equation and neglect the smallest terms,

$$V_{RF} = 2P_0\, T_0\, R_{\mathrm{M}} G\big[\, r_{pp,0} + \Delta r_{pp}(\mathrm{t})\big]\big[r^*_{pp,0} + \Delta r^*_{pp}(\mathrm{t})\big][\theta_{\mathrm{k},0} + \Delta\theta_k(t)] \qquad 3.35$$

$$= 2P_0\, T_0\, R_{\mathrm{M}} G\big[\, r_{pp,0} r^*_{pp,0}\theta_{\mathrm{k},0} + r_{pp,0}\Delta r^*_{pp}(\mathrm{t})\theta_{\mathrm{k},0} + \Delta r_{pp}(\mathrm{t}) r^*_{pp,0}\theta_{\mathrm{k},0} + r_{pp,0} r^*_{pp,0}\Delta\theta_k(t)\big] \qquad 3.36$$

$$= 2P_0\, T_0\, R_{\mathrm{M}} G \quad [\underbrace{\big|r_{pp,0}\big|^2\, \theta_{\mathrm{k},0}}_{\text{static Kerr rotation}} + \underbrace{(\, r_{pp,0}\Delta r^*_{pp}(\mathrm{t}) + \Delta r_{pp}(\mathrm{t}) r^*_{pp,0})\theta_{\mathrm{k},0}}_{\text{change in reflectivity}} + \underbrace{\big|r_{pp,0}\big|^2 \Delta\theta_k(t)}_{\text{change in Kerr rotation}}\,] \qquad 3.37$$

To measure the RF voltage, we use the lock-in, which measures only the 1st harmonic, and outputs the RMS voltage. Eliminating the static terms, and including the prefactor of the 1st harmonic we obtain the in-phase signal,

$$V_{IP} = \frac{1}{\sqrt{2}} 2P_0\, T_0\, R_{\mathrm{M}} G[\theta_{\mathrm{k},0} \mathrm{f}(\Delta r_{pp}^{pk-pk}) + \left|r_{pp,0}\right|^2 \Delta\theta_k^{pk-pk} 0.5586] \qquad 3.38$$

Where $\Delta\theta_k^{pk-pk}$ and $\mathrm{f}\left(\Delta r_{pp}^{pk-pk}\right)$ are peak to peak changes of the Kerr rotation and a function of the dynamic reflectivity. Interestingly, we can assume that our static Kerr rotation $\theta_{\mathrm{k},0}$ is decomposed into a magneto-optic Kerr rotation $\theta_{\mathrm{k(mag),0}}$ + a small parasitic rotation $\theta_{\mathrm{k(parasitic),0}}$ which unbalances our photodiodes (technically this term should be better derived from equation 3.9 by including a small error in the fast axis angle of the wave-plate). This is the reason why, it is often safer to measure the time-dependent signals with a positive and a negative magnetic saturation and then subtract them, in order to eliminate the term which is highly sensitive to the balance. The term proportional to the magneto-optic Kerr rotation is much smaller, since $\theta_{\mathrm{k(mag),0}}$ are typically very small. By dividing equation 3.38 by equation 3.33 we obtain the relation,

$$\frac{V_{IP}}{V_+} = 2 \cdot 0.5586\sqrt{2}\frac{G}{g}[\theta_{\mathrm{k},0} \mathrm{f}'(\Delta r_{pp}^{pk-pk}) + \Delta\theta_k^{pk-pk}] \qquad 3.39$$

For a well-balanced signal, with relatively small dynamic reflectivity, we would have,

$$\frac{V_{IP}}{V_+} \sim \sqrt{2}\frac{G}{g}\Delta\theta_k^{pk-pk} \qquad 3.40$$

If the experiment allows measurements with both magnetic polarities, we can precisely extract the pump-induced Kerr rotation $\Delta\theta_k^{pk-pk}$ by taking the difference of two traces with opposite magnetic polarity, even for unbalanced signals.

Figure 3.16 (a) represents the TRMOKE measurement on one of the samples (stack detail: $Pt_5/Ta_4/Co_3/Cu_1/Ta_4/Pt_1$ where a number in subscript represents the thickness in nanometers) used during this thesis work. The above TRMOKE response corresponds to a 3nm thin Co layer with in-plane magnetic anisotropy. Moreover, the device is patterned, and has some preferential direction within the plane. We use a polar MOKE configuration, sensitive to the out-of-plane magnetization change.

Zero time delay is the moment in space and time when both the optical beams overlap and have no optical path-length difference. In other words, it can be seen as the time when the pump just starts to interact with the material. The black curve represents the magnetic response of the sample in the presence of a positive external out-of-plane magnetic field whereas the blue corresponds to a negative external out-of-plane field. Before these measurements, the ferromagnet was saturated in one of the in-plane directions by applying an external IP magnetic

field. The external OOP field is required to detect these magnetic oscillations since it slightly changes the plane of precession and thereafter, the dynamics can be studied by exciting the system optically or electrically. The measurements shown in figure 3.16(a) are for electrical excitation.

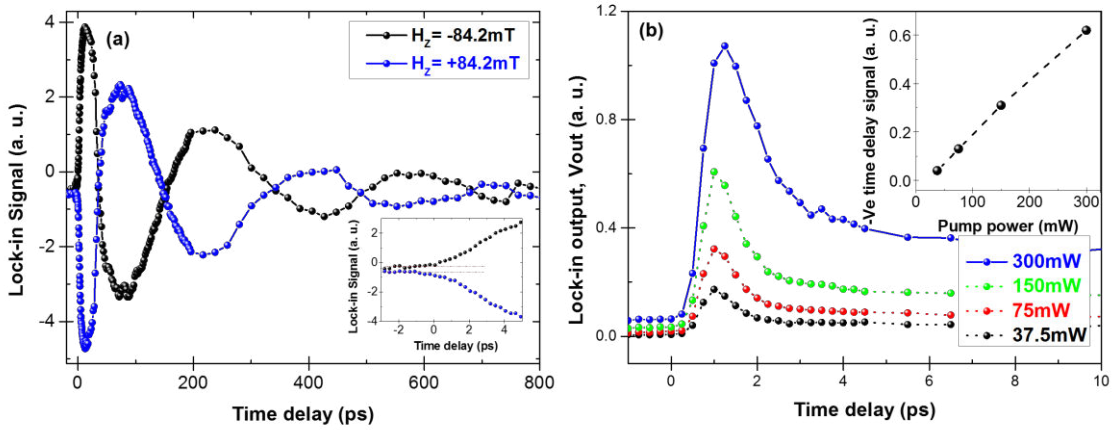

Figure 3.16 (a) TRMOKE dynamics of a $Pt_5/Ta_4/Co_3/Cu_1/Ta_4/Pt_1$ sample after excitation with THz pulse, and (b) pump power dependence on the TRMOKE signal for a $Pt_4/Co_1/Pt_4$ sample after optical excitation under an out-of-plane magnetic field (H_Z)

The pump-probe signal is detected by taking the difference of signal levels with and without the pump excitation. The signal level before time zero (i.e. negative time zero) should be zero, since the signal before the pulse should be equal to the signal when there is no pulse, but as shown in figure 3.16(b), there is often a small non-zero signal. We attribute this non-zero signal level before time zero to heating present in the system that could not be dissipated before the next laser excitation (~12.5ns for a 80MHz repetition rate). This effect can be verified by taking similar measurements at different pump power values as represented by figure 3.16 (b). The plot in the inset section shows a linear dependence of the negative time delay signal on the pump power. The measurements shown in figure 3.16 (b) are the result of optical excitation on a slightly different magnetic nanostructure (stack detail: $Pt_4/Co_1/Pt_4$) where the Co ferromagnet possesses perpendicular magnetic anisotropy.

3.3.1.2 Time-domain thermo-reflectance (TDTR)

The time-domain thermal reflectance (TDTR) setup is used to detect the time-resolved temperature-induced change in the reflectance. This kind of measurement can access various thermal properties of the samples such as electronic or phonon thermal conductivity, electron-phonon coupling or other parameters. During this thesis work, TDTR measurement was used for different purposes such as to find the time zero. Finding the time zero can be a little tricky at the

beginning of developing the setup and therefore it is convenient to take TDTR measurement on a sample that has high thermo-reflectance signal, for example, LT-GaAs substrates.

Since the TDTR is a measurement of the change in the reflection only, we don't need any analyzer in the detection path. In our setup, we either need to remove the Wollaston polarizer from the detection path so that the reflected laser beam can go directly into one of the photodiodes or we have to rotate the half-wave plate ($\lambda/2$) before the Wollaston prism such that the full intensity of the laser is directed towards a single photodiode. Figure 3.17(a) represents the TDTR traces for the above-mentioned conditions.

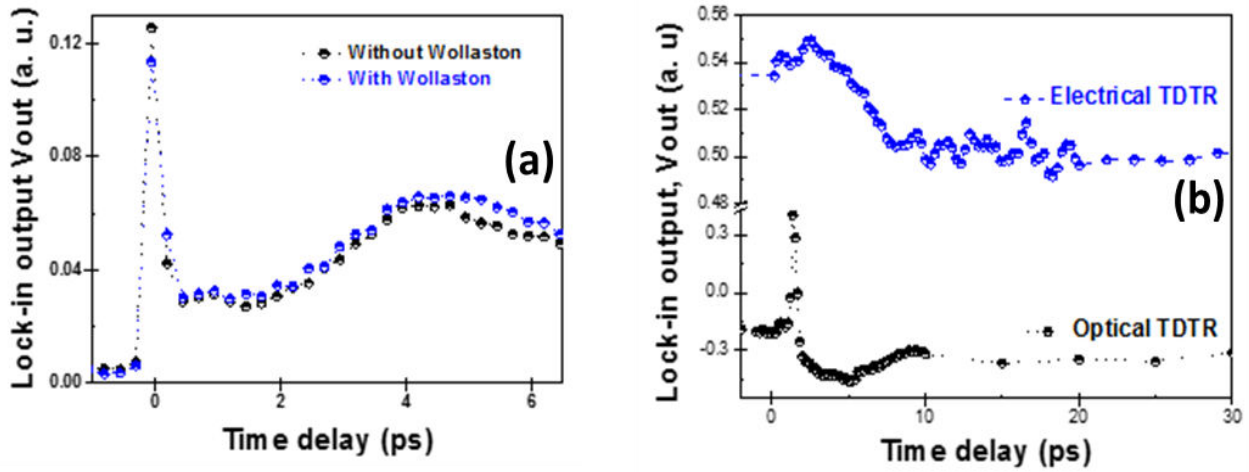

Figure 3.17 (a) Different approaches of detecting the TDTR signal, (b) TDTR signal after optical (fs laser pulse) and electrical (ps electrical pulse) excitation of a magnetic nanostructure

Figure 3.17(b) represents the TDTR traces for both the optical (i.e. fs laser pulse) and the electrical (i.e. ps electrical pulse) excitations on a multilayer stack of Ta(5)/Pt(4)/Co(3)/Cu(1)/Ta(4)/Pt(1). The time zero value for both the cases has a difference of ~ 9ps since in the case of electrical excitation, the pump (ps Electrical pulse) has to travel ~1075 μm extra through the gold (Au) transmission line. Considering the speed of the light along the gold transmission line, this distance of ~1075 μm corresponds roughly to 8.9ps. To detect the TDTR signal after electrical excitation, a few additional steps need to be done. These steps include biasing of the photoconductive Auston switch with the source meter and to short the end of the transmission line with an impendence matched resistor. These electrical connections can be done either via wire bonding or by using impedance-matched RF tips (picoprobe). The use of wire bonds can lead to reflection from the end due to impedance mismatching. Most of the results reported in this thesis are obtained with impedance-matched RF tips (picoprobe). An attempt to tackle the issue of impedance mismatching within the on-chip THz device is made and listed in section 3.3.2.

3.3.1.3 Time-resolved THz e-field measurement

There are several different approaches to detect the time-resolved electric-field component of a THz pulse including electro-optic sampling, photoconductive sampling, etc [74] [75] [76]. Electro-optic sampling is widely used as it provides a high sensitivity as well as a bandwidth of >30THz [60]. Only a few additional elements are required to transform a TRMOKE setup into a THz time-domain spectroscopy setup, most importantly, the non-linear crystal (ZnTe, ZnSe…) that performs the electro-optic operation. However, when dealing with on-chip photoswitch-based THz pulses that have a limited bandwidth (typically <4THz), it is simplest to use a second photoconductive switch to perform the sampling. The second photoswitch remains unbiased during the readout operation, and it is the electric field of the travelling THz pulse that acts as a transient bias. When the probe beam is irradiated on the second photoconductive switch or the photoconductive antenna, carriers are excited, and are then accelerated by the electric field of the THz pulse. This in turn induces a measureable DC current proportional to the THz current. By changing the delay between the pump and the probe the electric field (i.e. current) as a function of time can be sampled. Since the output DC currents are small (in the pico- and nanoAmps range), modulation and lock-in amplification should be used.

In our case, we used a commercial photoconductive switch grown on a thin cantilever as shown in figure 3.18 (d). This device, sold by the name Teraspike®, has a bandwidth of 4THz and allows for measurements at various positions on the transmission line. While seting upthe Teraspike® microprobe, we provide a small bias of 1V to the tip via a sourcemeter, and adjust the probe laser beam position on the photoconductive switch (with <3mW for the 80MHz laser) until the photocurrent is maximized.

Figure 3.18 (a) represents the E-field trace on one of the transmission line structures. This measurement has been taken at the red dot position on the transmission line as shown in figure 3.18(b). The very first peak is the main electrical pulse and all the other small peaks are the reflections from different spatial positions on the transmission line due to impedance mismatching. The speed of the electromagnetic wave in the transmission line is $1/3^{rd}$ of the speed of light in the vacuum that is 1.2×10^{8} m/s. Hence, the 2^{nd} peak is the reflection from the load and the 3^{rd} peak is the reflection from the end. The fourth peak is most likely the reflection from the photoconductive switch since the time difference between the 3^{rd} and the 4^{th} peak is ~18ps which corresponds to a spatial distance of ~2000μm. Figure 3.18(c) represents the THz E-field traces at different positions on the transmission line. The difference in the time zero value for different positions is used to calculate the speed of propagation of the ps electrical signal. We can see that the amplitude of the pulse is also decreased as the pulse advances. However,

as we move the tip for these experiments, the distance between the tip and the transmission line is also slightly changed, which in turn changes the detection sensitivity. This complicates any absorption characterization effort.

3.3.2 High-frequency characterization

A vector network analyzer was used to characterize our transmission lines in the MHz to GHz frequency range. To this aim, a vector network analyzer measures the s-parameters corresponding to the reflection and the transmission of AC electrical power. Fitting an analytical model allows the extraction of parameters such as capacitance, inductance or impedance describing the high-frequency response of the system. Impedances of various lines where characterized in order to find the best match with our 50 Ohm electrical probes. This step will be particularly important for future modifications and calibrations of the transmission lines.

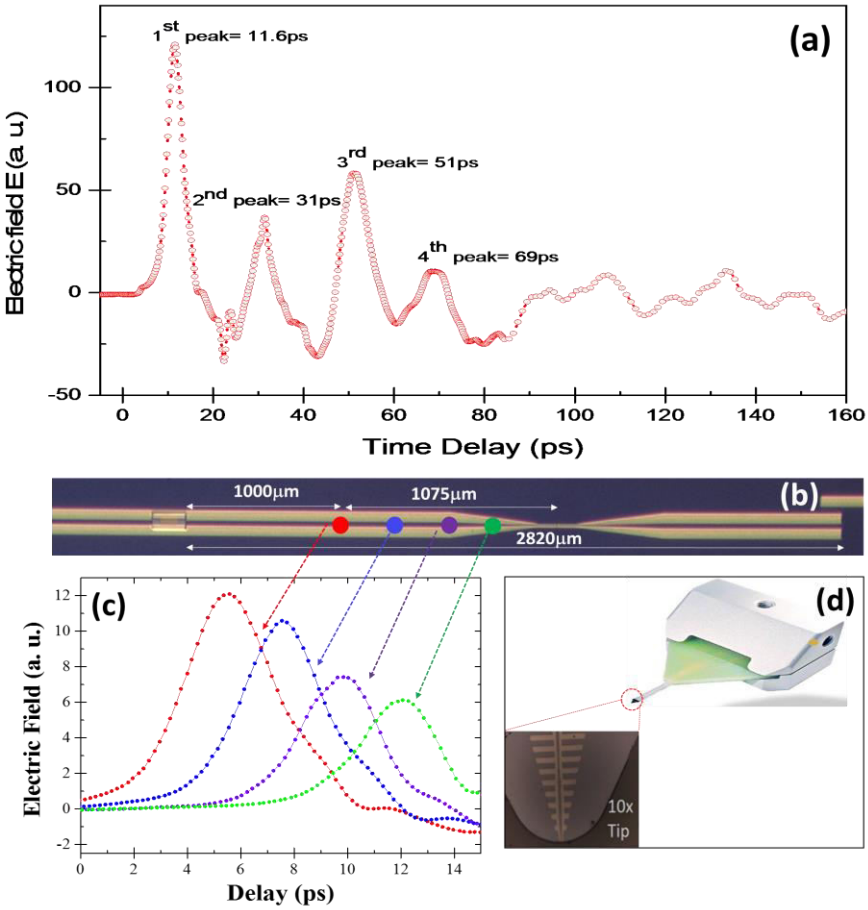

Figure 3.18 (a) Time-resolved E-field measurement (b) THz on-chip device under the microscope with labels for the positions where the E-field traces have been taken as shown in (c), (d) Teraspike probe/antenna to detect the E-field component

Co-planar waveguide (CPW) and co-planar stripline (CPS) are the two transmission line structures that are being used for this thesis work. Optimizing all the geometrical parameters of the transmission line is very important to get rid of the unwanted reflected signals that can be arising due to impedance mismatching. In this section, some of the preliminary attempts are reported that were made to optimize the co-planar waveguide (CPW) structure to obtain a $50\ \mathrm{Ohms}$ impedance on the new substrates we received from our grower.

For this study, five different CPW devices were fabricated on a LT-GaAs substrate where all the geometrical parameters i.e. length of transmission line ($L = 2\mathrm{mm}$), width of the central conductor ($W = 75\mu\mathrm{m}$), thickness of the gold line ($T = 0.3\mu\mathrm{m}$), height of the dielectric substrate ($H = 500\mu\mathrm{m}$) were kept constant while changing the gap between the conductors ($\mathrm{Gap(G)} = 15 - 40\mu\mathrm{m}$). These parameters were decided after using an online available transmission line modeling software (i.e. TXLINE 2003). Figure 3.19 represents the soft mask that was used to fabricate the required devices using maskless UV-lithography. The devices for this study were fabricated using the maskless/projectorial UV- lithography tool where the desired patterns were first drawn with *Klayout* software and the soft copy of the mask was used to fabricate the desired patterns.

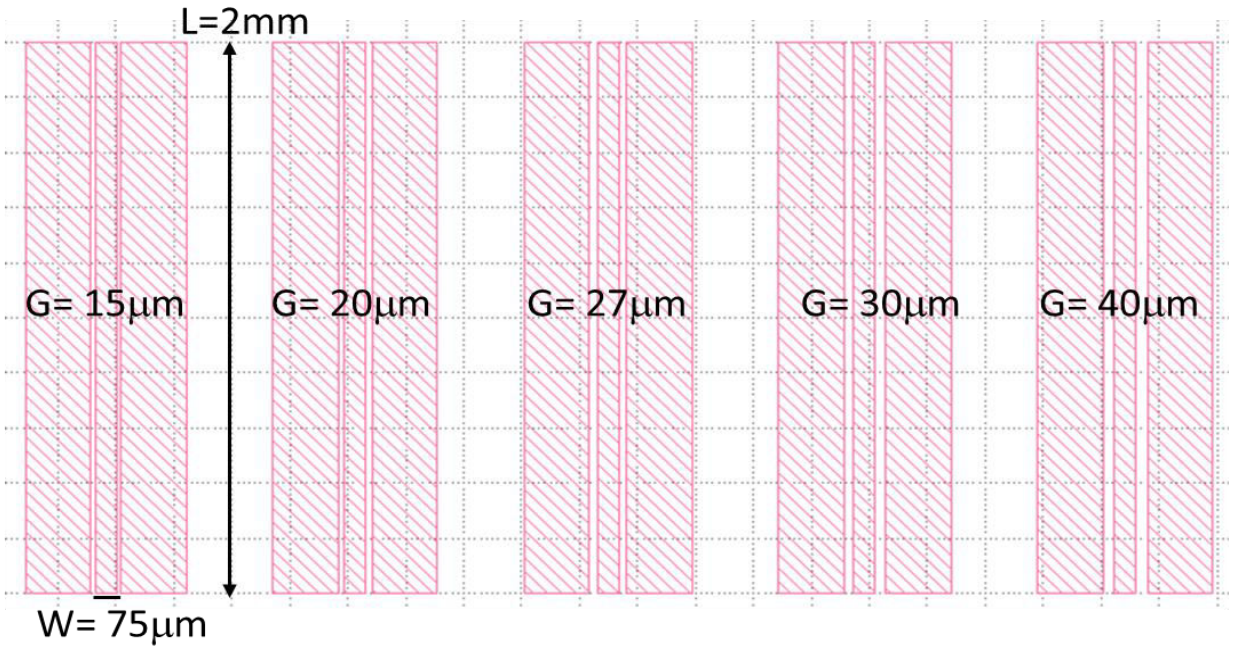

Figure 3.19 Picture of the soft mask to fabricate the CPW devices with different gap values using maskless Lithography

The vector network analyzer we have used has 2 ports and can cover the range 1MHz-40GHz. One port is connected to the left side (input) of the circuit and the second port to the right side (output). First, the input is set as the source of the signal, and delivers an AC signal at a given

frequeny. During this time both ports are used to detect the reflected and transmitted signals simultaneously. Then, the output is set as the source, and a second measurement of both transmitted and reflected signals is done. The output can be described by the following 2×2 s-parameter matrix as shown below-

$$s = \begin{bmatrix} s_{11} & s_{12} \\ s_{21} & s_{22} \end{bmatrix} \qquad 3.41$$

Where s_{11} is the signal detected at port 1 while port 1 was the source. Both the real and the imaginary parts of each element were recorded.

To compare the experimentally obtained data with that of the theoretical model predictions, we have worked with a Python code that was developed following the textbooks written by Gupta *et. al.*, and DM Pozar [77] [78]. The model first calculates the theoretical values of the characteristic parameters such as the characteristic impedance (z_0), phase velocity (V_P) according to the geometrical dimensions of the system. Consequently, we use these as initial parameters for our fitting procedure. The model multiplies a concatenation of transmission matrices of each section on the transmission line. The final transmission matrix can then be translated into an s-matrix to be compared with the experimental data. This procedure allows to get a more accurate value of the impedance. The procedure is still being implemented and improved, but we can already extract the impedance, the dielectric constant of our substrates, the phase velocity… (see table 1)

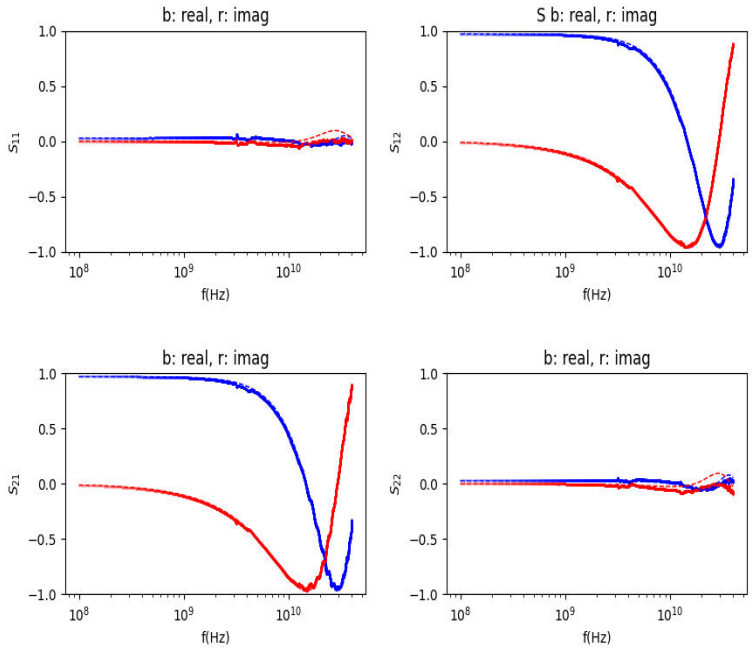

Figure 3.20 Fitting of s-parameters for devices with 40µm of gap between the conductors (G)

Table 1 Experimentally obtained parameters of for co-planar waveguide structure for different gap values.

Gap G (μm)	z_0 (Ohms)	Phase velocity (10^8 m/s)	Relative dielectric permittivity of substrate
15	35.25	1.21	13
20	38.47	1.21	13
27	42.25	1.21	13
30	44.19	1.21	13
40	48.44	1.21	13

After calculating the value of characteristic impedance z_0 for all the devices, it was found that the device with $\mathrm{G} = 40\mu\mathrm{m}$ is the closest to the desired value i.e. 48.44 Ohms. The fits for $G = 40\mu\mathrm{m}$ are shown in Figure 3.20. Further measurements are required to characterize the other parts of the transmission line such as the tappers, the photoswitch or the magnetic sample. Such study will allow us to predict the reflections and amplitude of waves at all points, among other things, which we can then use to optimize the transmission lines.

3.4 Numerical simulation of the macroscopin LLG model

This chapter describes the macrospin model used to simulate the experimental data measured on various magnetic structures interacting with the femtosecond laser and picosecond electrical pulses. Section *3.4.1* re-introduces the Landau-Lifshitz-Gilbert (LLG) model including the field and the damping-like spin-orbit torque terms. Further in sections 3.4.2 and 3.4.3, the effects of temperature have been introduced.

3.4.1 Landau-Lifshitz-Gilbert (LLG) equation

To model the effect of spin-orbit torques on the magnetization in the picosecond time regime, the Landau-Lifshitz- Gilbert equation of motion with anti-damping like and field-like terms from the spin-current in the following form was solved using matlab coding:

$$\frac{d\boldsymbol{m}}{dt} = -\gamma\mu_0(\boldsymbol{m}\times\boldsymbol{H_{eff}}) + \alpha\left(\boldsymbol{m}\times\frac{d\boldsymbol{m}}{dt}\right) - \theta_{SH}^{DL}\,C_s(\boldsymbol{m}\times(\boldsymbol{m}\times\boldsymbol{\sigma})) - \theta_{SH}^{FL}C_s(\boldsymbol{m}\times\boldsymbol{\sigma}) \qquad 3.42$$

where

$$C_s = \frac{\mu_B}{q_e}\frac{\boldsymbol{J_c}}{d_0}\frac{1}{\boldsymbol{M_s}} \qquad 3.43$$

Here, γ is the gyromagnetic ratio, μ_0 is the vacuum permeability, α is the damping parameter, $\boldsymbol{M_S}$ is the saturation magnetization, σ is the direction of spin-polarization, θ_{SH}^{DL} is the damping-

like spin Hall angle, θ_{SH}^{FL} is the field-like spin Hall angle, $\boldsymbol{J_c}$ is the charge current density, d_0 is the thickness of the magnetic layer, q_e is the charge of the electron and μ_B is the Bohr magneton. The effective field in the first term consists of a magneto-crystalline anisotropy field, a demagnetization field, and any applied external field,

$$\boldsymbol{H_{eff}} = \begin{bmatrix} \boldsymbol{H_x} - N_x M_s \boldsymbol{m_x} \\ \boldsymbol{H_y} - N_y M_s \boldsymbol{m_y} \\ \boldsymbol{H_z} + \left(\frac{2K}{\mu_0 M_s} - N_z M_s\right) \boldsymbol{m_z} \end{bmatrix} \qquad 3.44$$

Here, H_x, H_y and H_z are the x, y, and z-components of the external field, K is the perpendicular anisotropy constant, and $\boldsymbol{M} = M_s\begin{bmatrix}\boldsymbol{m_x} & \boldsymbol{m_y} & \boldsymbol{m_z}\end{bmatrix}^T$. $N = \begin{bmatrix}N_x & N_y & N_z\end{bmatrix}^T$ is the demagnetizing factor, and determines the shape anisotropy. For example, for a thin film, *N* = [0 0 1]. For this thesis work, the macrospin approximation is used, i.e. we assume that the properties in equation 3.42 are independent of position. To solve for the dynamics, we first set $d\boldsymbol{m}/dt = 0$ and solve for the equilibrium orientation of the moment, $\boldsymbol{m}(t < 0) = \boldsymbol{m_0}$. We identify the stable solution to $d\boldsymbol{m}/dt = 0$ by choosing the solution with the lowest free energy. We then use a finite-difference scheme to evolve $\boldsymbol{m}(t)$ forwards in time in response to a charge current $\boldsymbol{J_c}(t)$. We evolve the magnetization forward in time with time-increments of $\Delta t = 1$ fs (we verified that the results were unchanged with smaller time-increments).

3.4.2 Heat-diffusion equation

Ultrafast heating of a magnetic material leads to temperature-induced changes to the magnetic moment and the interfacial anisotropy. We estimate the temperature response of the metal film in our experiments by solving the heat diffusion equation,

$$C\frac{dT}{dt} = \Lambda\frac{d^2T}{dx^2} + q(t) \qquad 3.45$$

Here, T is the temperature, C is the heat capacity per unit volume, Λ is the thermal conductivity, and $q(t)$ is the volumetric heating from either a laser or electrical pulse, x is the direction along the long axis of metal film. Based on literature values of the heat capacity of metals [79] and the thickness of each layer, the average value of C for the multilayer stack at room temperature was estimated. The value of Λ was kept fixed according to the Wiedemann-Franz Law $\Lambda = \frac{\mathrm{L}_0 T}{\rho_e}$. Here ρ_e is the measured electrical resistivity (procedure is explained in chapter 5) of the thin film multilayer magnetic stack. For a typical stack used in this thesis i.e.

Ta(5nm)/Pt(4)/Co(1)/Cu(1)/Ta(4)/Pt(1), is found to be $\sim 81\ \mu\Omega \cdot \mathrm{cm}$ the value for Λ turns out to be ~ 9 $Wm^{-1}K^{-1}$.

To fit the optical excitation data, we assume $q(t) = P_{abs}(t)/(\pi w_0^2 d)$, where $P_{abs}(t)$ is the absorbed laser power vs. time, w_0 is the $1/e^2$ radius, and d is the thickness of the multilayer stack. For electrical experiments, we set $q(t) = \rho_e \boldsymbol{J}^2(t)$, where $\boldsymbol{J}(t)$ is the charge current density. Solving equation 3.45 for $T(t)$ requires boundary conditions. We assume an adiabatic boundary condition at the metal film surface. We assume the heat-current J_Q at the bottom of the metal film is limited by the interfacial thermal conductance G_{int} between the Ta and SiO_2 substrate.

$$J_Q = G_{int} T(z = d) \qquad 3.46$$

Typical values for the conductance between metal films and oxide substrates are 100-300 $MWm^{-2}K^{-1}$ [2-4]. We treat G_{int} as a fit parameter and deduce $G_{int} \sim 170$ $MWm^{-2}K^{-1}$ for the typical sample mentioned above.

By using equation 3.45 to model the temperature response of the stack to heating, we are assuming that electrons, phonons, and spins are in thermal equilibrium with one another. Such an assumption is not always valid on picosecond time scales, and non-equilibrium between thermal reservoirs can drive ultrafast magnetic phenomena [10]. In our experiments, non-equilibrium effects should be small due to the 4-6 picosecond pulse duration of the electrical signals, together with the strong thermal coupling between electrons and phonons in the Co layer [80]. The picosecond time-scale for heating is much greater than the electron-phonon relaxation time in transition metals [81]. Therefore, we can estimate the non-equilibrium between electrons and phonons by assuming a quasi-steady-state condition where the rate of heat absorption of electrons equals the rate of heat loss to the phonons. In other words, we assume $q(t) \sim g_{ep} \Delta T_{ep}(t)$, where g_{ep} is the electron-phonon volumetric energy transfer coefficient [57], which we take from [80].

3.4.3 Temperature dependence of material parameters

To theoretically quantify the effects of the temperature-evolution after optical heating we added temperature effects to equation 3.42-3.44. We allow M_s and K in equations 3.47 and 3.48 to evolve in time based on the predictions of our thermal model described in Equations 3.45 to 3.46. We follow [82] and assume the temperature dependencies of the magnetization and magneto-crystalline anisotropy to be described by the following equations,

$$M_s(T) = M_s(0)[1 - (T/T_c)^{1.7}\ ] \qquad 3.47$$

$$K\ \ (T) = K\ \ (0)[M_s(T)/M_s(0)\ ]^3 \qquad 3.48$$

Here, T_c is the Curie temperature, $M_s(0)$ is the magnetization at absolute zero, and $K\ \ (0)$ is the anisotropy constant at absolute zero.

The ingredients presented in this sub-chapter will be used to fit our experimental results. Details on the fitting methodology and parameter selection will be presented in future sections.

4

Results and Discussion

This chapter is divided into three different subchapters. *Chapter 4.1* explores the spin-orbit torque-induced magnetization dynamics in different magnetic nanostructures at picosecond time scales. The experimental data is compared with the macrospin model described in section 3.4. *Chapter 4.2* reports on the magnetization switching of a 1nm thick ferromagnetic Cobalt layer via spin-orbit torques generated by a single 6ps wide electrical pulse. Chapter 4.3 discusses the importance of impedance matching the transmission lines and the possibilities that impedance engineering might allow. *Chapter 4.4* includes various attempts that are being made to study the Giant- magnetoresistance (GMR) effect at picosecond time scales which could lead to both a time-resolved ultrafast electrical probe and a faster readout.

*****

4.1 Motivation

To challenge existing electronic charge-based memories and processors and integrate low-power spintronics into current computing platforms, the writing operation must first be speed up. For comparison, the record switching time of spintronic devices is still in the order of a few hundreds of picoseconds (even a few nanoseconds for commercial devices) while silicon-field effect transistors have a switching delay of less than 5ps [8].

This could be obtained by replacing the application of a conventional magnetic field with either spin-polarized current pulses [8384] One way of increasing the speed of magnetization manipulation is via the use of femtosecond (fs) laser pulses[51]. However, it is still far more preferable to use electrical currents than optical pulses for various reasons: 1) The integration of optics with electronics is still a big challenge 2) Embedding a femtosecond laser onto a chip is also a major challenge 3) The number of material systems where ultrafast optical control of magnetization has been observed is severely limited.

As mentioned in chapter 2, the time required for magnetization reversal is dependent on a number of parameters such as the switching scheme (field driven, STT or SOT) and switching mechanism (coherent, incoherent). In the case of coherent magnetization switching, the time required for the reversal is limited to half of it'snatural precessional period (i.e. it's ferromagnetic resonance). The precessional frequency ($f = \gamma \boldsymbol{H_{eff}}$; where γ being the gyromagnetic ratio and $\boldsymbol{H_{eff}}$ is the effective magnetic field acting on the magnet) corresponds to a quarter of the time ($T/4$) required for full reversal or the time required to cross the equator. So for the magnetic materials with high magnetic anisotropy (~1T-5T) as used for commercial purposes, ($T/4$) corresponds to (~9ps-2ps) which suggest that at least for the coherent switching scheme, the magnetization can be reversed at these ultrashort time scales.

As described in chapter 2, spin-orbit torque switching can be potentially faster than spin-transfer torque switching due to the immediate torque provided by the injected spin polarization. So far, spin-orbit torques have been studied with electrical pulses as short as ~200 picoseconds. The limiting factor is the availability of pulse generators. In fact, to the best of our knowledge there is no pulse generator available commercially which can generate intense electrical pulses down to a few 10's of picoseconds.

During this thesis work a systematic study of spin-orbit torques generated with sub-10 picosecond wide electrical pulses has been undertaken. We have used the photoconductive switches presented in chapter 3 to generate such pulses and the time-resolved magneto-optical

Kerr effect (TRMOKE) to probe the resulting magnetization dynamics. We have also used such photoswitches to fully reverse the magnetization of a thin perpendicularly magnetized Co film with picosecond electrical pulses. Finally, ongoing work will explore the possibility of using magnetoresistance effects at the picosecond timescale in order to bypass the laser and its limitations.

4.2 Magnetization Dynamics induced by picosecond spin-orbit torques

4.2.1 Sample of choice and fabrication

We selected a number of heterostructures hosting a Co thin film and heavy metals, listed in Table 4.1. To avoid confusion, short names of the samples will be used throughout the manuscript. Pt/Co bilayers were chosen due to their tunable anisotropy: out-of-plane for thickness less than 2nm, and in-plane above. In particular, we always use a Ta(4-5nm) buffer layer to ensure a well-defined (111) texture for the growth of upper layers like Pt or Co. This texture guarantee an interface anisotropy with the neighboring Pt layer that promotes perpendicular magnetic anisotropy. Pt and Ta are also used as heavy metals since they are known to have high spin-Hall angles and hence strong spin-orbit torques. The thin Co layer has been sandwiched between the Pt and Ta heavy metals to enhance the overall SOT acting on the Co spins, since the spin-Hall angles of these heavy metals are opposite to one another. Also, Pt is used to cap the stack in order to prevent oxidation.

Table 2 Details of the magnetic stacks used for the spin-orbit torque studies

Magnetic anisotropy	Details of the magnetic stack (short name)
Out-of-plane	Ta(5)/Pt(4)/Co(1)/Cu(1)/Ta(4)/Pt(1)
In-plane	Ta(4)/Co(3)/Pt(3)
	Ta(4)/Co(2)/Pt(3)

In some samples, a 1nm thin copper (Cu) layer has also been introduced. For example: in Pt/Co(1)/Ta stacks, because the magneto-optic Kerr effect (MOKE) hysteresis resulted in a non-square loop with very small remanence indicating a possible large effective Dylazhosinkii-Moriya interaction as shown in Figure 4.1 (a)[85]. Inserting the Cu layer was essential for the studies that are being undertaken in chapter 4.2, where the full magnetization reversal of a 1nm thin Co layer is shown. Figure 4.1(b) is the sample image under the Kerr microscope at zero external magnetic field ($H_Z = 0$). The small bubble structures are observed which can be due to the

skyrmionic phase that is possible to obtain in the above magnetic stack. Confirming the presence of the skyrmionic phase due to Dylazhosinkii-Moriya interaction is out of the scope for this thesis and hence we proceed further by inserting the Cu (1nm) interlayer. Figure 4.1(c) represents the MOKE hysteresis loop for the magnetic stack after introducing the 1nm thin Cu interlayer between the Co and the Ta which greatly reduces the Dylazhosinkii-Moriya interaction effect and results into almost perfect square hysteresis loop. The x-axis shown in figures 4.1 (a) and (c) presents the magnetic field along the out-of-plane direction with respect to the sample plane (i.e. along z-direction).

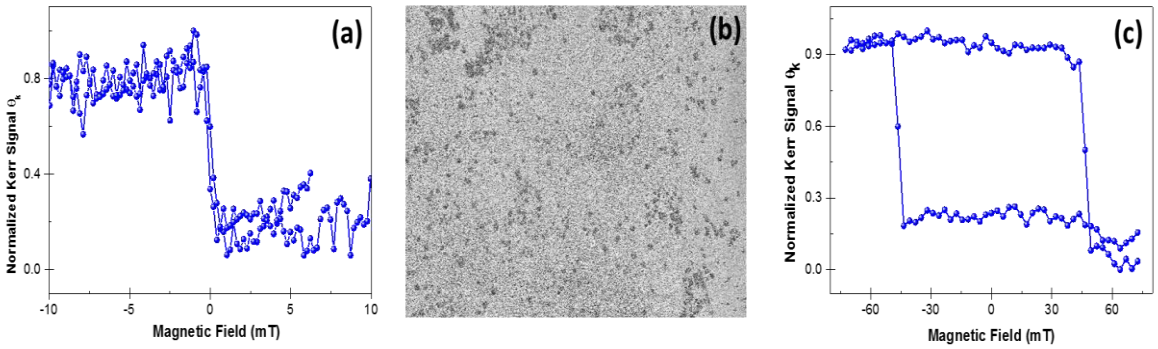

Figure 4.1 (a-b) MOKE hysteresis loop and Kerr microscope image for Pt(5)/Ta(4)/Co(1)/Ta(4)/Pt(1) stack, (c) MOKE hysteresis loop for Pt(5)/Ta(4)/Co(1)/Cu(1)/Ta(4)/Pt(1)stack.

The Co(2) and Co(3) stacks where grown initially for initial tests. These test samples will be used to develop the characterization and simulation tools and to improve our understanding of in-plane and out-of-plane systems excited by picosecond SOTs. The goal is to explain the dynamics in both the in-plane and out-of-plane systems with a single model and single set of parameters. Future work will focus on complete series where the thickness of a single layer is varied or the heavy metal is systematically changed.

4.2.2 Quasi-static spin orbit torques

The Hall bar devices as shown in figure 4.2 (a) were used to perform the quasi-static spin orbit torque switching experiments. First, we characterized the anomalous Hall resistance of the device by performing a magnetic hysteresis loop with the out-of-plane magnetic field (figure 4.2(b)). Then, we applied 100 µs-long current pulses of variable amplitude under a uniform and constant in-plane magnetic field (H_x) and monitored the anomalous Hall resistance a few 10s of milliseconds after each pulse. As shown in figure 4.2(c) the current can reverse the direction of the magnetization. As explained earlier, the external in-plane (IP) magnetic field (H_x) is required in for out-of-plane (OOP) systems during SOT driven magnetization reversal to break the

symmetry of the system and determine the final magnetic state. From the critical current, device dimensions and resistivities, a critical current density (J_c) equal to $\sim 2 \cdot 10^{11}$A/m^2 was estimated for a 160 mT external in-plane field (H_x).

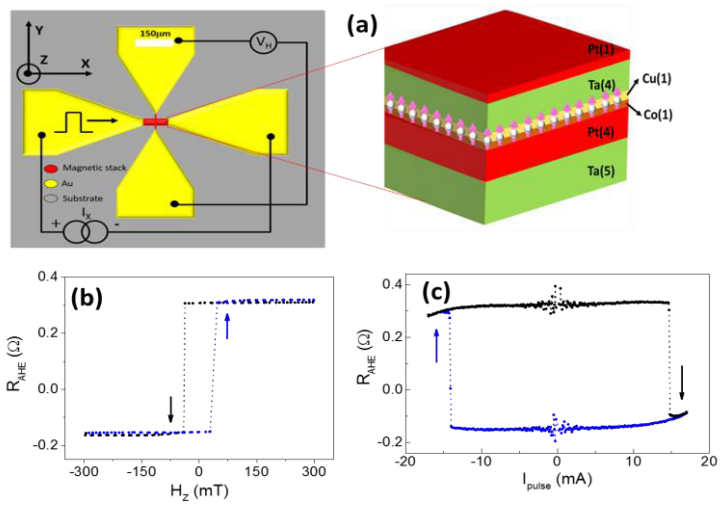

Figure 4.2 Sample and switching behavior via field and current. a) Magnetic sample stack and Patterned Hall bar structure using the magnetic stack and gold contact pads. The schematic shows the electrical connections used for Anomalous Hall resistance ($R_{AHE}= V_H/I$) detection. (b-c) shows the hysteresis loop response of the sample under external magnetic field (H_z) and current I_{pulse} respectively.

As the external in-plane magnetic field (H_x) in increased, the critical current density (I_c) drops as expected from SOTs [86–88](figure 4.3). The sample switches to $-M_z$ ($+M_z$) when the in-plane magnetic field (H_x) and the charge current (I) are parallel (antiparallel), in agreement with a SOT raising from the combination of the spin Hall effect from both heavy metals [31,89]. These symmetries will be useful for comparison while probing the SOT driven magnetization dynamics at the picosecond scale.

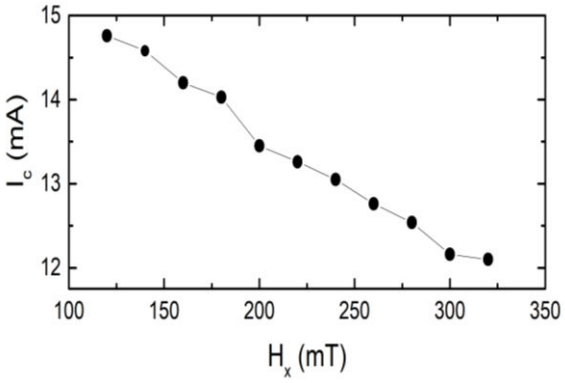

Figure 4.3 The critical current density for SOT switching with 100 μs pulses is inversely proportional to the in-plane H_x field, as reported previously [90]

The next section will focus on the use of picosecond electrical pulses to induce SOTs.

4.2.3 On-chip picosecond spin-orbit torque detection

Schematic of a typical experimental setup to probe the picosecond SOT magnetization dynamics is shown in figure 4.4. A high intensity femtosecond laser beam (pump beam) was focused on the photoconductive switch using a lens of 15cm focal length. The pump beam diameter of ~150μm was observed at the sample position. To probe the magnetization dynamics, a delayed low intensity femtosecond laser beam (probe beam) was focused on the magnetic specimen via a $\times$ 50 objective with 10cm focal length as shown in figure 4.4. Due to the small size of the magnetic specimen, a probe diameter of ~1μm was used throughout the measurements. A chameleon oscillator laser system with 80MHz repetition rate, ~200fs wide laser pulses was used throughout the measurements reported in chapter 4.2. An amplifier laser system with 5KHz repetition rate, ~30fs pulse duration was used for full magnetization reversal in Co(1)/Cu sample reported in chapter 4.3.

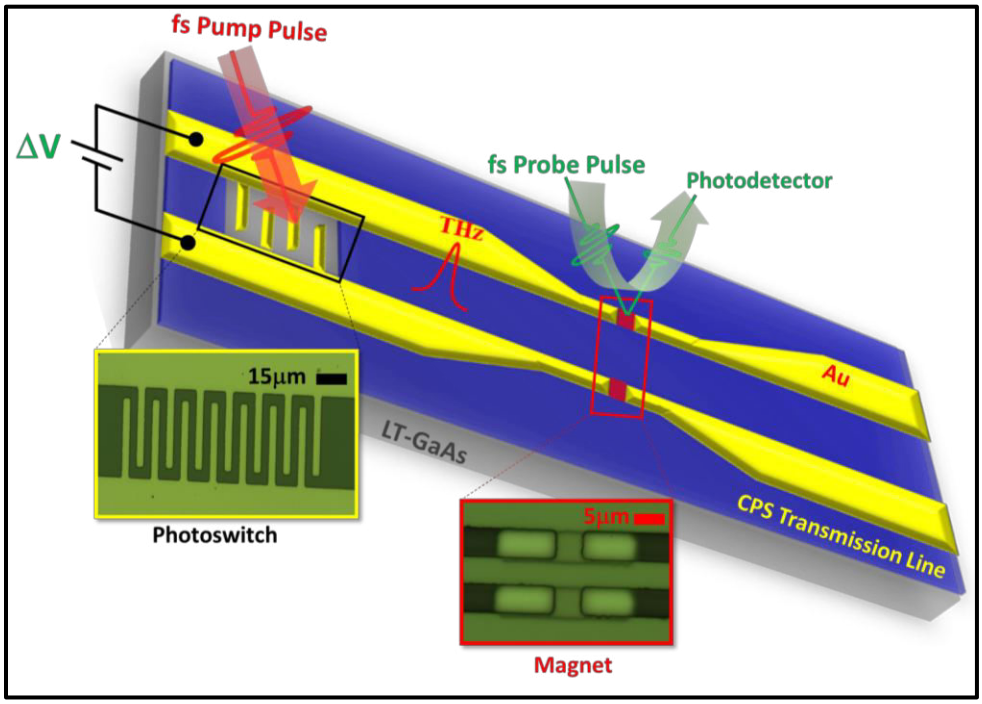

Figure 4.4 Schematic representation of the experimental setup used for on-chip picosecond SOT driven magnetization dynamics detection.

As a reminder, all the static and time resolved MOKE measurements were taken in the polar MOKE geometry and hence the signals represents the magnetization vector along the z-axis.

The next section comprises different measurements we usually take on each sample before probing the time-resolved magnetization dynamics. First few tests to check the performance of the photoconductive switch. Secondly, time-resolved electric-field component, time domain thermal reflectance (TDTR) measurements to know the exact profile of electrical signal that is

interacting with the sample along with the corresponding temperature induced response of the sample. Hysteresis loop measurement were also performed to check the static magnetic properties of the sample and also to normalize the TRMOKE signal (explained in later section).

4.2.3.1 Photoconductive Auston switch performance

Prior taking any measurements on the THz devices, the photoconductive switch performance was tested by monitoring the dark- (non-illuminated) and photo- (illuminated) currents as a function bias voltage (ΔV) and pump power (P_{pump}). Figure 4.5 (a) represents the change in dark and photocurrent as a function of pump power (P_{pump}) for three different bias voltage values (ΔV) on a typical CPS structure based device. These measurements were undertaken while the pump beam was sourced from the 80MHz oscillator laser system. A relatively linear trend is observed for the pump power and bias voltage sweep.

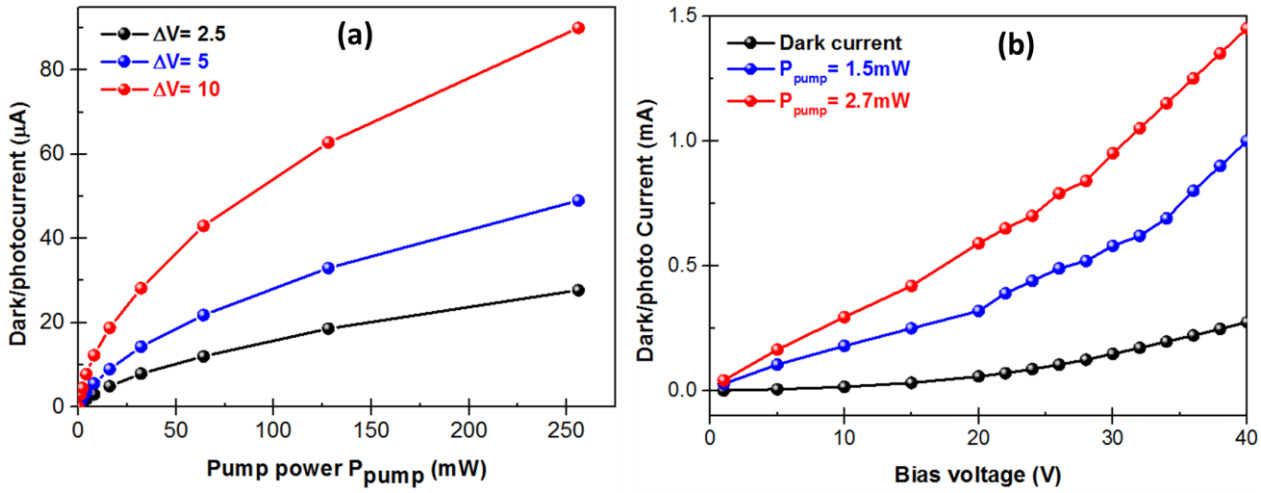

Figure 4.5 Dark and photocurrent measurements for as a function of pump power and bias voltage for (a) 80MHz oscillator and (b) 5KHz amplifier laser systems

Figure 4.5 (b) represents the similar measurements on one of the co-planar waveguide structure based device where the pump beam was sourced from the 5KHz amplifier laser system. A similar behavior for both, the bias voltage and pump power sweep was observed on these device. A clear difference in the photocurrent values shown in figure 4.5 (a) and (b) is mainly attributed to two parameters. Firstly, due to the difference in photoconductive switch geometry co-planar stripline and co-planar waveguide structure based devices. Secondly, it can also be due to the slight difference in the lithography output. It will be great interest to see how the magnetization will get affected as a function of bias voltage and pump power anf hence the photocurrent.

4.2.3.2 Time-domain thermal reflectance (TDTR)

After testing the photoconductive switch performance, time-domain thermal reflectance (TDTR) measurements were undertaken to hunt for the time-zero by observing a sudden change in the reflectivity as a result of temperature rise in the magnetic system after the arrival of electrical pulse. Figure 4.6 represents the electrical TDTR measurement taken on one of the co-planar waveguide structure based device. The graph in the inset represents that the magnetization dynamics (in red) starts almost at the same time as the electrical pulse arrival. The TDTR dynamics are surprising and we still do not fully understand them. Initially a negative signal is observed at time zero, which we attribute to the electronic response of the system. Right after a positive signal is observed, which should be the lattice response. However, the signal keeps increasing well after the THz pulse has traversed it. This might be related to the reflections that keep heating up the system, or to some non-intuitive heating profiles (due to dissimilar metals with different electron-phonon coupling constants for example Choi *et. al., 2014* [91]) that slow down the lattice response. At longer time, after 5 ps, we observe a common slow recovery in the TDTR signal as the temperatures in the system cool down via the substrate.

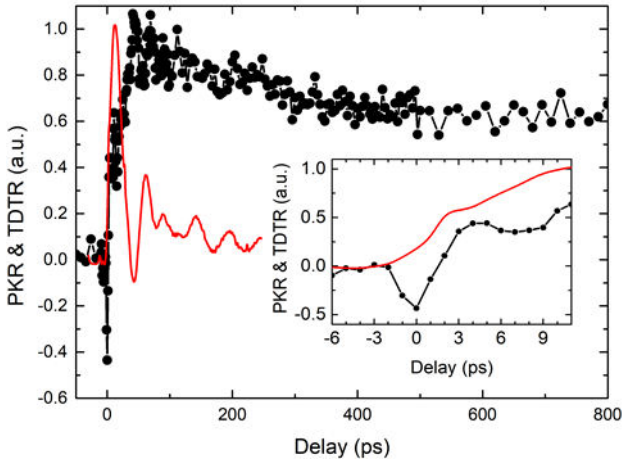

Figure 4.6 Electrical TDTR on CPW device (in black) along with the magnetization dynamics curve (in red)

4.2.3.3 Time-resolved electric-field detection

Since the pulse duration is the critical parameter for the spin-orbit torque induced magnetization dynamics and therefore the detection of time-resolved e-field signal in order to know the exact pulse duration of the THz current pulse is required. The e-field measurement is also useful to understand precisely the magnetization dynamics. As discussed in section 3.3.2 of chapter 3, the reflection from various parts of the THz device are also observed and hence the magnetization dynamics are also affected by these additional reflections along with the real pulse. Figure 4.7 represents the time-resolved e-field measurements taken on one of the

transmission line structure. The trace shown in Figure 4.7 (b) is obtained when the pump beam was sourced by the 5KHz amplifier laser system whereas for the trace in Figure 4.7 (c), the 80MHz oscillator laser was employed. The difference in the pulse duration of the generated electrical pulse is due to the difference in the way each laser system is exciting the photoswitch. For example, we have noticed that at high pump fluences or voltages the generated pulses become wider, as seen previously [57]. This observation is still not understood, particularly since some previous works showed an opposite effect [92].

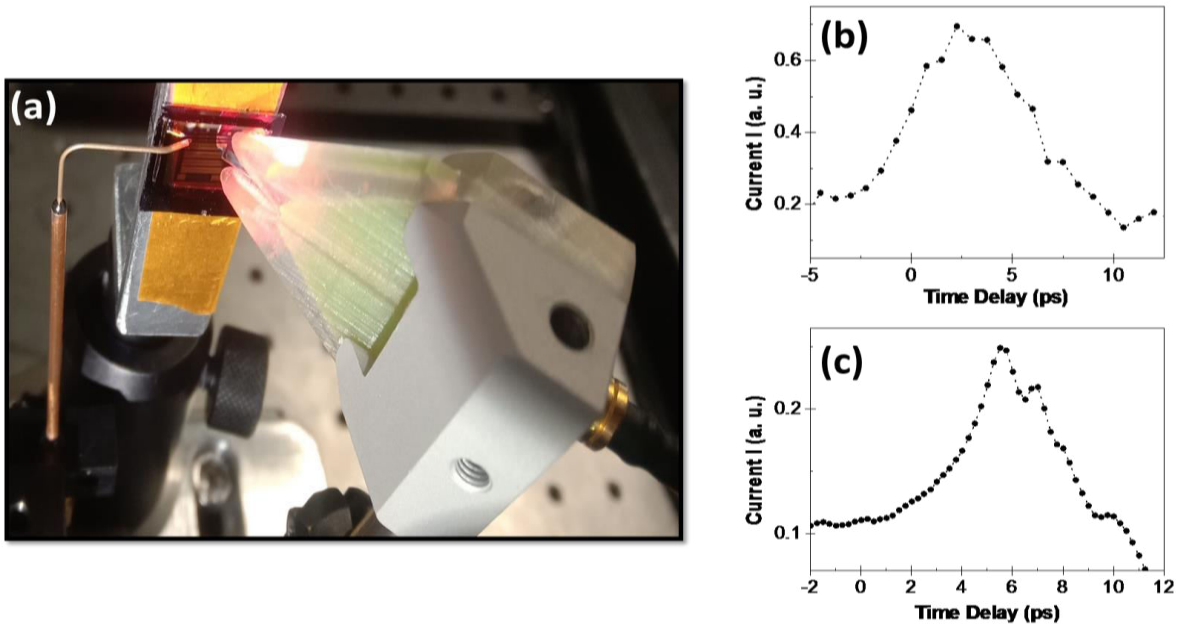

Figure 4.7 (a) Experimental setup to take time-resolved e-field traces, and e-field traces on (b) the 5KHz amplifier, and (c) 80MHz amplifier laser system.

In the referenced work they explained that the larger voltage bias would increase the charge acceleration and speed up (shorten) the pulses. In our experiments we also noticed that the duration of the detected pulse with the Teraspike® probe was larger at large probe powers (we assume static heating was affecting the performance). We therefore reduced the power until the width of the pulse stayed constant and independent of the probe power. The reported electric field traces are all performed under these conditions. After performing electric-field measurements on different devices (with different photoswitches), it was observed that the pulse duration of the generated electrical signal is almost constant in the various devices for the 80MHz oscillator system.

4.2.3.4 Normalization of Kerr rotation θ_k into magnetization (M)

As explained in chapter 3, the TRMOKE signal is detected using a lock-in amplifier, which provides voltage signal (V_{out}) corresponding to the change in the Kerr rotation ($\Delta\theta_k$). To

convert the V_{out} into θ_k, equation 3.40 is used. Under most circumstances, we know that $\theta_k \propto M_Z$, which means that $\Delta\theta_k/\theta_{k,max} = \Delta M_Z/M_S$ where $\theta_{k,max}$ is the Kerr rotation at saturation. Therefore, to further normalize $\Delta\theta_k$ in terms of normalized change in magnetization ($\Delta M_Z/M_S$), we need to know $\theta_{k,max}$. When the external magnetic field is strong enough to saturate the magnetization in both directions, $\theta_{k,max}$ is easy to obtain from a hysteresis loop as shown in Figure 4.8(c). However, when attempting to saturate the magnetization along the hard axis for example, the required field is too large for our setup. We therefore need to compare the magnetization response obtained with our Kerr setup (Figure 4.8(a)) and that obtained with another tool with access to higher fields, such as the VSM(Figure 4.8(b)). So, when exploring the hard axis magnetization, we convert the Kerr rotation into magnetization by using the ratio of the acquired data via the two methods at same field values (we obtain almost-linear slopes at low field and can use equation 4.1). We can then normalize by using the measured M_S.

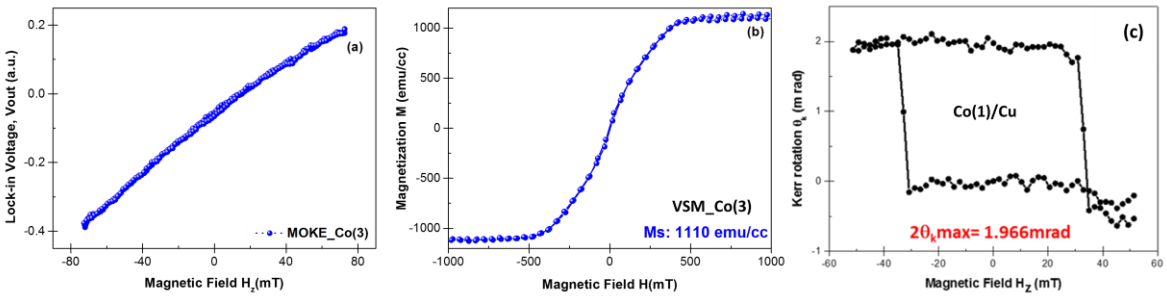

Figure 4.8 (a) Kerr rotation induced voltage (Vout) on the Co(3) sample as a function of out-of-plane magnetic field (b) Magnetization hysteresis loop obtained from VSM measurements on the Co(3) sample, and c) Kerr rotation of a Co(1)/Cu as a function of the out-of-plane magnetic field.

$$\frac{M_Z}{\theta_k} = \frac{dM_Z/dH}{d\theta_k/dH};\ \left(\text{Unit: } \frac{emu/cc}{rad.}\right) \qquad 4.1$$

The hysteresis loop measurements shown in figure 4.8(a) was undertaken for Co(3) sample to get the slope from MOKE. To obtain the data shown in Figure 4.8 (a) in terms of magnetization (M), the M-H hysteresis measurement obtained from VSM (Figure 4.8(b)) were used. The contribution of substrate during the VSM measurement at high external magnetic fields was eliminated before comparing it with the MOKE response.

4.2.4 Picosecond SOTs in out of the plane magnetized thin films

In this section we report the spin-orbit torque induced magnetization dynamics induced by a 3.7 picosecond electrical pulse on the Co(1)/Cu sample with out-of-plane magnetization. The

dependence of various external parameters such as the bias voltage (ΔV) and pump power ($\mathrm{P_{pump}}$) along with the conventional spin-orbit torque symmetries are reported in the following subsections.

4.2.4.1 Spin-orbit torque symmetries

As explained in section 4.2.2, for Co(1)/Cu sample, the final magnetic state is determined by the combination of polarities of external in-plane magnetic field *(*H_X) and the electrical pulse. Similar verification of these spin-orbit torque symmetries were done by taking TRMOKE measurements for all the different combinations. In these experiments, we monitored (ΔM_Z) via polar MOKE. A typical magnetic response to the pulses is shown in Figure 4.9. We plot the normalized change in magnetization ($\Delta M_Z / M_S$) as a function of time delay Δt for different excitation conditions (black, red, blue curves). The y-scale on the left corresponds to an initial saturation along $+M_Z$ whereas the y-scale on the right is for the $-M_Z$ direction.

We first focus our attention on the dynamics under zero in-plane field (signal in black). The response of the Co magnetization to the current is instantaneous. For $+M_Z$ and $-M_Z$, the out-of-plane magnetization ($\Delta M_Z / M_S$) decreases rapidly and recovers slowly. Let us explain this observation via the schematic shown in figure 4.10 (a-b). This rapid decrease in the magnetization is due to two mechanisms. First, the damping like spin-orbit torque pulls the magnetization towards the y-direction. Second, the picosecond charge current pulse induces Joule heating, which leads to an ultrafast loss of magnetic order[57], commonly known as ultrafast demagnetization[57] [4].The latter mechanism and the subsequent slow cooling by heat diffusion explain the slow recovery at long time delays.

We now focus on the dynamics under in-plane magnetic field $\pm H_X$ (signal in blue and red). Unlike for the zero-field (signal in black), the magnetization is not initially oriented along *z*. In the presence of an in-plane field ($H_X = \pm 160\mathrm{mT}$) pointing along *x*, the magnetization at negative time delay ($\Delta t < 0$) is tilted in the *x-z* plane to be parallel to the effective field (H_{eff}). The value of external in-plane magnetic field (i.e. $\pm 160\mathrm{mT}$) was choosen for two main reasons. Firstly, the achieveable field strength with the TRMOKE setup is limited to ~200mT and secondly, to have a field that is very small in comparison with the saturation field (i.e. ~1T) in the in-plane direction.

As detailed earlier, the in-plane field breaks the symmetry of the system and, together with the injected spin polarization σ_Y, determines the sign of precession and hence the final direction of magnetization. A parallel (antiparallel) in-plane field and current causes the moment to precess towards (away from) –*z*, causing $\Delta M_Z / M_S$ to decrease (increases) on a 10-ps timescale. This

occurs regardless of the initial up ($+M_Z$) or down ($-M_Z$) saturated magnetic states, as expected from the spin-orbit torque and in agreement with the result of our quasi-static spin-orbit torque switching experiments (represented in figure 4.2). This result can also be understood via the schematic shown in figure 4.10 (c). The precessions in figure 4.9 are offset by the heating-induced demagnetization. In addition to reducing the magnetization, ultrafast Joule heating reduces the magnetic anisotropy. We also depict this effect in figure 4.10 (d). As the temperature rises, the anisotropy field $H_a(T)$ drops and, under a constant external field, the angle (and amplitude) of the effective field H_{eff} ($\Delta t < 4ps$) changes.

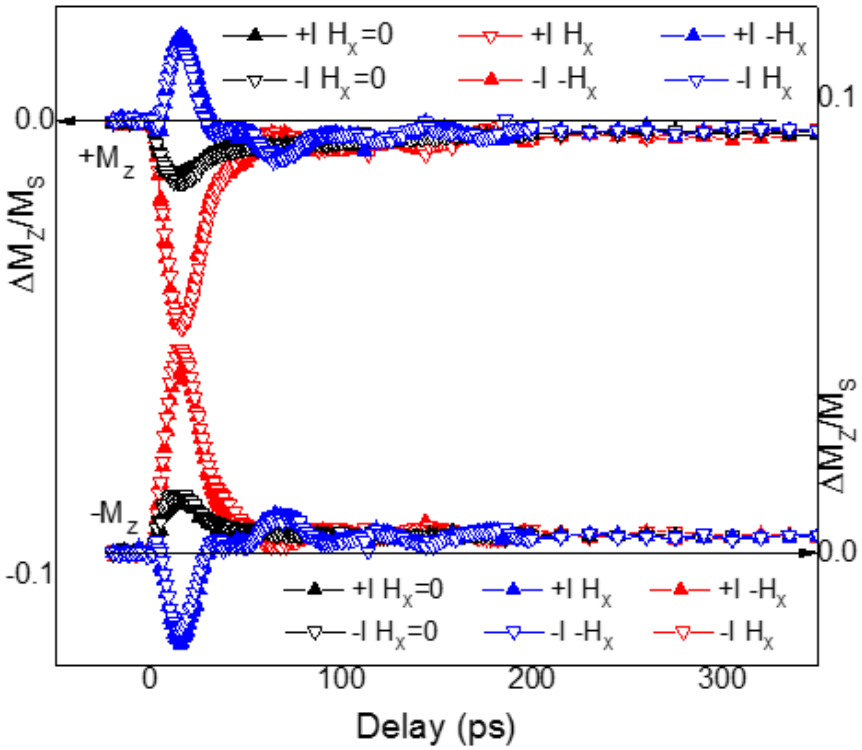

Figure 4.9 Picosecond Spin-orbit torque driven magnetization dynamics in SOT_PMA_Cu sample

The magnetization experiences a torque (τ_{Heff}) due to the change in angle of H_{eff}. The torque τ_{Heff} is enhanced by the damping-like spin-orbit torque τ_{DL}, which pulls the magnetization even further from H_{eff}.

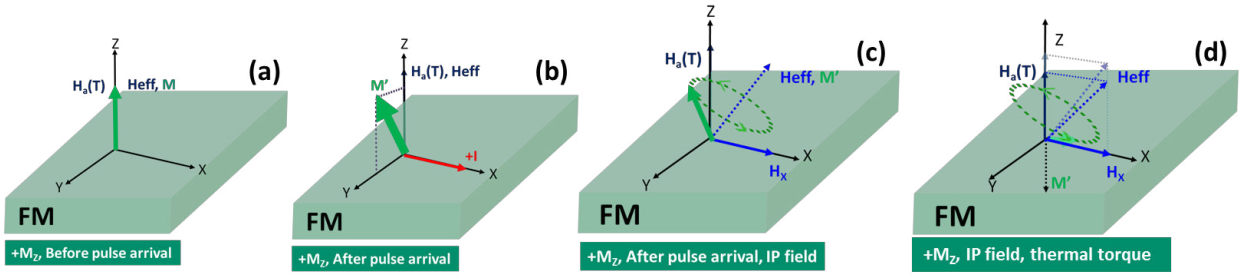

Figure 4.10 Schematic representation of the movement of magnetization at different excitation conditions.

The torque τ_{Heff}, which we call the thermal anisotropy torque, is commonly used in ultrafast pump-probe ferromagnetic resonance (FMR) experiments as a way to trigger oscillatory dynamics[11] [93]. Surprisingly, the thermal anisotropy torque alone can lead to a complete magnetization reversal in ferromagnet, as was recently demonstrated using femtosecond optical pulses[94].

4.2.4.2 Fitting of the magnetization dynamics with a macrospin model

The results in figure 4.9 were fited with the macrospin model predictions (model explained in section 3.4). A full list of the parameters used to fit the magnetization dynamics and the source for their value is listed in table 4.2. We remind the reader that the anisotropy field and magnetization are both temperature-dependent [82].

Table 3 Tabular representation of the fitting parameters used to fit the magnetization dynamics after both optical and electrical excitation

	Name	Variable	Value	Units	Source
LLG	Saturation magnetization	M_S (300K)	10^6	Am^{-1}	VSM measurement
	Magnetic anisotropy field	B_K (300K)	0.8	T	Optical pump-probe data fit
	Damping	α	0.23	---	Optical data fit
	Thickness of magnetic layer	d_0	1	nm	Estimated from growth rate calibrations
	Thickness of full metallic stack	d	16	nm	Estimated from growth rate calibrations
	Damping-like spin Hall angle	θ_{SH}^{DL}	0.3	---	Set as in similar stacks from article [33]
	Field-like spin Hall angle	θ_{SH}^{FL}	0.05	---	Free parameter
	Current density	J_c	variable	Am^{-2}	Free parameter (values shown in Figure captions)
Thermal	Curie Temperature	T_C	800	K	Optical data fit & experience from previous samples.
	Volumetric total heat capacity	C	$2.6 \cdot 10^6$	$Jm^{-3}K^{-1}$	Weighted average value from [79] Typical 1-3 $MJm^{-3}K^{-1}$
	Interface thermal conductance	G_{int}	$170 \cdot 10^6$	$Wm^{-2}K^{-1}$	Free parameter. Typical 100-300 $MWm^{-2}K^{-1}$ [19 59 6 97].
	Thermal conductivity	Λ (300K)	9	$Wm^{-1}K^{-1}$	Wiedemann-Franz Law $\Lambda = L_0 T/\rho_e \sim 10$
	Electrical resistivity	ρ_e	$81 \cdot 10^{-8}$	Ωm	4 points measurement

We first determined some of the model parameters such as the anisotropy, damping constant, and thermal dependence of the magnetization and anisotropies via optically pumped time-resolved MOKE experiments. To this aim, we first orient the magnetization of the Co with an out-of-plane magnetic field of 0.3 Tesla. After removing the out-of-plane magnetic field, we optically irradiate the sample surface with 250 fs duration pump pulses at a fluence of 0.7 J m^{-2} under the application of an in-plane magnetic field. The transient temperature response causes precessional dynamics, due to the thermal anisotropy torque. We track the resulting out-of-plane component of the magnetic moment by monitoring the polar Kerr angle with a time-delayed probe pulse. We repeat this experiment with varied in-plane magnetic fields.

Figure 4.11 (a) shows the time-resolved magneto-optic Kerr response of a Co(1)/Cu sample co-grown on a glass substrate (same growth as that of the THz devices) to optical irradiation, under an in-plane field of 0, 0.15, and 0.3 T. The lines in Figure 4.11(a) are best-fit model predictions for the data based on the LLG equations, including the thermal model. We note that due to the glass substrate, the interfacial conductance is lowered to G_{int}~100 MWm^{-2}K^{-1}. Using an optical multilayer calculation as described in[98], we estimate the absorbed fluence per pump pulse *F,* (i.e. 0.3 Jm^{-2}). We estimate that this absorbed fluence should cause a per-pulse temperature rise of approximately *F/(d. C)* ~7K. Comparing this temperature rise to our experimental measurements of the resulting ΔM_Z, allows us to quantify $\Delta M_Z/dT$ close to room temperature (i.e. for small heatings, just like in the spin-orbit torque time-resolved MOKE). The amplitude of precession of $\Delta M_Z(t)$ following heating provides information about $\Delta MK \ \ /dT$. The frequency and decay rate of precession allow us to determine the total anisotropy field and effective damping.

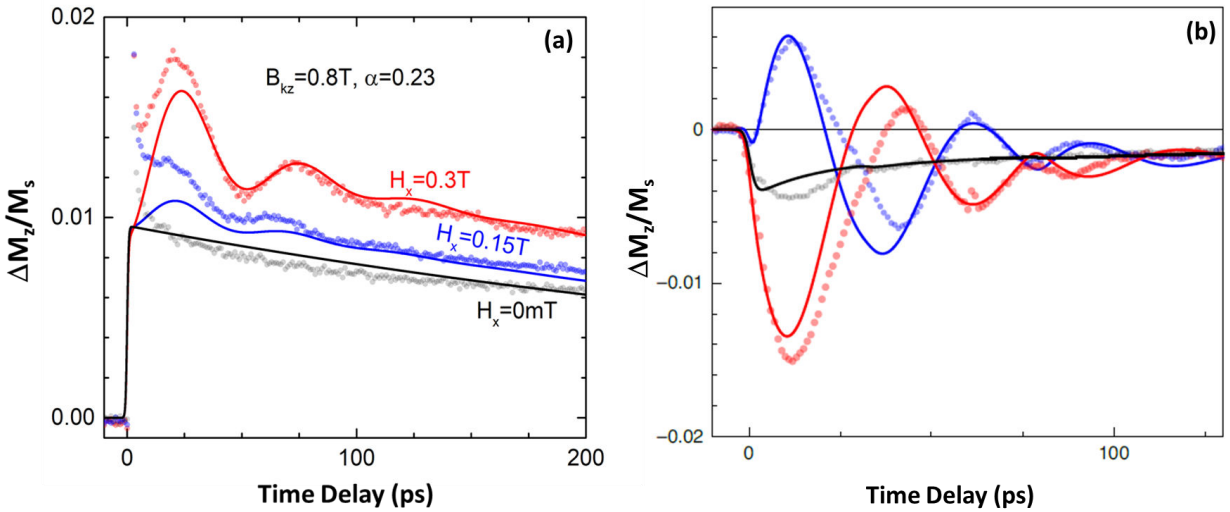

Figure 4.11 (a) Time-resolve magneto optic Kerr effect of the optically and (b) electrical pumped Co(1)/Cu sample. The magnetization is pointing in the $+M_z$ direction. Black data points correspond to a positive current and no in-plane field. Blue data points correspond to a positive current and negative in-plane field. Red data points correspond to a positive current and positive in-plane field.

Thanks to the optical pump-probe experiments, we have now very few parameters left to fit the data in figure 4.11(a). More specifically, we are only missing the current density J_c and the spin-to-charge conversion parameters (spin Hall angles θ_{SH}^{FL} and θ_{SH}^{DL}), as well as the interface conductance G_{int}. In figure 4.11(b) we plot the experimental data (doted) along with the macrospin model prediction (line) for different configurations. The interfacial thermal conductance determines the recovery of the magnetization at long time-delays, whereas the current density and spin Hall angles determine the amplitude of the oscillations. The field-like spin Hall angle in particular, is important to fit the subtle pre-overshoot (or kink) of the blue curve present in the presence of the current pulse. We also had to include a number of electrical reflections of the current pulses from the end of the transmission lines, which affect the magnetization dynamics. These reflections are best seen at around 75 ps when there is a phase change in the dynamics. The best fits shown in figure 4.11(b) resulted in damping-like and field-like spin Hall angles of 0.2 and 0.05, respectively. Both values are reasonable, and a damping-like dominant torque agrees well with the reports on similar structures [33]. The fit reproduces most features in the data.

Even though the macrospin model describes the overall dynamics, it's predictions do not agree with certain features in the experimental data. In particular, the model does not match the dynamics of the black trace at $H_X = 0$ between 3 and 35ps. A possible explanation is inhomogeneous broadening. In the optically excited time-resolved MOKE measurements for damping and anisotropy, we observed an effective damping parameter larger than 0.2. Previous pump-probe studies of the dynamics of perpendicularly magnetized films show that such a large effective damping parameter is caused by inhomogeneous broadening [93]. In addition to inhomogeneities in anisotropy, it is possible that there are spatial inhomogeneities in the excitation, either due to the (spin) current distribution or hot spots.

In the next section, the dependence of various other parameters such as bias voltage, pump power, and external field amplitude on the magnetization dynamics are explained.

4.2.4.3 External field amplitude dependence

As discussed in section 4.2.2, the external in-plane magnetic field (H_X) plays a vital role in breaking the symmetry of the system and induces magnetization switching. Figure 4.12 shows the dependence of the picosecond SOT driven magnetization dynamics on the external in-plane magnetic field. During quasi-static SOT measurements (see figure 4.3) it was found that the reversal was assisted by the in-plane magnetic field (the critical current density decreased). During the picosecond SOT measurements shown in figure 4.9, similarly, we observe an increase

in the amplitude of the dynamics facilitated by the external in-plane magnetic field. The measurement shown in Figure 4.12 were taken on the co-planar stripline-based device for a fixed pump power of 65mW and a bias voltage of 10 V.

It can also be observed that the frequency is not strongly dependent on the external magnetic field. This is to be expected, since the out-of-plane anisotropy is relatively larger than the applied fields. From the precessional period (~13 GHz) we can estimate the total anisotropy field (including interfacial and shaped anisotropy) to be ~0.5 T. Even the strongest in-plane field of 210mT should not modify the frequency by more than 5-10%. We also note that a slight difference in precessional frequency is observed beetween figure 4.9 (red color) and figure 4.12. We attribute this difference to a slight variation in the growth of the interfaces, which might affect the interface anisotropy.

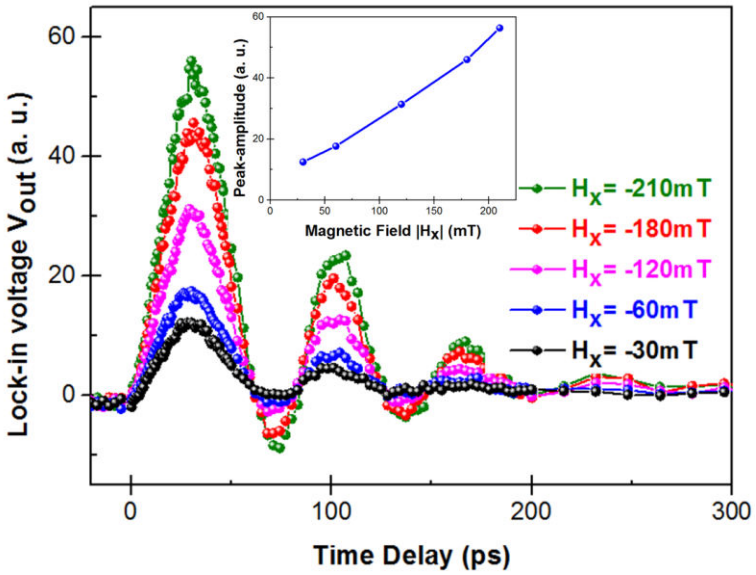

Figure 4.12 External in-plane magnetic field dependence on the SOT induced magnetization dynamics in Co(1)/Cu sample; (Inset: Peak amplitude of lock-in signal versus external in-plane magnetic field)

4.2.4.4 Bias voltage dependence

Figure 4.13 shows the picosecond SOT driven magnetization dynamics of the Co(1)/Cu sample as a function of the bias voltage applied across the photoconductive switch. In figure 4.13(b), we compare the amplitude of the first oscillation with the photocurrent measured at the given bias voltage. Despite limited data, it appears that the amplitude of oscillations is growing at the same rate as the photocurrent does with the voltage. This almost linear relation between oscillation amplitude and photocurrent is possibly explained by the employed current range in which heating effects ($\propto I^2$) are limited. For further analysis, more time-resolved traces as a function of voltage will be taken over a larger range of bias voltages and fits using the

micromagnetic model will be attempted.

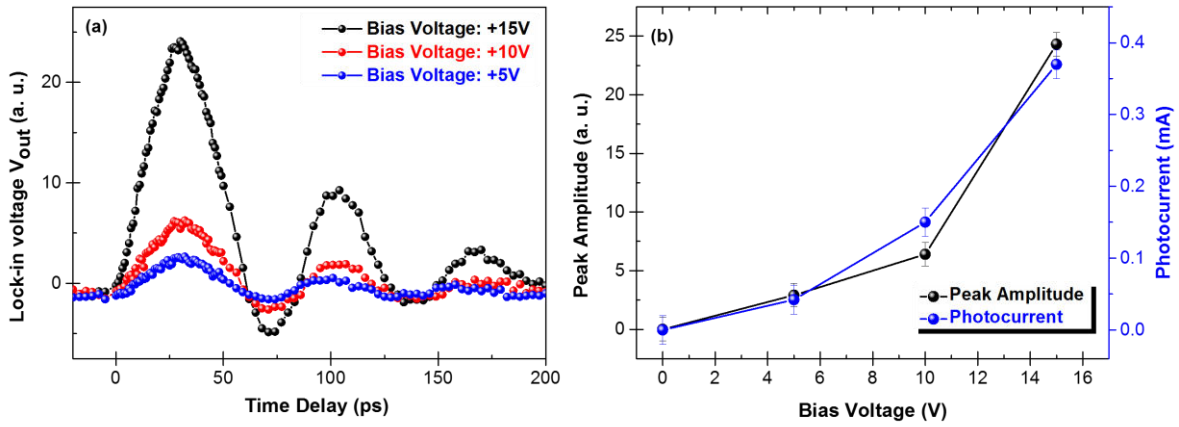

Figure 4.13 Dependence of ps SOT driven magnetization dynamics on the bias voltage applied across the photoconductive switch

4.2.4.5 Pump power dependence

Similar to the bias voltage, Figure 4.14 shows the dependence of the picosecond SOT induced magnetization dynamics of the Co(1)/Cu sample on the femtosecond laser pump power that is irradiated on the photoswitch. The dependence of pump power on peak amplitude of the first oscillation is presented in the inset of figure 4.14(a). Figure 4.14(b) presents the photocurrent values and first peak amplitude as a function of pump power.

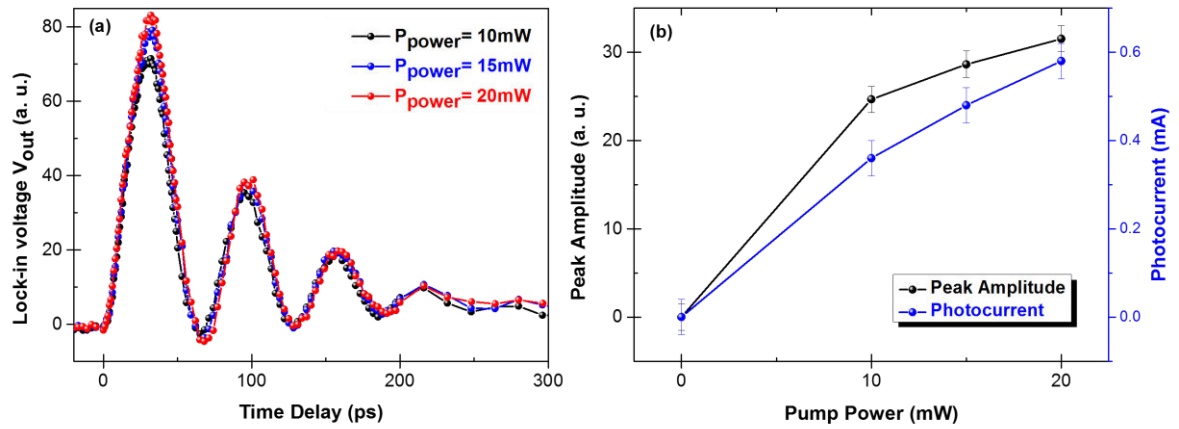

Figure 4.14 Laser pump power dependence on the ps SOT induced magnetization dynamics in Co(1)/Cu sample

The dependence of the oscillation amplitude on pump power is small in comparison to the dependence on the bias voltage, but so is the photocurrent too. Ultimately, because what drives the dynamics is the picosecond pulse, it is its amplitude and temporal profile that should be properly characterized for each voltage and pump power condition. For this reason, in future

experiments, we will systematically characterize the pulse characteristics under all voltage and pump-probe conditions.

4.2.4.6 Discussion and Conclusion

In this section we systematically varied various parameters that control the dynamics induced by our picosecond current pulses on out-of-plane magnetized 1nm thin Co ferromagnetic films. The SOT symmetries associated with the samples were verified both by using μs and ps wide electrical pulses. The external in-plane magnetic field was also found to be assisting the dynamics and the reversal. Dependence of various THz electrical pulses parameters (by changing the bias voltage across the photoswitch and the femtosecond laser pump power) onto the magnetization dynamics were also measured. Further in detail experiments and simulations needed to confirm if our simple macrospin understanding of the dynamics is adapted or not. These further analysis might help elucidate the impact of heating ($\propto I^2$) vs SOTs ($\propto I$).

4.2.5 Picosecond SOTs in in-plane magnetized thin films

As discussed earlier in section 4.2.1, two different magnetic heterostructures were used to study picosecond SOTs in driven magnetization dynamics in the in-plane magnetized Co ferromagnet. The schematic samples Co(2), and Co(3) are shown in figure 4.15(a-c). The division of subsections is similar to as it was for the OOP magnetized Co(1)/Cu sample including the SOT symmetries, dependence of various external parameters on the magnetization dynamics.

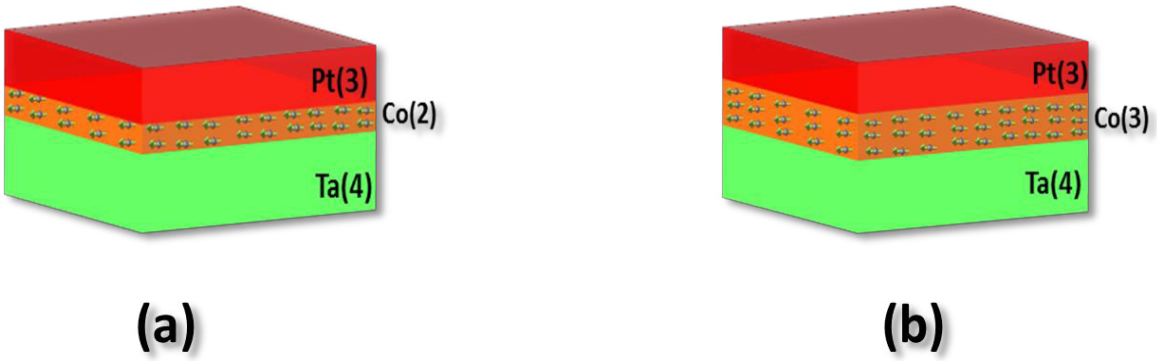

Figure 4.15 (a-b) Schematics of Co(2), and Co(3) samples respectively

4.2.5.1 SOT symmetries

The symmetries associated with SOTs in the in-plane magnetized samples were studied by performing the TRMOKE measurement for different combinations of the polarity of the THz pulse (hence the direction of SOT) and the polarity of the external in-plane magnetic field (H_X).

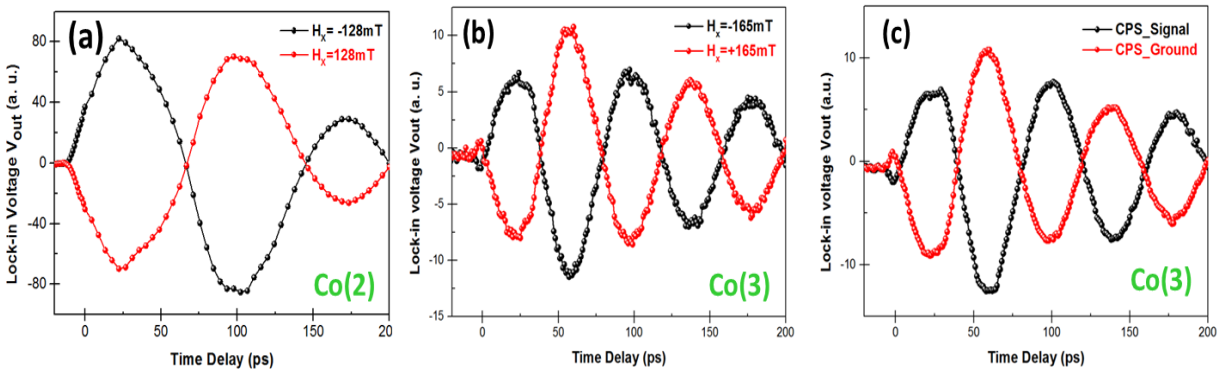

Figure 4.16 SOT symmetries in (a) Co(2), and (b-c) Co(3)/Cu samples

Figure 4.16 (a) shows the SOT induced magnetization dynamics in the Co(2) sample under both in-plane field polarities (H_X= ±128mT) at a fixed bias voltage of +20V. Figure 4.16(b) shows the same response for the thicker Co(3) sample, only with a slight difference in-plane field strength. The different external in-plane field as well as the difference in thickness are responsible for the different precessional frequencies observed in both samples. A small kink in the signal near zero time delay in the case of Co(3) sample is observed, which is not present in the Co(2) sample. When fitted with a macrospin model (see blue line in figure 4.11(b)), the kink appears to be related to the field-like torque. Interestingly, the amplitude of the first oscillation in sample Co(3) is smaller in comparison with the second oscillation. The origin of this decrease is not yet clear, but might be related to the field-like torque and/or the ultrafast demagnetization.

The measurement shown in figure 4.16(c) is taken on the Co(3) sample, under an in-plane magnetic field of ~130mT, to further verify the SOT symmetry by probing the same dynamics on both the signal and the ground lines of the co-planar stripline. The polarity of the THz pulse and hence the SOT acting on the Co ferromagnet is opposite for both lines, therefore reversing the observed response. An adittional conclusion from the data in figure 4.16(c) is that we can safely exclude the influence of Oersted fields generate from one line onto the other line of the transmission line. This is because Oersted fields generated by the current flowing in one line on the other line have the same direction. Therefore they should lead to a common signal of the same sign and amplitude on the two curves in figure 4.16. As shown in figure 4.16(c) the data is rather symmetric, excluding this possibility. However, internal Oersted fields due to the distribution of the current density within the stack are likely to be present, but would yield the same response as a field-like torque and are thus difficult to distinguish.

4.2.5.2 Bias voltage and pump power dependence

The dependence of bias voltage and pump power on the SOT-induced magnetization dynamics in the in-plane magnetized samples is very similar to what we observed for the Co(1)/Cu sample. Figure 4.17(a-b) shows the bias voltage dependence for Co(2) and Co(3) samples respectively. The measurements shown below were taken in the presence of a constant external in-plane magnetic field H_x= -128mT and H_x= -150.5mT for Co(2) and Co(3) respectively.

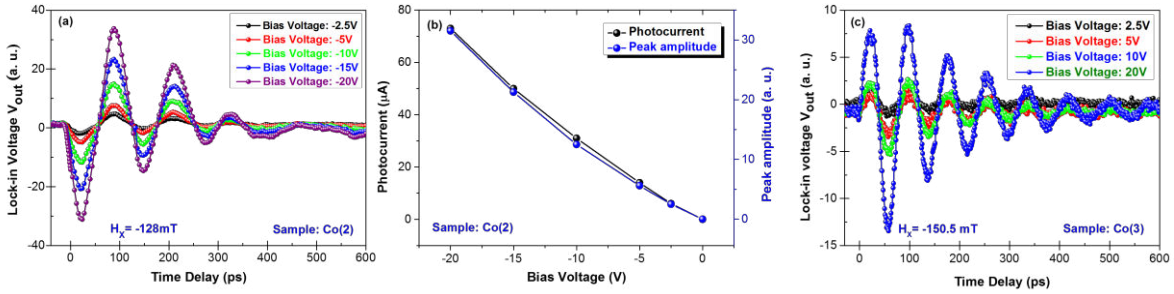

Figure 4.17 (a, c) Bias voltage dependence on the ps SOT induced magnetization dynamics in Co(2) and Co(3) samples respectively, and (b) dependence of photocurrent and peak amplitude of first oscillation from magnetic dynamics as a function of bias voltage for Co(2) sample

Figure 4.17(b) shows the dependence of first peak amplitude and photocurrent value on the applied bias voltage. The dependence of bias voltage on the peak amplitude is comparable with the dependence on the photocurrent value (Figure 4.17(b)).

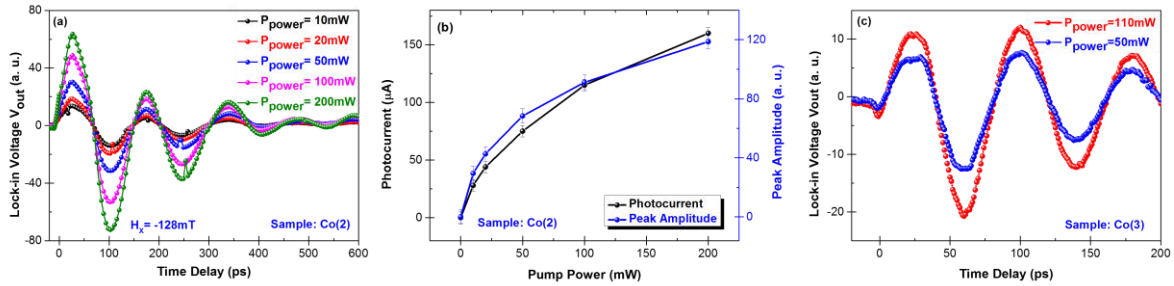

Figure 4.18 (a-c) Pump power dependence on the ps SOT driven magnetization dynamics in Co(2), Co(3), and Co(3)/Cu samples respectively

Figure 4.18(a-c) shows dependence of magnetization dynamics for Co(2), and Co(3) samples respectively on the the pump power. The measurements were taken at a constant bias voltage of 20V. In figure 4.18(b), the dependence of peak amplitude of the first oscillation as a function of pump power is presented. The dependence of the peak amplitude on bias voltage and pump power is comparable with how the photocurrent value is changing as a function of both parameters (Figure 4.17 and 4.18(b)). In conclusion, the dependence is essentially related to the photocurrent values generated during the THz generation.

4.2.5.3 External field amplitude dependence

Finally, the dependence of external magnetic fields on the SOT-induced magnetization dynamics is represented in figure 4.19. The data shown in figure 4.19(a-b) is for Co(2), and Co(3) samples respectively for different external in-plane magnetic fields (H_x). The peak amplitude as well the precessional frequency is directly proportional to the external field strength for both Co(2), Co(3) samples. The experimental results were also compared with the macrospin model for Co(3) as shown in figure 4.19(b) which accurately capture the right precessional period (dark line represents the theoretical macrospin model prediction).

Effect of external out-of-plane magnetic field on the amplitude and the precessional frequency of the magnetization dynamics again verifies the presence of SOT in the dynamics along with the ultrafast demagnetization.

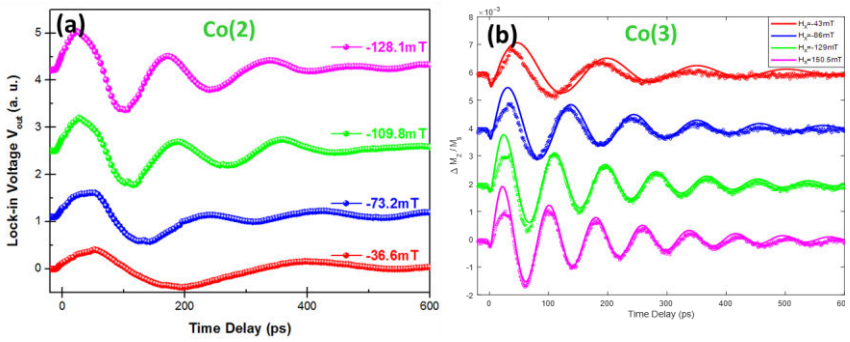

Figure 4.19 (a-b) External in-plane field dependence on the ps SOT magnetization dynamics for Co(3), and Co(2) samples respectively

4.2.6 Reflections and their impact on magnetization

A detailed study of spin-orbit torques induced picosecond magnetization dynamics is undertaken in the previous sections. There is a noticeable difference in the magnetization dynamics going from one type of device to another (in particular co-planar stripline to co-planar waveguide). Part of these noticeable differences are attributed to distinct reflections of the THz pulses that are present in the devices. These reflections are due to an impedance mistmatch at different positions on the transmission line as discussed in chapter 3.

Figure 4.20(a-b) shows the magnetization dynamics on the co-planar waveguide-based Co(1)/Cu sample. As discussed earlier, the co-planar waveguide-based devices are designed such that the ground line (the line with photoswitch on it) is floating if the transmission line is not closed from the other end. The curves shown in figure 4.20(a) are observed when the transmission line was shorted from the end or in other words, the THz pulse reaching the end (right side of the line) will bounce back towards the magnetic sample. The left side of the transmission line is

connected to the keithley sourcemeter via CPW 40GHz GGB and coaxial cables. This reflected THz signal will have the same polarity concerning the initial pulse that is interacting with the magnetic sample. Due to this reflection, an additional spin-orbit torque (small in amplitude) is acting onto the magnetic sample after 28ps which corresponds to the time it requires for the THz to cover twice the distance from magnetic stack to one end of the transmission line. The influence of which is visible during the second oscillation (figure 4.20(a)).

To further verify that indeed the reflected signal is playing a crucial role in the magnetization dynamics, we closed the transmission line by connecting it to a 50 Ohms resistor with the help of an impedance-matched radio-frequency (RF) probe (i.e. CPW 40GHz GGB probes). The output signal corresponding to this condition is shown in figure 4.20(b). Since there is no reflection from the end of the transmission line the original trajectory of the magnetization is not perturbed.

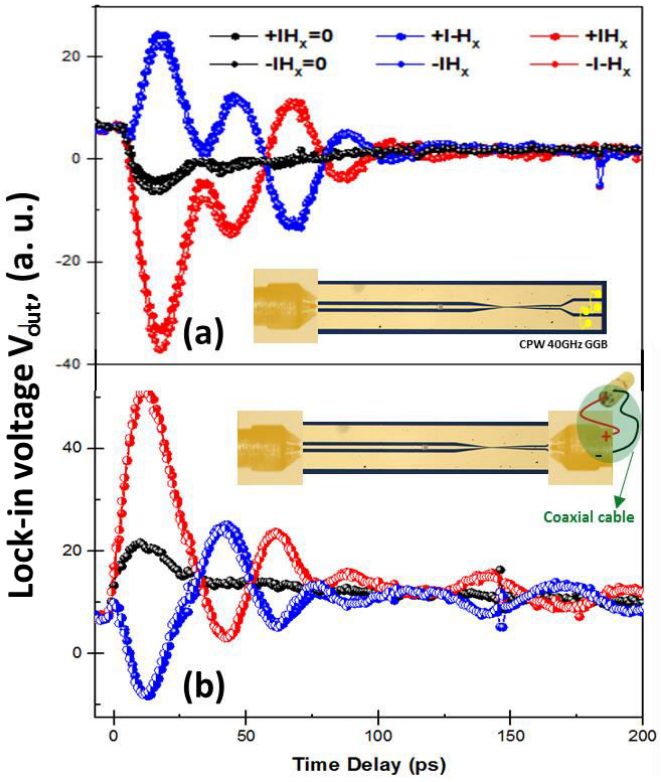

Figure 4.20 Spin-orbit induced magnetization dynamics (a) with just the wire bond and (b) With wire bond and impedance-matched RF tip

The reflected signal from one end of the transmission line may also lead to some interesting applications. The reflection polarity and time of arrival can then be engineered by choosing the transmission line dimensions and impedances, in order to assist or hinder the reversal. If the reflection condition can be dynamically changed, they could be used as a gate-like control for the writing of the magnetic memory.

4.2.7 Discussion and Conclusion

A systematic study of picosecond SOT-driven magnetization dynamics was undertaken in the above chapter. The SOT symmetries were verified on different in-plane magnetized samples. Similar to OOP magnetized sample, the external in-plane magnetic field was directly proportional to the precessional frequency. Dependence of various THz electrical pulses parameters (by changing the bias voltage across the photoswitch and the femtosecond laser pump power) onto the magnetization dynamics were also undertaken. The pump power and bias voltage were found to have a similar effect on the magnetization dynamics which was essentially related to the photocurrent values.

In the next section, we will demonstrate full magnetization reversal induced by spin-orbit torques, using higher current intensities.

4.3 Magnetization reversal via picosecond spin-orbit torques

This chapter comprises the study undertaken as a continuation of chapter 4.2 where the spin-orbit torque-driven magnetization dynamics in picosecond time scales were explored. The energy per pulse used to study the dynamics was tilting the magnetization only by ~10° (<5% reduction in M_z). Using spin-orbit torques to reverse the magnetization completely is the ultimate goal of the study as it has the potential to bring advances in the energy-efficiency and/or speed of spintronic. For the magnetization reversal study via SOTs in picosecond time scales, the out-of-plane (OOP) magnetized sample (i.e. Ta(5nm)/Pt(4)/Co(1)/Cu(1)/Ta(4)/Pt(1)) is used.

4.3.1 Procedure for picosecond SOT switching experiments

After performing the conventional quasi-static spin-orbit torque switching measurements presented in figure 4.2, we performed switching experiments on picosecond time scales using picosecond wide electrical pulses. We focused on a sample with perpendicular magnetic anisotropy (PMA) of particular interest to perform the switching experiments from both the industrial as well as technical aspects for us. As discussed at the beginning of chapter 4, and chapter 2 that the magnetic systems with high magnetic anisotropy in particular the PMA/uniaxial anisotropy are considered to be more promising systems from the application point of view. To monitor the out-of-plane magnetization we used a polar MOKE microscope.

As discussed in chapter 4.2, the magnetization dynamics were obtained using an oscillator laser system with a repetition rate of 80MHz, ~200fs pulse duration, and the spot size such that when applied a laser power of ~30mW, energy per pulse was ~0.37nJ. For switching we needed to use a laser system with much higher energy per pulse. For this purpose, we replaced the 80MHz oscillator laser system with a 5KHz amplifier laser system. To generate the picosecond wide electrical pulses, a pump pulse of ~30fs was focused on the photoconductive switch with a 15cm lens. A full width at half maxima (FWHM) radius of about 150μm pump beam (with ~0.3μJ energy per pulse) was then used to generate the picosecond electrical pulses. A 6ps wide electrical pulse was generated on the co-planar waveguide (CPW) device as shown in figure 4.7 of chapter 4.2.

The experimental setup for magnetization reversal experiments is pretty similar to what has been done during the magnetization dynamics detection explained in chapter 4.2. The detection in these experiments is static MOKE microscopy instead of TRMOKE. To switch from the

TRMOKE to MOKE microscopy setup, we simply need to flip the flipper mirror in front of the objective as explained in chapter 3.

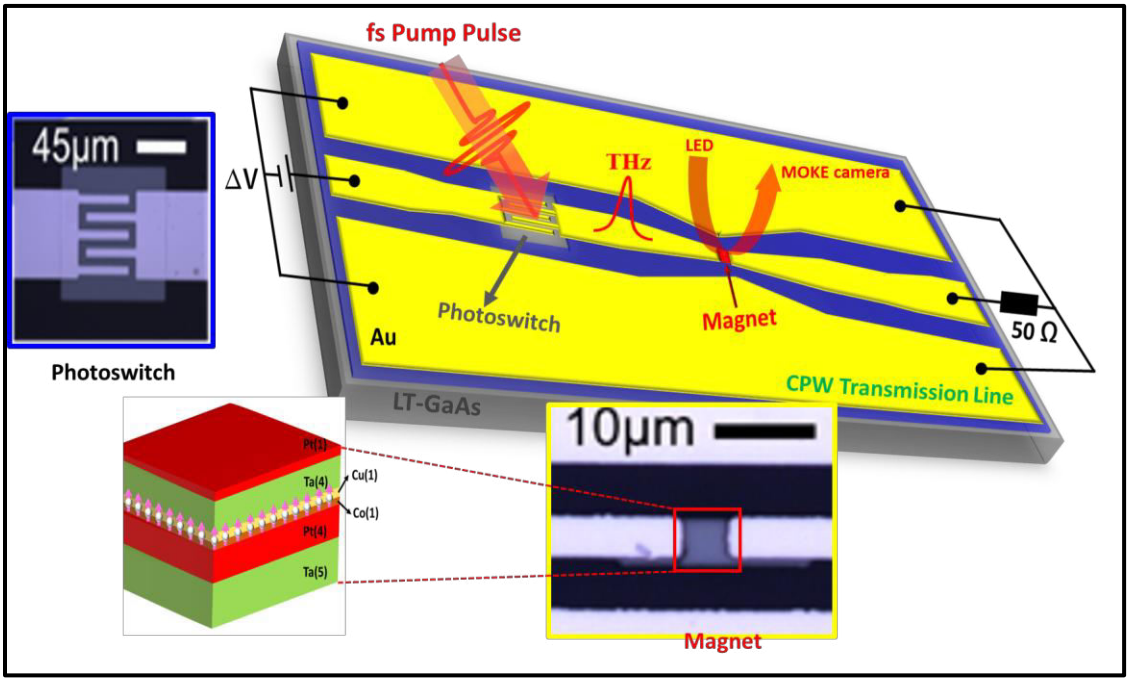

Figure 4.21 Setup for generation of picosecond electrical pulses and magneto-optical detection on co-planar stripline structure

Figure 4.21, represents the schematic of the experimental setup used to perform the ultrafast spin-orbit torque-driven magnetization reversal studies. As mentioned earlier in chapter 3, a single 1cm×1cm chip has six different devices in total depending on various parameters such as the transmission line structure (i.e. co-planar stripline (CPS)/co-planar waveguide (CPW), different photoconductive switch parameters as a result of the difference in switch geometry). From a technical point of view, it is easier for us to work with co-planar stripline structure-based device since the number of electrical contacts can be reduced for example: the end of the line can be left open whereas, in the case of a co-planer waveguide (CPW), the end needs to kept close since the switch design is such that it keeps the circuit incomplete (open) if the end is not shorted or connected with an impedance matched resistor. The precise detail of the impact of letting the line shorted, open, or connected with impedance matched resistor and it's impact on the magnetization dynamics as a result of various reflections on the device are explained in chapter 4.3.

We begin first with saturating the Co ferromagnetic thin layer along ($-M_z$) and applied the maximum external IP field that was available on our setup (~ -160mT). We then begin with changing the pump power (from few μW to 1.5mW) and the bias voltage (ΔV: from 0 to +65V) to hunt for the minimum possible values of both the parameters where the magnet switches

from ($-M_z$) to ($+M_z$). Figure 4.22 represents the MOKE microscopy images corresponding to the initial saturation state of the ferromagnet (i.e. $-M_z$) and the final magnetization states after the injection of a single 6ps wide electrical pulse and hence the SOT (pump pulse of 1.5 mW was used) for different values of bias voltage. We note that in these experiments when the threshold was found the voltage was not increased too much more in order to avoid the risk of damaging the photoswitch.

For one device, we found that starting from 0-48V bias, the magnetization remains unchanged and afterward, a slow reversal began. The full reversal was observed at a bias voltage of 64-65V and hence we know the threshold voltage for magnetization reversal in the particular device. It can also be observed from figure 4.22 that the magnetization reversal might not be a coherent process and rather a multiple domain wall nucleations (see the state for 57V). A detailed discussion over the possible switching mechanisms is provided in the later sections.

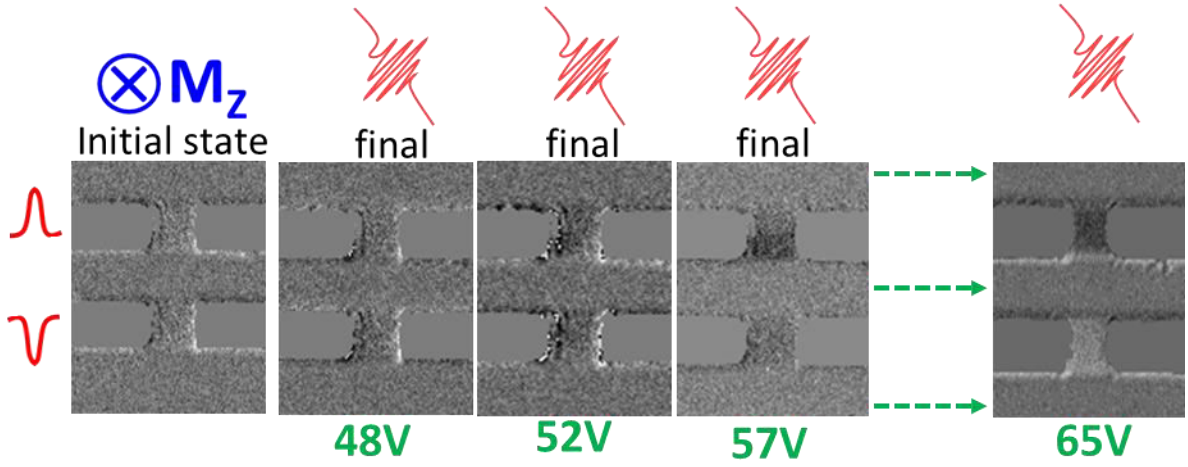

Figure 4.22 MOKE micrographs of single 6 ps electrical pulses switching the magnetization via SOT in co-planar stripline based devices

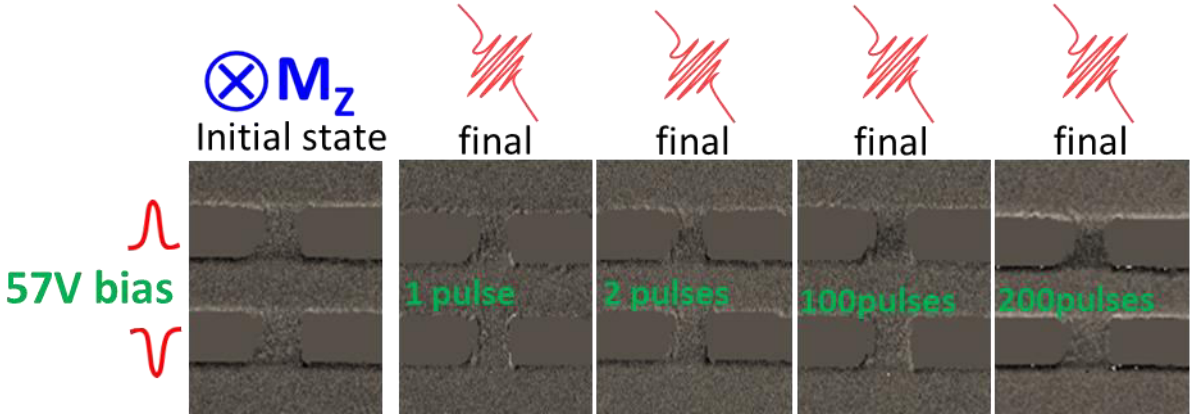

Figure 4.23 MOKE micrographs of single 6 ps electrical pulses switching the magnetization via SOT in co-planar stripline based devices

We have also tried to perform the same switching experiment slightly below the threshold bias voltage i.e. at 57V and found that even after injecting ~100pulses, the magnetization reversed only by 50 %, and a full reversal was observed after injecting ~ 200pulses as represented in figure 4.23.

The direction of the spin-orbit torque was controlled by controlling the bias voltage polarity that was applied across the photoconductive switch. The next section i.e. 4.3.2 is a summary of the switching measurements that we performed on the co-planar waveguide (CPW) structure-based device. As mentioned earlier, working with CPW based devices is slightly more demanding in terms of the additional electrical contacts but it's a better device to work with while analyzing the results. For the CPW structure, the magnetic load is deposited on the central conductor line. Due to the symmetric nature of the transmission line, one need not to worry about the Oersted fields generated by the top and bottom ground conductors as they cancel out one another's contribution.

4.3.2 Picosecond SOT switching on co-planar waveguides

To perform similar switching measurements on the CPW structure-based devices, we connected the left side of the transmission line with a 40GHz GBB probe tip. The right side of the transmission line was also connected with the same tip to close the circuit by connecting the end of the line with a 50 Ohm resistor as shown in figure 4.24.

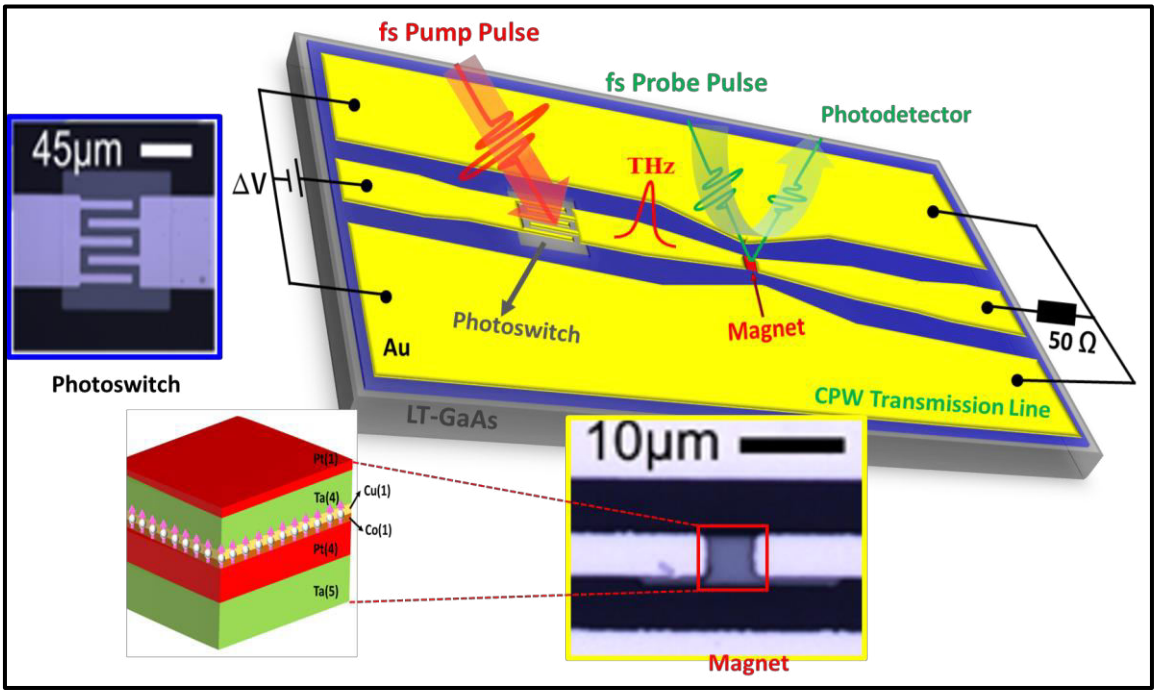

Figure 4.24 Setup for generation of picosecond electrical pulses and magneto-optical detection on co-planar stripline structure

Figure 4.25 shows polar magneto-optical Kerr effect (MOKE) micrographs of the initial configuration and final state after a single 6ps electrical pulse, for various configurations. In each of the four quadrants of figure 4.25 various combinations of current I and in-plane magnetic field H_x directions were tested. Here, current (I)represents nothing but the direction of the spin-orbit torque (SOT) that is being applied to the ferromagnet by controlling the polarity of the bias voltage as discussed in the previous section. After testing all the possible polarities, we observed that parallel (antiparallel) current (I) pulses and external IP field result in $-Mz$ ($+Mz$), just as expected by the symmetries of the SOTs in the prepared stack. Moreover, we observe that the final state is independent of the initial magnetic state of our stack. We injected up to 10 successive pulses of the same polarity and saw no difference in the final state. We successfully repeated the experiment (initial saturation + single shot) at the switching voltage for n =35 times. As soon as the bias voltage ΔV is decreased below 40V, no more reversal is observed. When the in-plane field is reduced below ($H_x \sim 120$ mT) no reversal is observed, likely requiring higher current densities, as also observed by Garello *et al.* [3]. In this work, we did not explore higher current densities in order to avoid the risk of degradation or permanent damage of the photoswitch. To test the device endurance, we subjected the device to electrical pulses at switching conditions ($\Delta V \sim$40V), a repetition rate of 5kHz, for 5 hours ($> 10^8$ pulses). After the endurance testing, we noticed no degradation or change to the electrical and magnetic properties.

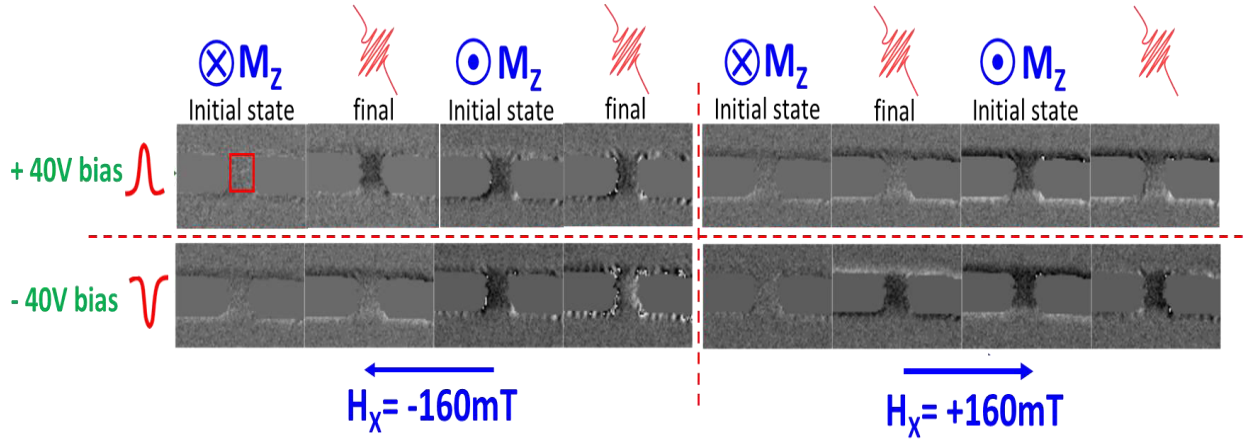

Figure 4.25 MOKE micrographs of single 6 ps electrical pulses switching the magnetization via SOT in co-planar waveguide based devices

4.3.3 Picosecond SOT switching on co-planar striplines

After confirming the spin-orbit torque symmetries as shown in the previous section, we switched back to the co-planar stripline (CPS) based device to check the symmetries again. The interest of checking these symmetries on a CPS structure is that the magnetic stack is deposited

on both the signal and ground lines of the CPS structure, unlike the CPW structure where the stack was deposited only on the central conductive line. Since the magnetic stack or the SOT stack is deposited on both the signal and the ground lines, when the picosecond electrical pulse is generated, for the same polarity of bias voltage, the electrical signal polarity for the magnetic stack on the signal and the ground lines are opposed to one another. Hence, the spin-orbit torque acting on the ferromagnetic Co layer is also opposite for both the lines and therefore the final magnetic states for the magnet on the ground and signal lines should be opposite to one another.

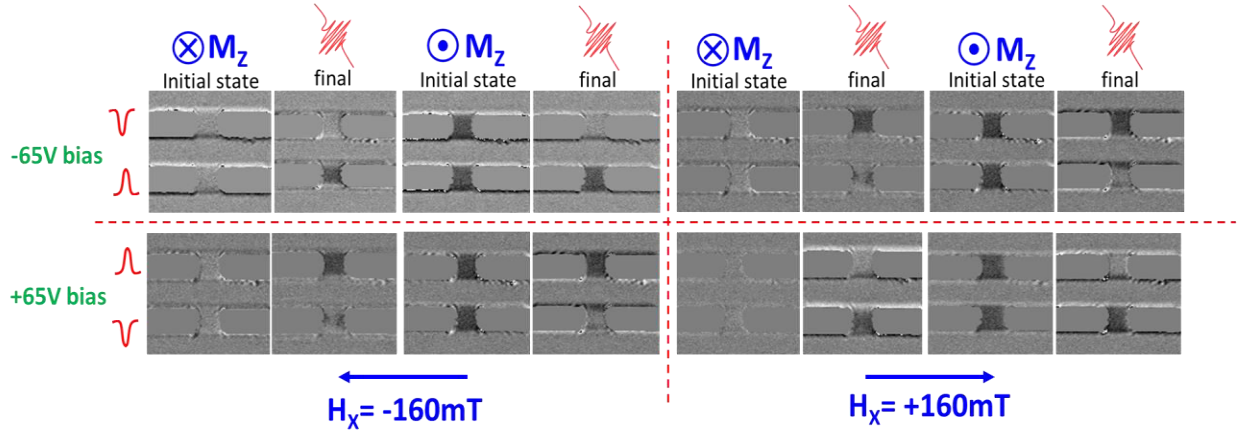

Figure 4.26 MOKE micrographs of single 6 ps electrical pulses switching the magnetization via SOT in co-planar stripline (CPS) based devices

Figure 4.26 represents the MOKE images of the initial and final magnetic states of the Co layer. It is clearly visible from the above figure that indeed the final magnetic states of both the ground and the signal lines are opposite to one another as expected from the spin-orbit torque symmetry arguments mentioned earlier. The threshold value of bias voltage for the CPS structure is found to be ~ 65V whereas it is ~40V for the CPW. This difference in the threshold bias voltage can be attributed to two different parameters. First, the dimensions of the switch, the number of fingers that are used to catch the generated picosecond electrical pulses are different for both the transmission line structures, and secondly, the dimension of the magnetic stack is slightly bigger for the CPW structure-based device. The magnetic stack is ~6μm × 5μm for the CPS structure whereas, it is 4μm × 5μm for the CPW.

4.3.4 Energy estimation

The pulse duration of the electrical signal used for the above spin-orbit torque (SOT) driven magnetization reversal is in picoseconds i.e orders of magnitude lower than the conventionally used wide electrical pulses and therefore it is expected to be orders of magnitude energy efficient as well. Since the Teraspike (photoconductive antenna) we have used to detect the

generated electrical pulses is not well calibrated for the amplitudes of the corresponding e-field component, the exact value for the electrical signal is unknown. Nevertheless, we performed capacitance measurements for one of our photoswitch that is fabricated on the co-planar waveguide (CPW) structure-based device, to estimate the maximum possible energy that can be stored and hence dissipated from the respective photoconductive switch. The upper limit to the energy dissipated at the load can be set by estimating the total initial energy stored in the photoswitch capacitor which is the energy that drives both the THz/ps current pulse in the transmission lines and the losses to THz radiation [99–98].

The capacitance of an interdigitated electrode (IDE) capacitor C_{IDE} is roughly $C_{IDE} = (N-1)\epsilon_r\epsilon_0 A/d$ where N is the number of electrodes, ϵ_r is the effective relative permittivity due to LT-GaAs substrate and air (measured as 15), ϵ_0 is the vacuum permittivity, A is the surface area of an electrode, and d is the center-to-center distance between electrodes. A capacitance of about $\sim 10^{-14}$ F was found for the photoconductive switch patterned on the co-planar waveguide structure device. As a second verification, it is also well known that the RC time constant due to the capacitance of the photoswitch limits the pulse duration of the generated pulses [103], which means we can also set an upper bound for the capacitance given by RC<3.7ps (which is our smallest measured pulse duration). Here, the characteristic impedance (Z_0) of the line plays the role of the resistor. The CPW line impedance was designed [77] to be $Z_0 = 70\Omega$, which means the capacitance is at most around $5.3 \cdot 10^{-14}$ F, consistent with our initial estimation. We will consider this upper-bound value as the capacitance of our switch to calculate the upper-bound energy dissipation in our experiments.

For the measured bias voltage at the switching threshold voltage of $\Delta V = 40$ V, the energy stored is $\frac{1}{2} C_{max} \Delta V^2 \sim 50$ pJ. In a worst-case scenario, if we assume a full discharge of the switch, no radiative losses, no transmission losses, and assume a perfect absorption at the magnet, then all of the energy stored in the switch capacitor would be dissipated on the load. For our magnetic load dimensions, this corresponds to an energy density of ~ 150MJ/m^3. Because the energy dissipation for a Gaussian current pulse is $E = \int J(t)^2 \rho \cdot \mathrm{d}t = 0.75 \cdot J^2 \, \rho \tau_\mathrm{p}$, where $\rho \, (= 81 \, \mu\Omega \cdot \mathrm{cm})$ is the measured resistivity of the magnet, we estimate the maximum peak current density for switching with $\tau_\mathrm{p} = 6$ ps pulses to be about $J_c \sim 6 \cdot 10^{12}$ A/m^2.

The value for resistivity was calculated using a four-point resistivity measurement. Using previously measured values of resistivity for 4-5nm Pt and Ta films deposited with the same sputtering system (24 and $200 \, \mu\Omega \cdot \mathrm{cm}$ respectively), and a parallel resistor model, we determine the correct effective resistivity by assuming that most of the current flow in the

13nm comprised by the 5nm Ta buffer, bottom 4nm Pt and top 4nm Ta layers, and neglecting the currents through the 1nm Co, Cu and Pt capping layers. We then estimate the critical current density by using again a parallel resistor model to calculate the amount of current going through Pt and Ta layers surrounding the Co/Cu bilayer.

4.3.5 Macrospin model predictions

Indeed, the magnetization reversal results are promising but to understand the physics behind this reversal is also of great importance. And to do so, we have used the simple macrospin model that is explained in section 3.4. We use the same parameters listed in table 3.

4.3.5.1 Dynamics at switching threshold

Since the energy per pulse for the 80MHz oscillator laser system is too low to get the time-resolved magnetization dynamics at the switching threshold, we tried to get these dynamics with the 5KHz repetition rate amplifier laser system. Probing the switching dynamics was still not possible even with our 5 kHz amplified laser system since on our MOKE setup, measurements require a minimum probe power of ~ 60 µW to resolve Kerr rotations of ~ 100 µrad. The study is still in progress to get to the time-resolved magnetization reversal measurements with a slightly different laser system (@100kHz repetition rate). Nonetheless, we tried to run the simulations to predict the magnetization dynamics at the switching threshold.

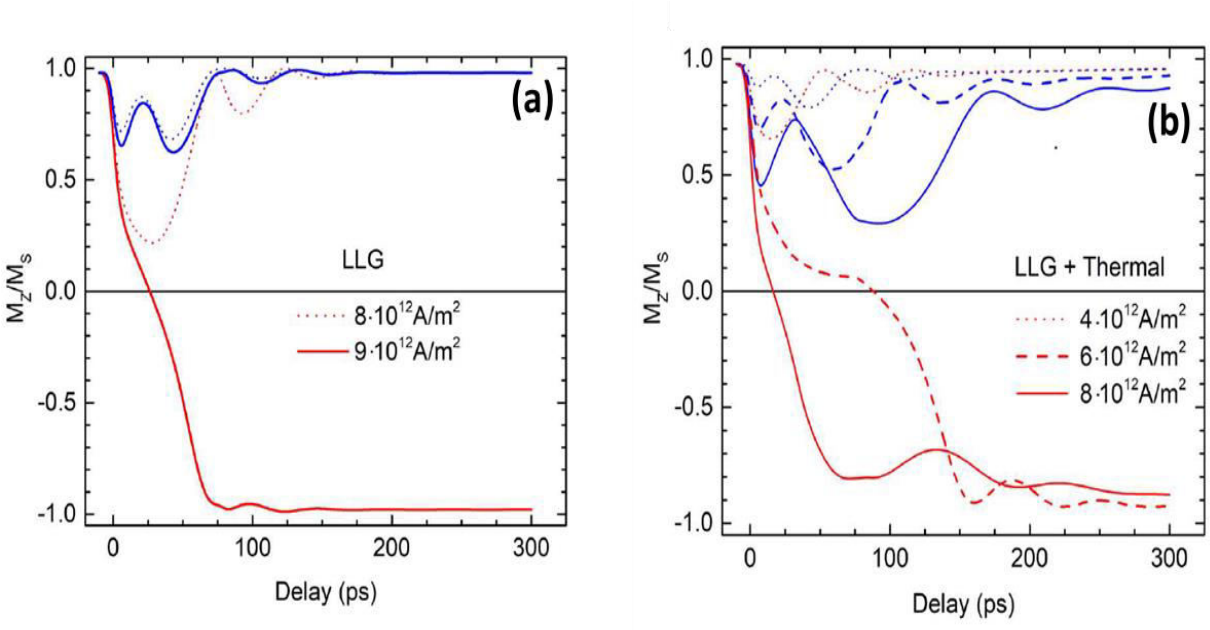

Figure 4.27 Strong current dynamics predicted with a 6 ps pulse.

To evaluate the role of temperature rises on the switching dynamics, the model parameters described above were used, to estimate the change in dynamics that results from the addition of temperature-induced precessional dynamics. An in-plane magnetic field of 0.16T and a 6ps wide pulse were set. The results of these simulations for two opposite current directions (plotted as blue and red) are shown in figure 4.27. Using the full thermal model (figure 4.27(b)) the critical current density is estimated to around $6 \cdot 10^{12}$ A/m^2 whereas when using a pure LLG with no temperature dependence (figure 4.27(a)) we need to increase the current up to $9 \cdot 10^{12}$ A/m^2 in order to observe switching. This corresponds to about a twofold increase in energy dissipation/consumption. The speed of reversal can vary quite a bit depending on the current density, but a minimum switching times around 16ps (for the crossing of zero magnetization) was observed for the shown parameters.

Interestingly, even if the spin Hall angles were set to zero (and thus have zero SOT) when the current density was increased to have enough of a temperature rise, then a strong enough thermal anisotropy torque will be present and lead to switching as shown in figure 4.28 This was also experienced in YIG by using ultrafast optical pulses [2], and the important requirements are: a) having dissimilar thermal derivatives of M and K, and b) to perform the experiment under a constant field perpendicular to the magnetic anisotropy axis.

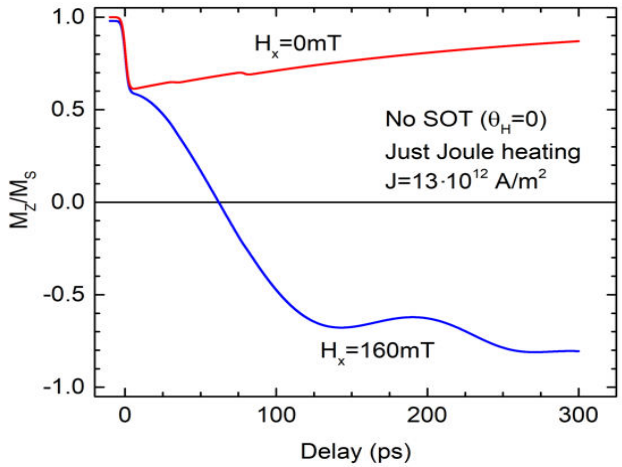

Figure 4.28 Switching with a 6 ps pulse purely via the thermal anisotropy torque

4.3.5.2 Critical current density vs pulse duration

In this section, the final outcome of the magnetic moment of the Co layer after a single current pulse, as a function of current density and pulse duration (Δt) was computed. The current density was increased for a given pulse duration until the magnetization's final state (end of the

pulse + 200ps) is reversed and record that current density as the critical current density. As shown in figure 4.29, two different scenarios were computed: Only LLG (red circles) and LLG + thermal effects (black open circles). The results for strong currents (such as here, for switching) when including thermal effects, are not representative of our samples necessarily, since the exact temperature dependence of M_S and K away from room temperature is not known. However, it is clear that ultrafast heating should lead to extra torques (just as in the case of optical pump-probe experiments) that should help the switching. Indeed, as figure 4.29 shows, the critical current density (figure 4.29(a)) and required energy (figure 4.29(b)) is smaller when including thermal effects. The ratio between the required critical current densities (energies) in both models is plotted as a dotted orange line in figure 4. 29(a-b)). With the used parameters, this ratio is at least ~1.5 thereby yielding at least a factor of 2 in energy gains.

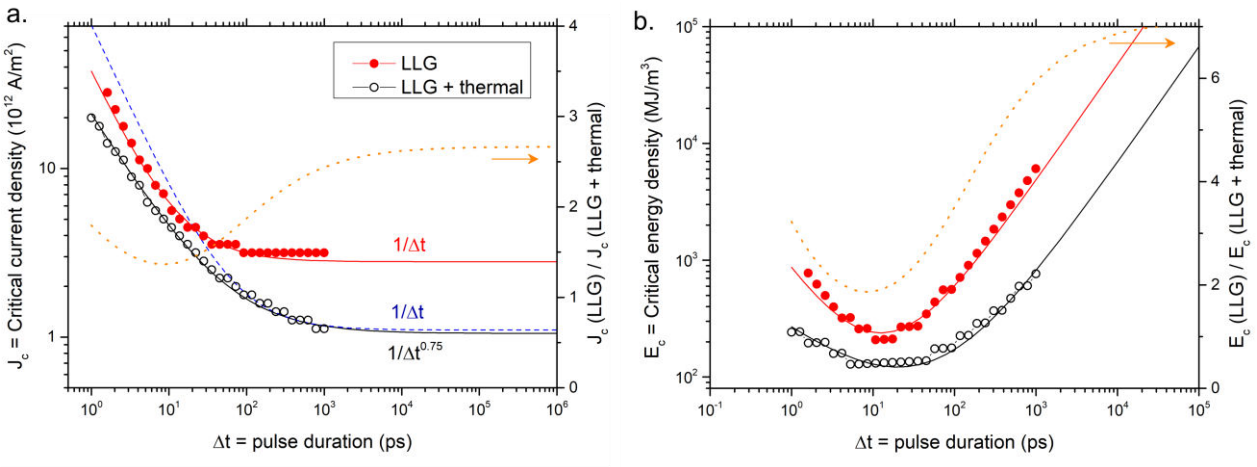

Figure 4.29 Simulated critical current densities as a function of current pulse duration

When using the macrospin LLG model (red line in figure 4.29), it was found that critical current is proportional to Δt^{-1} (+ an offset), which could mean that the spin angular momentum for switching is constant below a certain pulse duration, as suggested in [104]. Surprisingly, also in [104], a Δt^{-2} relationship was found using similar macrospin simulations. When the thermal effects were included (black empty circles) the relationship deviates from Δt^{-1}. However, it was observed that if we were to make a fit of the thermal estimates (black empty circles) using a Δt^{-1} relationship within a reduced range (between ~100ps and ~1ns as in reference [104], the fit would still work quite well (see blue dashed line) for that narrow range. This exercise highlights the difficulty in extracting the exact exponent when the range of the data is narrow.

Finally, it is interesting to look at the energy requirements on the right figure 4.29(b). Because of damping and anisotropy, as the current pulse gets wider than 10 ns, a large part of the angular momentum injected by the current pulses gets dissipated, and thus even more current is

required to keep increasing the precession angle, until switching is achieved. This results in an important increase in the required energy. On the other hand, when going into the very short pulse regime, even if less angular momentum is "wasted", more and more current density is required, resulting in stronger Joule heating. In between, around 10-20 ps for the used parameters (not far from the FMR half-period), a minimum of the required energy will be found. Curiously, it is around this minimum point that was found as the least difference between the two model's estimated critical energies.

4.3.6 Switching mechanisms

Switching via a spin-orbit torque on such a fast timescale brings up interesting questions about the mechanisms involved. According to our fits, the low current dynamics are almost fully coherent. However, as we approach the switching currents, more complex mechanisms such as magnetic domain nucleation and magnetic domain wall propagation might play a role. We will discuss some of these mechanisms in the following paragraphs. In particular, we will distinguish stochastic nucleation due to thermal noise and deterministic nucleation due to geometry, defects, or spatial inhomogeneities in the sample properties.

For long pulses, it is well known that thermal activation plays an important role in the nucleation of reversed magnetic domains, which followed by domain wall motion allows for full switching[105]. Thermal activation, and in particular the attempt frequency, is generally thought to be correlated to the FMR frequency [106]. In fact, the noise spectrum of a ferromagnet under a DC current has been experimentally found to peak at the FMR [107,108]. Therefore, when using current pulses wider than the FMR period ($\sim$40 ps, for $H_a \sim 1$ T), some degree of stochasticity should be expected. It is thus surprising that many works assume thermal activation should be negligible in the sub-ns regime [9,105,109–111]. Stochasticity in the context of sub-ns SOT switching has only been very recently reported [110,111]. If we now consider our experiments with 6ps pulses, well below the FMR period of our samples, stochasticity becomes more questionable. An important point to keep in mind is that with ps pulses the transient temperature rise (and thus thermal noise amplitude) in the film can be much larger than with ns pulses. In fact, thermal noise terms are successfully included in models for optically induced ps switching dynamics [52,112–114], but ultimately have a macroscopic deterministic role. Experimentally, few-nm sized nucleation points have been observed at the ps timescale [112,113], but are explained as a magnon localization [113] rather than classical domain nucleation (we remind that domain wall widths are typically ~5-10nm in equilibrium, and that a domain should be larger than two walls). At those length scales, the dynamics resemble those of a temperature-dependent macrospin model [114]. In summary,

the question of the role of thermal fluctuations at ultra-fast timescales is far from resolved, but we believe it is unlikely that stochastic nucleation of *classical* domains is taking place in our experiments.

If we then consider the switching to be purely deterministic, a few different scenarios are possible. We can first consider an edge-to-edge single domain wall sweeping scenario, assuming deterministic nucleation at one sample edge. Recently, it was experimentally shown [115] that even in large (4µm long) devices, SOT reversal with 0.2ns pulses could be driven by a single domain wall motion. Given our ultra-short pulses, this scenario would imply unphysical domain wall velocities [113] [15]of 10^5 m/s, too large for the estimated current densities. Therefore, we believe that, depending on the homogeneity of the sample properties, the switching in our samples could be either nearly coherent or governed by multiple nucleation events that happen within the current pulse and cover at least 50% of the area. Tracking the dynamics during the reversal could help in distinguishing between these mechanisms.

4.3.6.1 HAMR Scenario and dependence of coercivity on number of pulses

An alternative scenario would be to consider some form of heat-assisted magnetic recording due to Joule heating. In such a scenario the anisotropy barrier and/or magnetic order would be completely reduced by heating up to the Curie temperature T_c and any tiny torque could then determine the switching direction. To test for this scenario, we performed experiments where the in-plane field was replaced by an out-of-plane field, just below the coercive field and favoring a reversal.

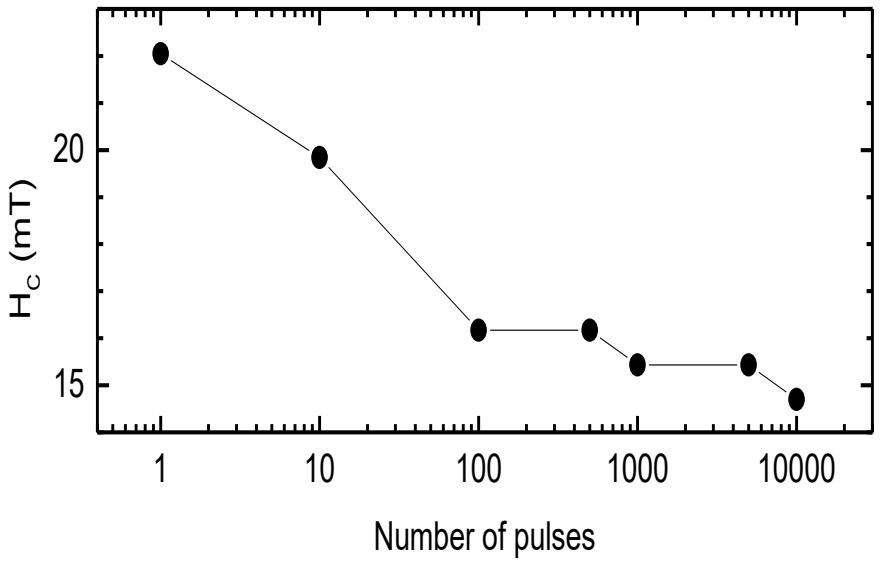

Figure 4.30 Switching probability as a function of temperature increment to test the HAMR scenario

In order to check for a heat-assisted magnetic recording-like scenario, single pulses were injected at the switching threshold current, under no in-plane field, and the variation of the coercive field (the applied out-of-plane field leading to ~50% reversal or more) was monitored as a function of the number of applied current pulses. If the sample was to be heated near T_c, then any out-of-plane magnetic field would lead to reversal even after excitation with a single current pulse. However, switching was observed when injecting a single pulse and applying an out-of-plane field as large as 93% of the switching field. In fact, only a small decrease of $\sim 30\%$ in the coercivity was observed when increasing the number of pulses by a factor of 10^5 as shown in figure 4.30. Hence it can be concluded that the dissipation by the electrical pulse does not heat the Co film near T_c. No reversal was observed after injection of a single current pulse at the critical current, which allows us to discard the HAMR scenario.

4.3.6.2 Domain wall nucleation mediated switching

A second possible scenario would be one considering multiple domain nucleations at specific sample sites, due to spatial inhomogeneities in material properties. Based on our estimated peak current density ($J_c \sim 6 \cdot 10^{12}$ A/m^2) if we extrapolate the expected domain wall velocity based on results of the fastest measured velocities in ferromagnets [116] we obtain ~1000 m/s. A Gaussian-like current pulse of 6 ps would allow for less than ~6nm of displacement, which is comparable to the domain wall width [15]. Therefore, under this scenario switching would be driven by nucleation. Nucleation would then need to cover at least 50% of the area, in order to determine the final state. At longer time scales, these domains could merge leading to a full switching [110]. We note that we did observe some domain formation observed in a different device, at currents close to the switching threshold, possibly correlated to the current distribution.

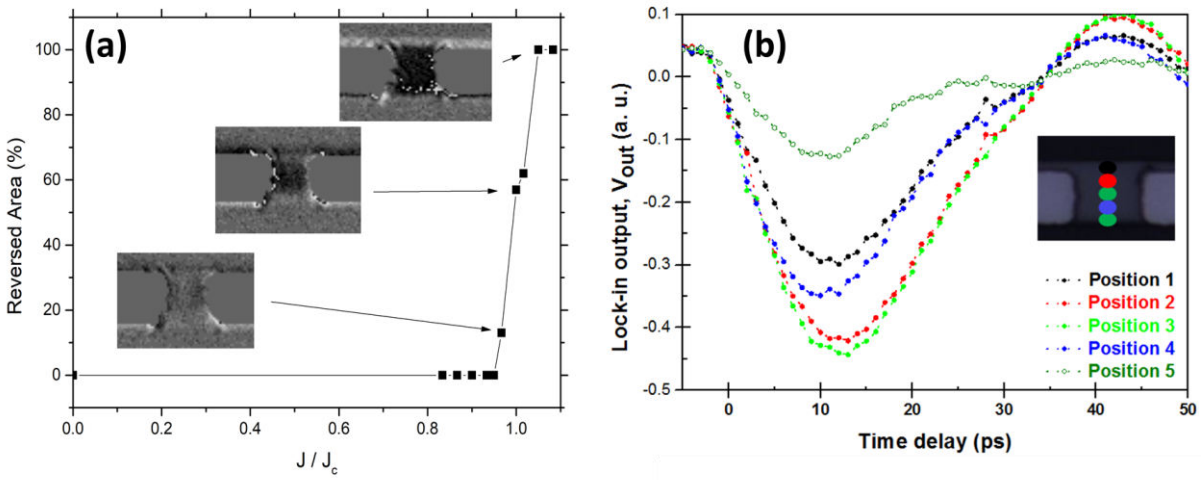

Figure 4.31 The switched area as a function of the current density normalized by the critical current density (Jc).

In order to check for a signature of non-coherent switching at ultrafast timescales, we performed low-intensity time-resolved dynamics at various positions on the magnet with our $\sim$1.5 µm diameter probe and found negligible differences (figure 4.31(b)). This measured homogeneity could mean nucleated domains are too small and numerous, or just that spatial inhomogeneities in the dynamics are below the sensitivity at such low intensities

The reversal process is first happening where the current density is the highest, at mid-height, right in between the tips of the rounded gold electrodes. In order to fully switch the device a little more current density than J_c is needed (figure 4.31(a)). These experiments were performed on the coplanar stripline design based devices. Moreover, the magnetic section had a $\sim 6\mu$m width, slightly wider than the co-planar waveguide sample ($\sim 4\mu$m). In fact, in the co-planar waveguide based device, these partial reversals were not clearly evidenced. This could be due to the narrower section, or also due to the gold contacts being flatter, possibly resulting in a more homogeneous current distribution.

4.3.7 Conclusion

In conclusion, spin-orbit torque-driven switching of a thin Co film with a single 6 ps electrical pulse is well reported in this chapter of the thesis. It has been shown that picosecond-duration electrical pulses can inject spin into a magnet at ultrafast timescales. We can then probe the generated magnetization torques with picosecond resolution. All our experiments are in agreement with the symmetries expected from SOT. Macrospin simulations can accurately predict the observed dynamics, showing a damping-like torque-dominated effect. Finally, we have shown that the reversal process is extremely energy efficient. Future work will include

tracking different components of the magnetization via different magneto-optical effects, in order to spatially reconstruct the time-dependent spin-torque dynamics. We believe our approach will trigger new interest in ultrafast electrical studies of spin-torque dynamics, opening the door for the possible observation of elusive phenomena such as inertial dynamics in ferromagnetic materials [117–119] and offer a new way of triggering resonant dynamics in antiferromagnetic materials [120,121].

4.4 Picosecond/THz Giant Magnetoresistance (GMR)

As detailed in section 2.2.2, Giant magnetoresistance can be studied in various kinds of magnetic nanostructures namely the magnetic multilayer GMR, spin valve GMR, Pseudo-spin-valve GMR, Granular GMR, etc [22]. We have tried to study GMR in both the magnetic multilayer and spin-valve GMR nanostructures. Conventionally, the reading operations are performed using the four-probe method explained in Section 3.2.2. The two resistance states correspond to the relative magnetic orientation between the ferromagnetic layers (parallel or antiparallel) and can be used to read the magnetic state of the bit.

Recently, Jin *et. al.,*[122] reported a slightly different approach to probe the magnetic state of the GMR stack. For this, they injected a THz pulse into the GMR stack and monitored the transmitted THz waveform. The peak amplitude of the THz pulse was found to be dependent on the external magnetic field that is applied across the GMR stack. The change in peak amplitude of the transmitted pulse had the same dependency on the external field as the magneto-resistance, demonstrating experimentally that magneto-resistance effects are still present up to THz. Furthermore, these experiments allowed the researchers to estimate various fundamental properties of magneto-transport such as scattering times and the spin scattering assymetry.

We expect that a very similar approach can be used for our on-chip THz devices. This would enable fully electrical pump-probe experiments with picosecond resolution. Furthermore, an electrical probe would allow to push the spatial resolution of our electrical pump-probe experiments to sub-wavelength dimensions where device physics could be tested (devices are typically 20-50nm in width). In the future, the THz GMR could be extended to exploit different magneto-resistances such as TMR or AMR. In the next subsection, a brief description of the samples and the detection approach is reported.

4.4.1 Sample of Choice and static GMR measurements

To study Giant magnetoresistance in picosecond time regime for read-out operations, we have tried to work with various samples. Table 4 represents the list of various samples taken under study. The first 10 samples listed in the table below are based on the spin-valve structure where an antiferromagnetic layer (IrMn in our case) is used to increase the coercivity of one of the ferromagnetic layers using antiferromagnetic-ferromagnetic exchange coupling (schematic shown in figure 4.32(a)). The other samples listed in the table are based on the multilayer structure in which a repeated bilayer system of a ferromagnet (Co in our case) and a non-magnetic metal (Cu in our case) is used (schematic shown in figure 4.32(b)).

Table 4 List of samples used to study giant magnetoresistance

S. No	Details of the magnetic stack (short name)	Current in-plane GMR %
1	Ta(5)/CoFeB(3)/Cu(3.5)Co(4)/IrMn(2.5)/ Pt(2)	2.85
2	Ta(5)/CoFeB(3)/Cu(3.5)Co(4)/IrMn(2)/ Pt(2)	2.80
3	Ta(5)/CoFeB(3)/Cu(3.5)Co(4)/IrMn(1.5)/ Pt(2)	1.14
4	Ta(5)/CoFeB(4)/Cu(3.5)Co(5)/IrMn(2.5)/ Pt(2)	2.68
5	Ta(5)/CoFeB(4)/Cu(3.5)Co(5)/IrMn(2)/ Pt(2)	2.48
6	Ta(5)/CoFeB(3)/Cu(3.5)Co(3)/IrMn(3)/ Pt(2)	2.65
7	Ta(5)/CoFeB(4)/Cu(3.5)Co(3)/IrMn(3)/ Pt(2)	2.68
8	Ta(5)/CoFeB(3)/Cu(3.5)Co(4)/IrMn(3)/ Pt(2)	3.03
9	Ta(5)/CoFeB(4)/Cu(3.5)Co(4)/IrMn(3)/ Pt(2)	2.75
10	Ta(5)/CoFeB(4)/Cu(3.5)Co(4)/IrMn(4)/ Pt(2)	2.54
11	Ta(3)/Cu(2.5)/[Co(2)/Cu(0.84)/Co(1.4)/Cu(0.84)]×10/Pt(2)	4.54
12	Ta(3)/Cu(2.5)/[Co(2)/Cu(0.98)/Co(1.4)/Cu(0.98)]×10/Pt(2)	6.05
13	Ta(3)/Cu(2.5)/[Co(2)/Cu(1.12)/Co(1.4)/Cu(1.12)]×10/Pt(2)	1.83
14	Ta(3)/Cu(2.5)/[Co(2)/Cu(1.24)/Co(1.4)/Cu(1.24)]×10/Pt(2)	2.10

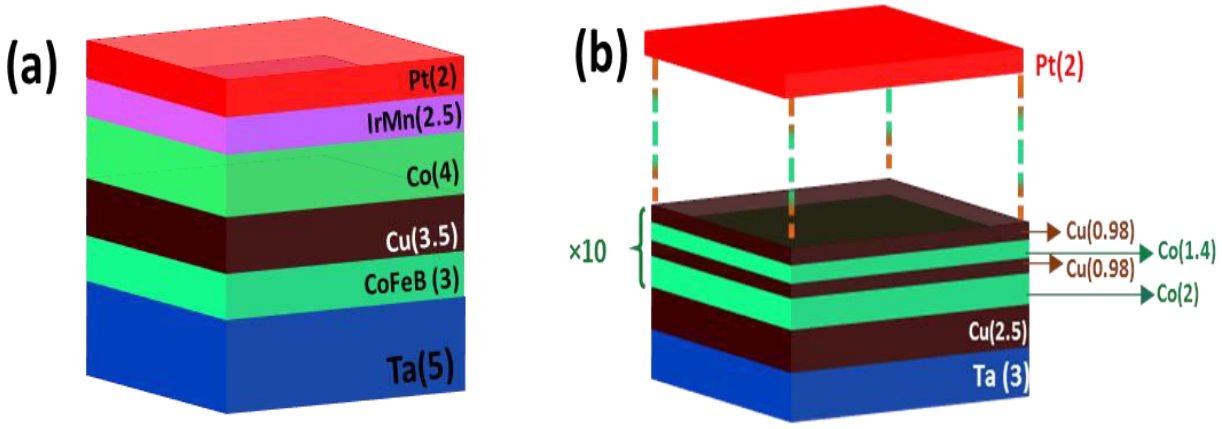

Figure 4.32 Schematics of (a) spin-valve and (b) magnetic multilayer structure based stacks deposited on the on-chip THz device to detect GMR using THz pulse

Figure 4.33(a) shows the in-plane magnetic hysteresis loops for some of the spin-valve-based samples. These measurements were performed to select the sample of choice based on their static magnetic response (coercivity, remanence etc). The hysteresis loops shown in figure 4.33(a) show the full hysteresis corresponding to both the exchange hardened layer by IrMn (high coercivity) and the free (low coercivity) ferromagnetic layers. For instance, the sample

corresponding to the blue curve (figure 4.33(a)) has a high coercivity of more than 100mT which is difficult to achieve with the current set of electromagnets on the pump-probe setup, and hence a sample with comparatively low coercivity will be far more preferable (black curve in figure 4.33(a)). The samples based on multilayer structures were found to have a very high coercivity of ~500mT which is not possible to achieve during the THz-GMR detection measurements on our setup.

Figure 4.33(b) shows the static GMR measurements taken using the four-probe setup shown in figure 3.5. Three distinct samples are shown in figure 4.33(b) to show the importance of different parameters that are essential for the sample of choice during the THz-GMR measurements. For example, the sample corresponding to the black curve will be of least interest due to very low GMR % and also the sample corresponding to the red curve due to very low remanence state. The sample corresponding to the blue curve will be of great interest since the GMR% is high and the coercivity is low which is easily achievable on our setup along with the stable remanence state.

Out of many samples, CoFeB(3)/Cu(3.5)Co(4)/IrMn(2.5) spin-valve-based nanostructure was chosen to be deposited on the on-chip THz device. The experimental procedure and challenges to perform the THz-GMR measurements are reported in the next section.

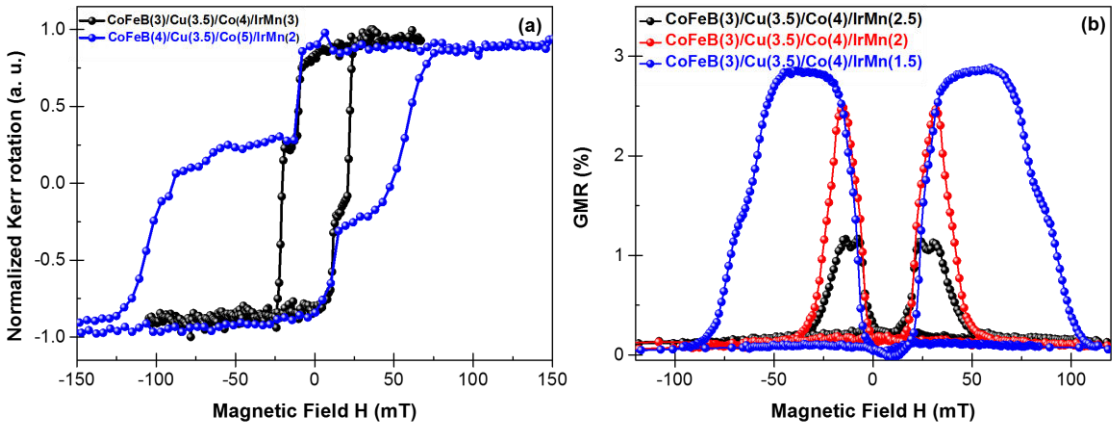

Figure 4.33 (a) In-plane MOKE hysteresis loops, and (a) static GMR measurements on different spin-valve based nanostructures

4.4.2 THz-GMR detection

In our experiments, we will try to measure the transmitted THz pulse on the transmission line with the Teraspike® probe. Figure 4.34(a) shows the experimental view of the setup. The idea behind this approach is to probe the GMR-induced change in the peak amplitude of the THz

signal in both the reflected as well as the transmitted pulse. With the incident, reflected, and transmitted pulses we will be able to extract the difference in absorption for both magnetic states. Interestingly, if the absorption is significantly different, the dynamics after an intense pulse could also be very different for both initial magnetic states. Figure 4.34 (b) shows the measurement of the THz electric field before (incident pulse + delayed reflection) and after the magnetic load/ GMR stack. This measurement is helpful to extract the transmission and reflected percentages. Unfortunately, the Teraspike® used to detect the electric field component of THz pulses is not well calibrated. Also, as discussed in section 3.3.2, the amplitude of the detected field is very sensitive to the positioning of the Teraspike as well as its optical excitation, which renders experiments taken at different days or different positions difficult to compare. Therefore, the transmitted (or reflected) wave will need to be measured without moving the Teraspike® as the magnetic configuration is changed from parallel to antiparallel. Using the Teraspike® probe makes this experiment complicated since we cannot use the electromagnet at the same time due to geometrical constraints. Also, any magnetic field is susceptible to moving the Teraspike® probe, affecting its sensitivity or even worse, damaging it (the tips are extremely fragile). In the near future we plan on integrating detection probes on the chip itself (using LT-GaAs photoswitches), to make measurements more reliable, sensitive, and less bulky (no external tip and positioner needed). On the downside, the bandwidth might be slightly reduced in comparison to the 4THz of the Teraspike®.

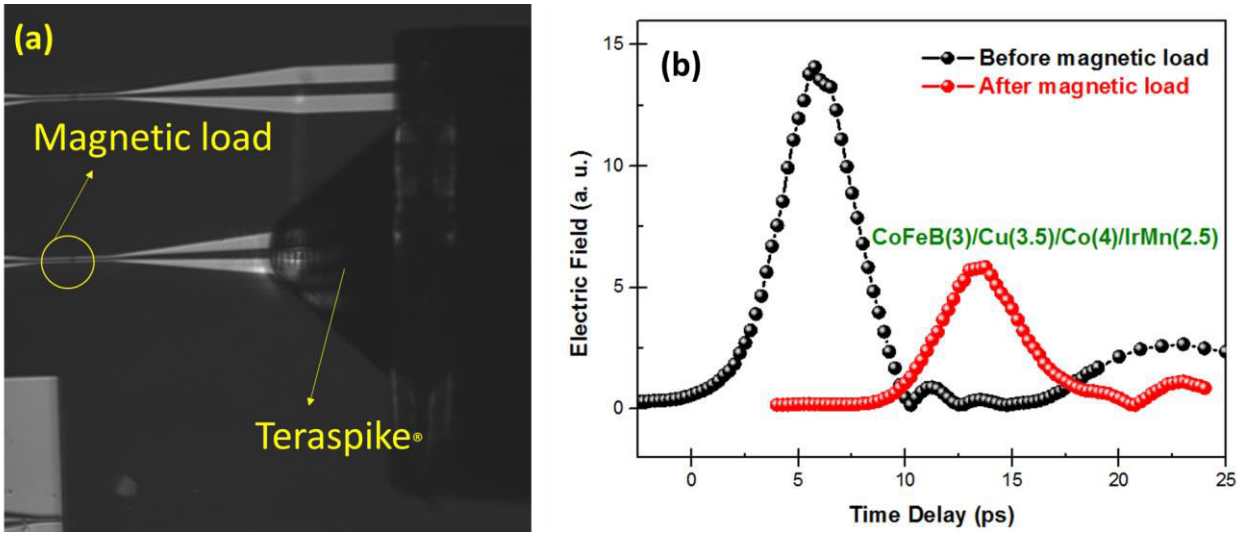

Figure 4.34 (a) Experimental setup used to detect the giant magnetic resistance using THz pulses, and (b) THz electric field measurement is taken before and after the magnetic load

So far, working with a small permanent magnet to change the magnetic state and with the Teraspike® detector has yielded no noticeable differences in the transmission. However, during such attempts, we had no way of verifying that the permanent magnet had indeed changed the

state of the magnetic multilayer. In future experiments, the magnetic state will be monitored via longitudinal MOKE or DC magnetoresistance measurements. In parallel, new structures and new transmission line designs (with embedded photoswitches) will be attempted.

4.4.3 Conclusion

A unique approach to detect the giant magnetoresistance effect using on-chip THz devices has been introduced in this chapter. Although still a work in progress, such detection capabilities would enable a whole new range of experiments on nano-magnetic devices, where at the moment ultrafast probing is a big challenge. In other words, ultrafast magneto-resistive measurements are in a way the equivalent of ultrafast magneto-optical measurements, and if demonstrated on-chip, they would open up all-electrical on-chip pump-probe experiments.

5

Conclusions & Perspectives

This chapter comprises the final conclusions of all chapters of this thesis. The scope of further studies based on this thesis is also briefly discussed in the end.

****

5.1 Final Conclusions

- ✓ In this manuscript, a unique pump-probe setup that allows the study of spin torques at the picosecond timescale has been presented. The setup combines ultrafast Auston switches and a magneto-optical pump-probe configuration to access the dynamics of a magnetic material after a picosecond current excitation, all within a 2D magnetic field. These type of experiments uncover the dynamics at timescales shorter than the ferromagnetic resonance, unveiling a previously inaccessible view of spin-torques.

- ✓ Both out-of-plane and in-plane magnetized Co ferromagnetic systems have been excited with picosecond-duration spin-orbit torques, and the resulting dynamics have been analyzed. So far, most results can be reasonably well explained by a macrospin model.

- ✓ In this thesis, we have demonstrated the fastest reversal of a ferromagnet via the use of spin-orbit torques. A single 6 picosecond wide electrical pulse was enough to reverse the magnetization. The symmetries and the subsequent ultrafast dynamics are analyzed and agree with a spin-orbit torque mediated switching. We suggest that ultrafast Joule heating and its effect on the anisotropy play an important role. The energy estimates and its projection for nano-sized devices are encouraging, but the reversal mechanism is still unknown and further experiments are required.

- ✓ In order to develop electrical ultrafast methods to access the magnetic state of these on-chip devices, we are currently pursuing experiments to detect a change in the THz transmittivity as a function of the DC magneto-resistance. Such a THz magneto-resistive probe could enable faster readouts of a magnetic memory.

5.2 Perspectives

- ➢ A further study could be done to better optimize the on-chip THz device by optimizing different parameters of transmission line parameters.

- ➢ A slightly new approach in the lithography step could also be implemented which will eliminate one step of the lithography. The photoconductive switches can be fabricated

on a separate LT-GaAs substrate which can be reused for different devices with different transmission line structures and magnetic specimens. The photoconductive switch can then be connected with the rest of the device using impedance-matched resistors. This approach will reduce the cost of the overall device since the transmission line and magnetic specimen can be deposited on any other low-cost substrate instead of LT-GaAs.

- In order to better elucidate the SOT's amplitude and the subsequent magnetization dynamics, a number of directions will have to be followed: A better calibration of the THz current amplitude is required. A larger range of current values should be studied in order to better separate heating effects from SOTs. Samples with predominantly field-like torques vs damping-like torques should be compared, and spin-torque FMR should also be performed to compare the amplitudes of the torques at different frequencies. Finally, the switching dynamics, if accessed, would enable to better understand the reversal mechanisms and the role of the SOTs in the reversal.

- A further study could also be done to detect the giant magnetoresistance effect using THz pulses. In fact, a study to detect tunnel magnetoresistance (TMR) can also be of great interest.

6

References

1. Zhang, C., Fukami, S., Sato, H., Matsukura, F. & Ohno, H. Spin-orbit torque induced magnetization switching in nano-scale Ta / CoFeB / MgO. *Appl. Phys. Lett.* **012401**, 1–5 (2015).

2. Sinova, J., Valenzuela, S. O., Wunderlich, J., Back, C. H. & Jungwirth, T. Spin Hall effects. *Rev. Mod. Phys.* **87**, 1213–1260 (2015).

3. Garello, K. *et al.* Ultrafast magnetization switching by spin- orbit torques. *Appl. Phys. Lett.* **105**, 1–5 (2014).

4. Beaurepaire, E., Merle, J.-C., Daunois, A. & Bigot, J.-Y. Ultrafast spin dynamics in ferromagnetic nickel. *Phys. Rev. Lett.* **76**, 4250–4253 (1996).

5. Baibich, M. N. *et al.* Giant magnetoresistance of (001)Fe/(001)Cr magnetic superlattices. *Phys. Rev. Lett.* **61**, 2472–2475 (1988).

6. Mgo, T. C. *et al.* Layer thickness dependence of the current-induced effective field vector in Ta | CoFeB | MgO. *Nat. Mater.* **12**, 240–245 (2013).

7. Ou, Y., Pai, C., Shi, S., Ralph, D. C. & Buhrman, R. A. Origin of fieldlike spin-orbit torques in heavy metal / ferromagnet / oxide thin film heterostructures. *Phys. Rev. B* **94**, 1–6 (2016).

8. Mistry, K. *et al.* A 45nm Logic Technology with High-k+Metal Gate Transistors, Strained Silicon, 9 Cu Interconnect Layers, 193nm Dry Patterning, and 100% Pb-free Packaging. *IEEE Int. Electron Devices Meet.* 247–250 (2007).

9. Garello, K. *et al.* SOT-MRAM 300mm integration for low power and ultrafast embedded memories. *IEEE Symp. VLSI Circuits* **54**, 81–82 (2018).

10. Beaurepaire, E., Merle, J., Daunois, A. & Bigot, J. Ultrafast Spin Dynamics in

Ferromagnetic Nickel. *Phys. Rev. Lett.* **76**, 4250–4253 (1996).

11. Koopmans, B., Ruigrok, J. J. M., Longa, F. D. & Jonge, W. J. M. De. Unifying Ultrafast Magnetization Dynamics. *Phys. Rev. Lett.* **95**, 1–4 (2005).

12. Battiato, M., Carva, K. & Oppeneer, P. M. Superdiffusive Spin Transport as a Mechanism of Ultrafast Demagnetization. *Phys. Rev. B - Condens. Matter Mater. Phys.* **105**, 1–4 (2010).

13. Ostler, T. A. *et al.* Transient ferromagnetic-like state mediating ultrafast reversal of antiferromagnetically coupled spins ¨. *Nat. Lett.* **472**, 5–9 (2011).

14. Bluendell, S. *Magnetism in Condensed Matter*. (Oxford University Press InC, 2001).

15. Thiaville, A., Rohart, S., Jué, É., Cros, V. & Fert, A. Dynamics of Dzyaloshinskii domain walls in ultrathin magnetic films. *Epl* **100**, 1–6 (2012).

16. Johnson, M. T., Bloemen, P., Broeder, Fja. & Vries, J. J. de. Magnetic anisotropy in metallic multilayers. *Reports Prog. Phys.* **59**, 1409–1458 (1996).

17. Hait, S. *et al.* Comparison of high temperature growth versus post-deposition in situ annealing in attaining very low Gilbert damping in sputtered Co 2 FeAl Heusler alloy films. *J. Magn. Magn. Mater.* **519**, 1–14 (2021).

18. Ralph, D. C. & Stiles, M. D. Spin transfer torques. **320**, 1190–1216 (2008).

19. Schrieffer, R. & Campbell, A. TWO-CURRENT CONDUCTION IN NICKEL. **21**, 15–17 (1968).

20. Guillemard, C. *et al.* Engineering Co2MnAlxSi1-x Heusler Compounds as a Model System to Correlate Spin Polarization, Intrinsic Gilbert Damping, and Ultrafast Demagnetization. *Adv. Mater.* **32**, 1–8 (2020).

21. Mcguire, T. R. & Potter, R. I. Anisotropic Magnetoresistance in Ferromagnetic 3D Alloys. *IEEE Trans. Magn.* **11**, 1018–1038 (1975).

22. Tsymbal, E. Y. & Pettifor, D. G. Perspectives of giant magnetoresistance. *Solid State Phys. - Adv. Res. Appl.* **56**, 113–237 (2001).

23. Marchon, B., Pitchford, T., Hsia, Y. & Gangopadhyay, S. The Head-Disk Interface Roadmap to an Areal Density of 4 Tbit / in 2. *Adv. Tribol.* **2013**, 1–8 (2013).

24. Slonczewski, J. C. Current-driven excitation of magnetic multilayers. *J. Magn. Magn. Mater.* **159**, L1–L7 (1996).

25. Berger, L. Emission of spin waves by a magnetic multilayer traversed by a current. **54**, 9353–9358 (1996).

26. Abert, C. *et al.* Fieldlike and Dampinglike Spin-Transfer Torque in Magnetic Multilayers. *Phys. Rev. Appl.* **054007**, 1–7 (2017).

27. Zhao, W. S. *et al.* Microelectronics Reliability Failure and reliability analysis of STT-MRAM. *Microelectron. Reliab.* **52**, 1848–1852 (2012).

28. Ramaswamy, R., Lee, J. M., Cai, K. & Yang, H. Recent advances in spin-orbit torques : Moving towards device applications. *Appl. Phys. Rev.* **5**, 1–19 (2018).

29. Miron, I. M. *et al.* Current-driven spin torque induced by the Rashba effect in a ferromagnetic metal layer. *Nat. Mater.* **9**, 230–234 (2010).

30. Rodmacq, B., Schuhl, A. & Gambardella, P. Perpendicular switching of a single ferromagnetic layer induced by in-plane current injection ´. *Nat. Lett.* **476**, 189–193 (2011).

31. Liu, L., Lee, O. J., Gudmundsen, T. J., Ralph, D. C. & Buhrman, R. A. Current-Induced Switching of Perpendicularly Magnetized Magnetic Layers Using Spin Torque from the Spin Hall Effect. *Phys. Rev. Lett.* **109**, 1–5 (2012).

32. Gambardella, P. & Miron, I. M. Current-induced spin–orbit torques. *Philos. Trans. R. Soc. A* **369**, 3175–3197 (2011).

33. Woo, S., Mann, M., Tan, J. A., Caretta, L. & Beach, S. D. G. Enhanced spin-orbit torques in Pt / Co / Ta heterostructures. *Appl. Phys. Lett.* **105**, 1–6 (2014).

34. You, A., Be, M. A. Y. & In, I. Conversion of spin current into charge current at room temperature : Inverse spin- Hall effect Inverse spin-Hall effect. *Appl. Phys. Lett.* **182509**, 15–18 (2016).

35. Ghosh, S. & Manchon, A. Spin-orbit torque in a three-dimensional topological insulator – ferromagnet heterostructure : Crossover between bulk and surface transport. *Phys. Rev. B* **97**, 1–10 (2018).

36. Garello, K. *et al.* Symmetry and magnitude of spin–orbit torques in ferromagnetic heterostructures. *Nat. Nanotechnol.* **8**, 587–593 (2013).

37. Morota, M. *et al.* Indication of intrinsic spin Hall effect in 4 d and 5 d transition metals. *Phys. Rev. B* **174405**, 1–5 (2011).

38. Hoffmann, A. Spin Hall Effects in Metals, IEEE Transactions on Magnetics. *IEEE Trans. Magn.* **49**, 5172–5193 (2013).

39. Garlow, J. A. *et al.* Quantification of Mixed Bloch-N ´ eel Topological Spin Textures Stabilized by the Dzyaloshinskii-Moriya Interaction in Co = Pd Multilayers. *Phys. Rev. Lett.* **122**, 237201–5 (2019).

40. Montazeri, M. *et al.* Magneto-optical investigation of spin-orbit torques in metallic and insulating magnetic heterostructures. *Nat. Commun.* **6**, 1–9 (2015).

41. Liu, L., Moriyama, T., Ralph, D. C. & Buhrman, R. A. Spin-Torque Ferromagnetic Resonance Induced by the Spin Hall Effect. *Phys. Rev. Lett.* **036601**, 1–4 (2011).

42. Yan, S. & Bazaliy, Y. B. Phase diagram and optimal switching induced by spin Hall effect in a perpendicular. *Phys. Rev. B* **214424**, 1–12 (2015).

43. Lee, O. J. *et al.* Central role of domain wall depinning for perpendicular magnetization

switching driven by spin torque from the spin Hall effect. *Phys. Rev. B* **024418**, 1–8 (2014).

44. Soong, H. K. & Malta, J. B. Femtosecond Lasers in Ophthalmology. *Am. J. Ophthalmol.* **147**, 189–197 (2009).

45. You, A., Be, M. A. Y. & In, I. Coherent terahertz emission from ferromagnetic films excited by femtosecond laser pulses. *Appl. Phys. Lett.* **3465**, 1–4 (2017).

46. Kirilyuk, A., Kimel, A. V & Rasing, T. Ultrafast optical manipulation of magnetic order. *Rev. Mod. Phys.* **82**, 2731–2784 (2010).

47. Malinowski, G., Bergeard, N., Hehn, M. & Mangin. Hot-electron transport and ultrafast magnetization dynamics in magnetic multilayers and nanostructures following femtosecond laser pulse excitation. *Eur. Phys. J. B* **91:98**, 1–20 (2018).

48. Aeschlimann, M. Explaining the paradoxical diversity of ultrafast laser-induced demagnetization. *Nat. Mater.* **9**, 259–265 (2010).

49. Brorson, S. D., Fujimoto, J. G. & Ippen, E. P. Femtosecond Electronic Heat-Transport Dynamics in Thin Gold Films. *Phys. Rev. Lett.* **59**, 1962–1965 (1987).

50. Malinowski, G. *et al.* Control of speed and efficiency of ultrafast demagnetization by direct transfer of spin angular momentum. *Nat. Lett.* **4**, 855–858 (2008).

51. Stanciu, C. D. *et al.* All-Optical Magnetic Recording with Circularly Polarized Light. *Phys. Rev. Lett.* **99**, 1–4 (2007).

52. Radu, I. *et al.* Transient ferromagnetic-like state mediating ultrafast reversal of antiferromagnetically coupled spins. *Nat. Lett.* **472**, 205–208 (2011).

53. Mangin, S. *et al.* Current-induced magnetization reversal in nanopillars with perpendicular anisotropy. *Nat. Mater.* **5**, 2–7 (2006).

54. Olivier, A., Li, G. & Davies, C. S. Single-shot all-optical switching of magnetization in Tb / Co multilayer- based electrodes. **10:5211**, 1–8 (2020).

55. Kirilyuk, A., Kimel, A. V & Rasing, T. Laser-induced magnetization dynamics and reversal in ferrimagnetic alloys. *Reports Prog. Phys.* **026501**, 1–36 (2013).

56. Coey, J. M. D., Besbas, J. & Rode, K. Single pulse all-optical toggle switching of magnetization without gadolinium in the ferrimagnet Mn2RuxGa. *Nat. Commun.* **11:4444**, 1–6 (2020).

57. Wilson, R. B. *et al.* Electric current induced ultrafast demagnetization. *Phys. Rev. B* **96**, 1–9 (2017).

58. Tonouchi, M. Cutting-edge terahertz technology. *Nat. Photonics* **1**, 97–105 (2007).

59. Kampfrath, T. *et al.* Coherent terahertz control of antiferromagnetic spin waves. *Nat. Photonics* **5**, 31–34 (2011).

60. Seifert, T. *et al.* Efficient metallic spintronic emitters of ultrabroadband terahertz

radiation. *Nat. Photonics* **10**, 483–487 (2016).

61. Burford, N. M., Burford, N. M. & El-shenawee, M. O. Review of terahertz photoconductive antenna technology. *Opt. Eng.* **56**, (2021).

62. Yang, Y. *et al.* Ultrafast magnetization reversal by picosecond electrical pulses. *Sci. Adv.* **3**, 1–6 (2017).

63. Choi, G., Min, B., Lee, K. & Cahill, D. G. Spin current generated by thermally driven ultrafast demagnetization. *Nat. Commun.* **5:4334**, 1–8 (2014).

64. Mann, A. *et al.* Insights into Ultrafast Demagnetization in Pseudogap Half-Metals. *Phys. Rev. X* **2**, 1–9 (2012).

65. Auston, D. H. Picosecond optoelectronic switching and gating in silicon. *Appl. Phys. Lett.* **26**, 1–4 (1975).

66. Robinson, C. C. The Faraday Rotation of Diamagnetic Glasses from 0.334 A to 1.9 A. *Appl. Opt.* **3**, 1163–1166 (1964).

67. Oppeneer, P. M. *Theory of the Magneto-Optical Kerr Effect in Ferromagnetic Compounds*. (1999). doi:10.13140/2.1.3171.4083

68. Funk, T., Deb, A., George, S. J., Wang, H. & Cramer, S. P. X-ray magnetic circular dichroism — a high energy probe of magnetic properties. *Coord. Chem. Rev.* **249**, 3–30 (2005).

69. LISSBERGER, P. H. & PARKER, M. R. Voigt Effect in Magnetic Films. *J. Appl. Phys.* **42**, 1708–1709 (1971).

70. Chen, J., Ding, W. X. & Brower, D. L. Impact of the Cotton – Mouton effect on Faraday polarimetry measurements using circular polarization. *Plasma Phys. Control. Fusion* **60**, 1–9 (2018).

71. Schellekens, A. J. Manipulating spins : novel methods for controlling magnetization dynamics on the ultimate timescale. (Eindhoven: Technische Universiteit Eindhoven, 2014). doi:10.6100/IR770953

72. Gomez, M. J., Liu, K., Lee, J. G. & Wilson, R. B. High sensitivity pump – probe measurements of magnetic , thermal , and acoustic phenomena with a spectrally tunable oscillator High sensitivity pump – probe measurements of magnetic , thermal , and acoustic phenomena with a spectrally tunable oscillator. *Rev. Sci. Instrum.* **91**, 1–11 (2020).

73. Dietrich, W., Proebster, W. E. & Wolf, P. Nanosecond Switching in Thin Magnetic Films. in *Conference on Magnetism and Magnetic Materials* 189–196 (1960).

74. You, A., Be, M. A. Y. & In, I. Free-space detection of terahertz radiation using crystalline and polycrystalline ZnSe electro-optic sensors. *Appl. Phys. Lett.* **2294**, 10–13 (2002).

75. Smith, R., Jooshesh, A., Zhang, J. & Darcie, T. Photoconductive generation and detection of THz-bandwidth pulses using near-field coupling to a free-space metallic slit waveguide.

Opt. Express **25**, 26492–26499 (2017).

76. Mittkeman, D. M., Jacobsen, R. H., Neelamani, R., Baraniuk, R. & Nuss, M. C. Gas sensing using terahertz time-domain spectroscopy. *Appl. Phys. B* **67**, 379–390 (1998).

77. Gupta, K. C., Garg, R., Bahl, I. & Bhartia, P. *Microstrip Lines and Slotlines*. (Artech House, 1996).

78. Pozar, D. M. *Microwave Engineering*. (John Wiley & Sons, 2011).

79. Y. S. Touloukian. Recommended Values of the Thermophysical Properties of Eight Alloys, Major Constituents and their Oxides Thermophysical Properties Research Center, Purdue University, Lafayette, Indiana,. (1966).

80. Verstraete, M. J. Ab initio calculation of spin-dependent electron – phonon coupling in iron and cobalt. *J. physicscondensed matter* **25**, 1–8 (2013).

81. Allen, P. B. Empirical electron-phonon A. values from resistivity of cubic metallic elements. *Phys. Rev. B* **36**, 2920–2923 (1987).

82. Lee, K., Choi, J. W., Sok, J. & Min, B. Temperature dependence of the interfacial magnetic anisotropy in W / CoFeB / MgO. *AIP Adv.* **7**, 1–8 (2017).

83. Shao, Q. *et al.* Roadmap of Spin – Orbit Torques. *IEEE Trans. Magn.* **57**, 1–39 (2021).

84. Kawahara, T., Ito, K., Takemura, R. & Ohno, H. Microelectronics Reliability Spin-transfer torque RAM technology : Review and prospect. *Microelectron. Reliab.* **52**, 613–627 (2012).

85. Woo, S. *et al.* Observation of room-temperature magnetic skyrmions and their current-driven dynamics in ultrathin metallic ferromagnets. *Nat. Mater.* **15**, 501–507 (2016).

86. Miron, I. M. *et al.* Perpendicular switching of a single ferromagnetic layer induced by in-plane current injection. *Nature* **476**, 189–193 (2011).

87. Cubukcu, M. *et al.* Spin-orbit torque magnetization switching of a three-terminal perpendicular magnetic tunnel junction. *Appl. Phys. Lett.* **104**, 1–6 (2014).

88. Lo Conte, R. *et al.* Spin-orbit torque-driven magnetization switching and thermal effects studied in Ta\CoFeB\MgO nanowires. *Appl. Phys. Lett.* **105**, 1–6 (2014).

89. Baumgartner, M. *et al.* Spatially and time-resolved magnetization dynamics driven by spin-orbit torques. *Nat. Nanotechnol.* **12**, 980–986 (2017).

90. Conte, L. *et al.* Spin-orbit torque-driven magnetization switching and thermal effects studied in Ta \CoFeB\MgO nanowires. *Appl. Phys. Lett.* **105**, 1–4 (2014).

91. Choi, G., Wilson, R. B. & Cahill, D. G. Indirect heating of Pt by short-pulse laser irradiation of Au in a nanoscale Pt / Au bilayer. *Phys. Rev. B* **064307**, 1–7 (2014).

92. Keil, U. D. & Dykaar, D. R. Ultrafast Pulse Generation in Photoconductive Switches. *IEEE J. Quantum Electron.* **32**, 1664–1671 (1996).

93. Lattery, D. M. *et al.* Quantitative analysis and optimization of magnetization precession initiated by ultrafast optical pulses. *Appl. Phys. Lett.* **113**, 1–5 (2018).

94. Davies, C. S. *et al.* Anomalously Damped Heat-Assisted Route for Precessional Magnetization Reversal in an Iron Garnet. *Phys. Rev. Lett.* **122**, 1–4 (2019).

95. Hopkins, P. E. Thermal Transport across Solid Interfaces with Nanoscale Imperfections : Effects of Roughness , Disorder , Dislocations , and Bonding on Thermal Boundary Conductance. *ISRN Mech. Eng.* **682586**, (2013).

96. Wilson, R. B., Apgar, B. A., Hsieh, W., Martin, L. W. & Cahill, D. G. Thermal conductance of strongly bonded metal-oxide interfaces. *Phys. Rev. B* **91**, 1–7 (2015).

97. Monachon, C., Weber, L. & Dames, C. Thermal Boundary Conductance : A Materials Science Perspective. *Annu. Rev. Mater. Res.* **46**, 8.1-8.31 (2016).

98. Sato, H. *et al.* 14ns write speed 128Mb density Embedded STT-MRAM with endurance > 10 10 and 10yrs retention @ 85 ° C using novel low damage MTJ integration process. in *2018 IEEE International Electron Devices Meeting (IEDM)* 27.2.1-27.2.4 (IEEE, 2018).

99. Hoffmann, M. C. & Fülöp, J. A. Intense ultrashort terahertz pulses: Generation and applications. *J. Phys. D. Appl. Phys.* **44**, 083001 (2011).

100. Bonvalet, A. & Joffre, M. Terahertz Femtosecond Pulses. in *Femtosecond Laser Pulses* (ed. Rullière, C.) 309–333 (Springer, 2005).

101. Gregory, I. S. *et al.* Optimization of photomixers and antennas for continuous-wave terahertz emission. *IEEE J. Quantum Electron.* **41**, 717–728 (2005).

102. Burford, N. M. & El-Shenawee, M. O. Review of terahertz photoconductive antenna technology. *Opt. Eng.* **56**, 010901 (2017).

103. Auston, D. H., Johnson, A. M., Smith, P. R. & Bean, J. C. Picosecond optoelectronic detection, sampling, and correlation measurements in amorphous semiconductors. *Appl. Phys. Lett.* **37**, 371 (2008).

104. Liu, L. *et al.* Spin-Torque Switching with the Giant Spin Hall Effect of Tantalum. *Science.* **336**, 555–558 (2012).

105. Garello, K. *et al.* Ultrafast magnetization switching by spin-orbit torques. *Appl. Phys. Lett.* **105**, 1–12 (2014).

106. Brown, W. F. Thermal Fluctuations of a Single-Domain Particle. *Phys. Rev.* **130**, 1677–1686 (1963).

107. El Hadri, M. S. *et al.* Two types of all-optical magnetization switching mechanisms using femtosecond laser pulses. *Phys. Rev. B* **94**, 1–8 (2016).

108. Guan, Y. *et al.* Thermal-magnetic noise measurement of spin-torque effects on ferromagnetic resonance in MgO-based magnetic tunnel junctions. *Appl. Phys. Lett.* **95**, 1–3 (2009).

109. Cubukcu, M. *et al.* Ultra-Fast Perpendicular Spin–Orbit Torque MRAM. *IEEE Trans. Magn.* **54**, 1–4 (2018).

110. Decker, M. M. *et al.* Time Resolved Measurements of the Switching Trajectory of Pt/Co Elements Induced by Spin-Orbit Torques. *Phys. Rev. Lett.* **118**, 1–5 (2017).

111. Grimaldi, E. *et al.* Single-shot dynamics of spin–orbit torque and spin transfer torque switching in three-terminal magnetic tunnel junctions. *Nat. Nanotechnol.* **15**, 111–117 (2020).

112. Graves, C. E. *et al.* Nanoscale spin reversal by non-local angular momentum transfer following ultrafast laser excitation in ferrimagnetic GdFeCo. *Nat. Mater.* **12**, 293–298 (2013).

113. Iacocca, E. *et al.* Spin-current-mediated rapid magnon localisation and coalescence after ultrafast optical pumping of ferrimagnetic alloys. *Nat. Commun.* **10**, 1–11 (2019).

114. Atxitia, U., Nieves, P. & Chubykalo-Fesenko, O. Landau-Lifshitz-Bloch equation for ferrimagnetic materials. *Phys. Rev. B* **86**, 1–11 (2012).

115. Cai, K. *et al.* Ultrafast and energy-efficient spin–orbit torque switching in compensated ferrimagnets. *Nat. Electron.* **3**, 37–42 (2020).

116. Miron, I. M. *et al.* Fast current-induced domain-wall motion controlled by the Rashba effect. *Nat. Mater.* **10**, 419–23 (2011).

117. Kikuchi, T. & Tatara, G. Spin dynamics with inertia in metallic ferromagnets. *Phys. Rev. B* **92**, 1–15 (2015).

118. Wegrowe, J.-E. & Ciornei, M.-C. Magnetization dynamics, gyromagnetic relation, and inertial effects. *Am. J. Phys.* **80**, 607–611 (2012).

119. Neeraj, K. *et al.* Experimental evidence of inertial dynamics in ferromagnets. *arXiv:1910.11284* 1–10 (2019).

120. Němec, P., Fiebig, M., Kampfrath, T. & Kimel, A. V. Antiferromagnetic opto-spintronics. *Nat. Phys.* **14**, 229–241 (2018).

121. Baltz, V. *et al.* Antiferromagnetic spintronics. *Rev. Mod. Phys.* **90**, 1–57 (2018).

122. Jin, Z. *et al.* Accessing the fundamentals of magnetotransport in metals with terahertz probes. *Nat. Phys.* **11**, 761–766 (2015).